

Centre Énergie Matériaux Télécommunications

**Development of Ytterbium-Laser-Based Intense Terahertz Sources and
an Application in Field-Driven Electron Photoemission from Out-of-
Plane Resonant Nanostructures**

Par

Andrea Rovere

Thèse présentée pour l'obtention du grade de
Philosophiae Doctor (Ph.D.)
en sciences des l'énergie et des matériaux

Jury d'évaluation

Président du jury et
examinateur interne

Tsuneyuki Ozaki
INRS – EMT

Examinateur externe

Ksenia Dolgaleva
University of Ottawa

Examinateur externe

Matthew Reid
University of Northern British Columbia

Directeur de recherche

Luca Razzari
INRS – EMT

Codirecteur de recherche

Roberto Morandotti
INRS – EMT

ACKNOWLEDGEMENTS

I would like to thank all the people that have accompanied me through this PhD.

My supervisor Prof. Luca Razzari, who has supported and encouraged me to pursue my goals. For finding always the time to discuss about my research, sharing his passion and knowledge to solve the problems together.

My co-supervisor Prof. Roberto Morandotti, who has invested his trust on my capabilities and has always contributed with his experience to add more value to my work.

Dr. Riccardo Piccoli and Dr. Young-Gyun Jeong from whom I have learnt something new day by day and for their help in many situations (experiments, data analysis, writing, etc.) I am really glad for having had you not only as mentors, but also as good friends.

All the colleagues and friends from our group and from the Institute that I have met along this experience. The list would be too long. Thanks for the mutual aids, the coffees and the time spent together inside and outside of INRS. You made this experience much more enjoyable!

My roommates Eva, Daniel and Spot. Thank you for sharing chats, every day or long-term plans, meals and cuddles. Living with you is great!

All the amazing people I have met in Montreal, and the friends back in Italy. Thanks to all of you for the good time and the adventures we have shared together.

Carolina, for always being present and giving me a lot of support during this last year.

Mamma e papà, per avermi dato l'opportunità e la motivazione di andare avanti.

RÉSUMÉ

Le développement des sources térahertz intenses (THz) a connu un grand essor au cours des dernières décennies, en raison de la disponibilité croissante des systèmes laser femtoseconde amplifiés par IR (par exemple les lasers Ti:Sapphire). Récemment, la technologie des lasers à l'ytterbium (Yb) a été reconnue comme une alternative prometteuse aux lasers Ti:Sapphire, offrant des avantages évidents en termes de stabilité, de compacité et de puissance de sortie. Dans la première partie de ce travail de thèse, nous avons étudié la mise en œuvre de sources THz commandées par des impulsions femtoseconde de laser Yb émises à la longueur d'onde centrale de 1030 nm. En particulier, nous avons caractérisé les impulsions THz à champ électrique de crête élevée générées par rectification optique (OR) par un cristal organique HMQ-TMS pompé par des impulsions laser Yb de 170 fs de long dans un schéma colinéaire. En effet, le HMQ-TMS possède une large bande de rectification optique de phase, ce qui lui permet d'être pompé à des longueurs d'onde plus courtes que celles requises par d'autres cristaux organiques (c'est-à-dire 1.3-1.5 μm), tout en conservant un rendement de conversion élevé. De plus, nous avons montré que les impulsions délivrées par le laser Yb amplifié peuvent être comprimées en temps à quelques dizaines de fs au moyen de techniques de compression d'impulsions non linéaires. Ces impulsions laser comprimées ont ensuite été utilisées pour la génération d'impulsions THz à très large bande via une source de plasma bicolore. Dans la deuxième partie de ce projet, nous avons exploité notre source THz HMQ-TMS pour des expériences d'émission d'électrons sur le terrain à THz sur une nouvelle conception de photocathode plasmonique. En particulier, nous avons étudié l'utilisation de nanocones résonants (NCR) THz imprimés en 3D comme nouvelle plateforme d'émission d'électrons ultra-rapide. La réponse électromagnétique des NCR a été optimisée par des simulations numériques, pour obtenir une résonance monopolaire centrée à 1 THz et présentant une amélioration du champ local à haut THz au sommet du NCR. Nous avons montré que les nanostructures peuvent être disposées de manière pratique sous forme de réseau pour améliorer encore l'extraction des électrons par une réponse collective, qui peut également être récoltée par un nanoémetteur individuel. Le processus de photoémission a été caractérisé expérimentalement et les résultats obtenus ont été étayés par des simulations numériques et des modèles analytiques.

Mots-clés: Radiation térahertz; lasers à base d'ytterbium; conception numérique de la réponse électromagnétique; spectroscopie; réseaux résonants de nanostructures; effets non linéaires; physique des champs élevés; photoémission d'électrons; confinement des sous-longueurs d'onde; amélioration du champ local.

ABSTRACT

The development of intense terahertz (THz) sources has experienced a large boost in the last few decades, due to the increasing availability of IR amplified femtosecond laser systems (e.g. Ti:Sapphire lasers). Recently, the ytterbium (Yb) laser technology has been recognized as a promising alternative to Ti:Sapphire lasers, offering clear advantages in terms of stability, compactness and output power. In the first part of this thesis work we have investigated the implementation of THz sources driven by femtosecond Yb-laser pulses emitted at the central wavelength of 1030 nm. In particular, we have characterized the high-peak-electric-field THz pulses generated through optical rectification (OR) by an HMQ-TMS organic crystal pumped by 170-fs-long Yb-laser pulses in a collinear scheme. Indeed, HMQ-TMS possesses a large OR phase-matching band, which allows it to be pumped at wavelengths shorter than those required by other organic crystals (i.e. 1.3-1.5 μm), yet keeping a high conversion efficiency. Moreover, we have shown that the pulses delivered by the amplified Yb-laser can be compressed in time to few tens of fs by means of nonlinear pulse compression techniques. These compressed laser pulses have then been employed for the generation of ultrabroadband THz pulses via a two-color plasma source. In the second part of this project, we have exploited our HMQ-TMS THz source for THz field-driven electron emission experiments on a novel plasmonic photocathode design. In particular, we have investigated the use of 3D-printed THz resonant nanocones (RNCs) as a new platform for ultrafast electron emission. The electromagnetic response of the RNCs has been optimized via numerical simulations, so as to achieve a monopole resonance centered at 1 THz and featuring a high THz local field enhancement at the RNC apex. We have shown that the nanostructures can be conveniently arranged in an array form to further enhance electron extraction via a collective response, which can also be harvested by an individual nanoemitter. The photoemission process has been experimentally characterized, and the results obtained have been supported by both numerical simulations and analytical modelling.

Keywords: Terahertz radiation; ytterbium based lasers; numerical design of the electromagnetic response; spectroscopy; resonant arrays of nanostructures; nonlinear effects; high-field physics; electron photoemission; sub-wavelength confinement; local field enhancement.

TABLE OF CONTENTS

ACKNOWLEDGEMENTS.....	III
RÉSUMÉ	V
ABSTRACT	VI
TABLE OF CONTENTS	VII
LIST OF FIGURES	IX
LIST OF TABLES.....	XI
LIST OF PUBLICATIONS	XIII
LIST OF CONTRIBUTION TO INTERNATIONAL CONFERENCES	XIV
1 INTRODUCTION.....	1
1.1 MOTIVATION AND OUTLINE OF THE THESIS.....	1
1.2 THE RISE OF THz TECHNOLOGY	4
1.2.1 OPTICAL RECTIFICATION IN NONLINEAR CRYSTALS.....	6
1.2.2 NONLINEAR CRYSTALS FOR OPTICAL-RECTIFICATION-BASED THz SOURCES	10
1.2.3 ELECTRO-OPTICAL SAMPLING DETECTION	13
1.2.4 TWO-COLOR PLASMA THz SOURCE AND AIR-BASED-COHERENT-DETECTION	15
1.2.5 THz TIME-DOMAIN SPECTROSCOPY AND DATA ANALYSIS	18
1.3 OPTICAL NANOANTENNAS	21
1.3.1 STRATEGIES TO IMPROVE THE RESONANCE QUALITY: SURFACE LATTICE MODES AND OUT-OF-PLANE CONFIGURATION	23
1.3.2 PLANAR ARRAYS OF THz DIPOLE NANOANTENNAS.....	28
1.3.3 LOCALIZATION OF THz FIELDS IN NANOCAVITIES	30
1.3.4 USE OF THz RESONANT NANOANTENNAS FOR LOCALIZED NONLINEAR PROCESSES.....	35
1.4 ELECTRON PHOTOEMISSION	38
1.4.1 SIMPLE MAN'S MODEL FOR FIELD-DRIVEN PHOTOEMISSION FROM METAL NANOTIPS.....	40
1.4.2 THz FIELD-DRIVEN ELECTRON EMISSION FROM METALLIC NANOSTRUCTURES	43
2 DEVELOPMENT OF YTTERBIUM BASED THz SOURCES	45
2.1 INTENSE THz PULSES FROM HMQ-TMS ORGANIC CRYSTAL PUMPED AT 1030 NM	46
2.1.1 CHARACTERIZATION OF THE HIGH-FIELD THz PULSES.....	47
2.1.2 NONLINEAR TRANSMISSION IN A InGaAs THIN FILM.....	50
2.2 TWO-COLOR PLASMA GENERATION OF ULTRA-BROADBAND HIGH-FIELD THz PULSES	52
2.2.1 SPECTRAL BROADENING AND TEMPORAL COMPRESSION OF Yb-LASER PULSES THROUGH AN Ar-FILLED HOLLOW-CORE FIBER.....	52
2.2.2 CHARACTERIZATION OF THE BROADBAND THz PULSES	55
3 3D-PRINTED THz RESONANT NANOCONES FOR OUT-OF-PLANE ULTRAFAST FIELD-DRIVEN PHOTOEMISSION	59

3.1	NUMERICAL DESIGN AND EXPERIMENTAL CHARACTERIZATION OF THE THz RESPONSE.....	62
3.2	STUDY OF THE THz FIELD-DRIVEN PHOTOEMISSION	66
3.2.1	EXPERIMENTAL SETUP FOR THE FLUORESCENCE MEASUREMENT.....	66
3.2.2	ANALYSIS OF THE FLUORESCENCE MEASUREMENTS.....	68
3.2.3	DIRECT MEASUREMENT OF THE PHOTOEMISSION CURRENT	71
3.3	ELECTRON ENERGY DISTRIBUTIONS CALCULATED VIA THE TWO-STEP ANALYTICAL MODEL.....	74
4	CONCLUSIONS AND FUTURE PERSPECTIVES	78
5	BIBLIOGRAPHY.....	81
6	APPENDIX I	92
6.1	THEORETICAL MODELING TO RETRIEVE THE THz INTENSITY SPECTRUM	92
7	APPENDIX II.....	93
7.1	SELF PHASE MODULATION.....	93
8	SOMMAIRE RÉCAPITULATIF.....	95

LIST OF FIGURES

FIGURE 1.1 THE THz RANGE DEPICTED IN THE ELECTROMAGNETIC SPECTRUM	4
FIGURE 1.2 SCHEMATIC OF THz GENERATION THROUGH OPTICAL RECTIFICATION	6
FIGURE 1.3 THz GENERATION VIA OR IN ZnTe AND GaP CRYSTALS	10
FIGURE 1.4 TILTED-PULSE-FRONT SCHEME FOR OR IN LiNbO ₃	11
FIGURE 1.5 COHERENCE LENGTH AND THz SPECTRA OF ORGANIC CRYSTALS.....	12
FIGURE 1.6 ELECTRO-OPTICAL SAMPLING	13
FIGURE 1.7 TWO-COLOR-PLASMA-BASED THz SOURCE AND ABCD DETECTION SCHEMES	15
FIGURE 1.8 SCHEMATIC OF A THz-TDS SETUP	18
FIGURE 1.9 ANALYSIS OF A THz-TDS MEASUREMENT	19
FIGURE 1.10 OPTICAL PLASMONIC NANOANTENNAS.....	21
FIGURE 1.11 SKETCH HIGHLIGHTING THE PRIMARY LATTICE MODES.....	23
FIGURE 1.12 EFFECT ON INDUCED CHARGES WHEN THE ANTENNA IS PLACED OVER A METALLIC SUBSTRATE.....	25
FIGURE 1.13 COMPARISON BETWEEN MONOPOLAR AND DIPOLAR RESONANCES.....	26
FIGURE 1.14 LATTICE MODE CHARACTERIZATION.....	27
FIGURE 1.15 ARRAY OF THz DIPOLE NANOANTENNAS.....	28
FIGURE 1.16 FANO COUPLING IN THz NANOGAPS	30
FIGURE 1.17 STRONG COUPLING IN THz NANOGAPS	31
FIGURE 1.18 ANALYTICAL AND NUMERICAL INVESTIGATION OF THz TAPERED NAS	32
FIGURE 1.19 EXPERIMENTAL CHARACTERIZATION OF THz TAPERED NAS	33
FIGURE 1.20 NONLINEAR EXPERIMENTS WITH THz NAS	36
FIGURE 1.21 ENERGY SCHEMATIC FOR PHOTOEMISSION PROCESSES	38
FIGURE 1.22 ELECTRON PHOTOEMISSION FROM METALLIC NANOTIPS.....	41
FIGURE 2.1 THz SPECTRA AND COHERENCE LENGTH FOR HMQ-TMS.....	46
FIGURE 2.2 TDS SETUP USED FOR THE CHARACTERIZATION OF THE HMQ-TMS THz SOURCE.....	47
FIGURE 2.3 THz WAVEFORM AND SPECTRUM GENERATED BY OR IN HMQ-TMS CRYSTAL.....	48
FIGURE 2.4 THz ELECTRIC FIELD PEAK AND ENERGY SCALING VERSUS PUMP FLUENCE.....	49

FIGURE 2.5 Z-SCAN MEASUREMENT	50
FIGURE 2.6 ULTRABROADBAND THz PULSES GENERATED BY USING A Ti:SAPPHIRE LASER.....	53
FIGURE 2.7 COMPRESSED PULSE CHARACTERIZATION	54
FIGURE 2.8 SCHEMATIC OF THE SETUP FOR THE GENERATION AND CHARACTERIZATION OF BROADBAND THz PULSES....	55
FIGURE 2.9 ELECTRIC-FIELD WAVEFORM AND SPECTRUM OF THE ULTRABROADBAND THz SOURCE.....	56
FIGURE 2.10 TRANSMISSION OF THE EMPLOYED FILTER.....	57
FIGURE 2.11 ULTRABROADBAND THz GENERATION AS A FUNCTION OF THE INPUT PULSE ENERGY	58
FIGURE 3.2 MODEL OF A THz RESONANT RNC	62
FIGURE 3.3 THz FREQUENCY RESPONSES OF THE INVESTIGATED RNCs	64
FIGURE 3.4 NUMERICAL SIMULATION OF A NC SURROUNDED BY JUST 8 CYLINDERS.....	65
FIGURE 3.5 EXPERIMENTAL SETUP FOR THE FLUORESCENCE MEASUREMENTS	66
FIGURE 3.6 FLUORESCENCE MEASUREMENTS	67
FIGURE 3.7 FN PLOTS OF THE FLUORESCENCE MEASUREMENTS.....	68
FIGURE 3.8 PHOTOCURRENT MEASUREMENTS.....	71
FIGURE 3.9 NUMERICAL EVALUATION OF THE SPATIAL SPREAD OF THE ELECTRON BUNCH.....	72
FIGURE 3.10 SEM IMAGES OF THE ARRAY OF RNCs TAKEN AFTER THE CHARACTERIZATION EXPERIMENTS.....	73
FIGURE 3.11 SPATIAL AND TEMPORAL DEPENDENCE OF THE THz NEAR-FIELD	74
FIGURE 3.12 TIME DEPENDENCE OF NEAR FIELD QUANTITIES	75
FIGURE 3.13 ENERGY DISTRIBUTIONS OF THE PHOTOEMITTED ELECTRONS FROM THE DIFFERENT NANOSTRUCTURES	76
FIGURE 7.1 SELF-PHASE MODULATION OF A GAUSSIAN OPTICAL PULSE.....	94

LIST OF TABLES

TABLE 1.1	ELECTRO-OPTIC COEFFICIENTS OF SOME THZ EMITTERS.....	9
TABLE 3.1	GEOMETRICAL PARAMETERS OF THE DIFFERENT SIMULATED NANOSTRUCTURES	63
TABLE 3.2	RESULTS FROM THE ANALYSIS FLUORESCENCE MEASUREMENT	70

LIST OF PUBLICATIONS

- [1] R. Piccoli, A. Rovere, A. Toma, R. Morandotti, L. Razzari, (2017). *Terahertz nanoantennas for enhanced spectroscopy*. Terahertz Spectroscopy: A Cutting Edge Technology, 21 IN-TECH, Vienna, Austria (Book Chapter).
- [2] A. Rovere, Y.-G. Jeong, R. Piccoli, S.-H. Lee, S.-C. Lee, O-P. Kwon, M. Jazbinsek, R. Morandotti, L. Razzari, (2018). *Generation of high-field terahertz pulses in an HMQ-TMS organic crystal pumped by an ytterbium laser at 1030 nm*. Opt. Express, 26, 2509-2516.
- [3] X. Jin, A. Cerea, G. C. Messina, A. Rovere, R. Piccoli, F. De Donato, F. Palazon, A. Perucchi, P. Di Pietro, R. Morandotti, S. Lupi, F. De Angelis, M. Prato, A. Toma, L. Razzari, (2018). *Reshaping the phonon energy landscape of nanocrystals inside a terahertz plasmonic nanocavity*. Nature Commun., 9, 763.
- [4] R. Piccoli, A. Rovere, Y.-G. Jeong, Y. Jia, L. Zanotto, F. Légaré, B.E. Schmidt, R. Morandotti, L. Razzari, (2019). *Extremely broadband terahertz generation via pulse compression of an ytterbium laser amplifier*. Opt. Express, 27, 32659.
- [5] V. Aglieri, X. Jin, A. Rovere, R. Piccoli, D. Caraffini, S. Tuccio, F. De Angelis, R. Morandotti, R. Macaluso, A. Toma, L. Razzari, (2020). *Improving nanoscale terahertz field localization by means of sharply tapered resonant nanoantennas*. Nanophotonics 9, 683.
- [6] P. A. Carpeggiani, G. Coccia, G. Fan, E. Kaksis, A. Pugžlys, V. Cardin, F. Légaré, A. Baltuška, R. Piccoli, Y.-G. Jeong, A. Rovere, R. Morandotti, L. Razzari, B. E. Schmidt, A. A. Voronin, A. Zheltikov, (2020). *Extreme Raman red shift: ultrafast multimode non-linear space-time dynamics, pulse compression, and broadly tunable frequency conversion*. Optica 7, 1349-1354.
- [7] A. Rovere, R. Piccoli, A. Bertoncini, Y.-G. Jeong, S. Payeur, F. Vidal, S.-H. Lee, J.-H. Seok, O-P. Kwon, R. Morandotti, C. Liberale, L. Razzari, (2020). *3D-Printed Photocathodes for Resonant, Terahertz-Field-Driven Ultrafast Electron Emission*. ArXiv: 2010.12098.

LIST OF CONTRIBUTIONS TO INTERNATIONAL CONFERENCES

- [1] A. Rovere, A. Toma, M. Prato, A. Bertoncini, A. Cerea, R. Piccoli, A. Perucchi, P. Di Pietro, F. De Angelis, L. Manna, R. Morandotti, C. Liberale, L. Razzari, (2016). *Conical nanoantenna arrays for terahertz light*. Conference: Photonics North.
- [2] A. Rovere, Y.-G. Jeong, R. Piccoli, S.-H. Lee, S.-C. Lee, O-P. Kwon, M. Jazbinsek, R. Morandotti, L. Razzari, (2017). *High-energy terahertz pulse source based on an HMQ-TMS organic crystal pumped at 1030 nm*. Conference: Photonics North.
- [3] A. Rovere, Y.-G. Jeong, R. Piccoli, S.-H. Lee, S.-C. Lee, O-P. Kwon, M. Jazbinsek, R. Morandotti, L. Razzari, (2018). *High-field terahertz pulses generated in an HMQ-TMS organic crystal pumped by an amplified ytterbium laser*. CLEO: QELS_Fundamental Science, JW2A. 81.
- [4] X. Jin, A. Cerea, G. C. Messina, A. Rovere, R. Piccoli, R. Morandotti, F. De Angelis, A. Toma, L. Razzari, (2018). *Modeling light-matter interaction in terahertz plasmonic nanocavities*. Conference: Photonics North (Aspnes & Studna).
- [5] A. Rovere, Y.-G. Jeong, R. Piccoli, S.-H. Lee, S.-C. Lee, O-P. Kwon, M. Jazbinsek, R. Morandotti, L. Razzari, (2018). *Intense THz pulses from HMQ-TMS organic crystal pumped at 1030 nm*. International Conference on Advanced Materials Processing.
- [6] X. Jin, A. Cerea, G. C. Messina, A. Rovere, R. Piccoli, F. De Donato, F. Palazon, A. Perucchi, P. Di Pietro, R. Morandotti, S. Lupi, F. De Angelis, M. Prato, A. Toma, L. Razzari, (2019). *Modifying the optical phonon response of nanocrystals inside terahertz plasmonic nanocavities*. The European Conference on Lasers and Electro-Optics.
- [7] V. Aglieri, X. Jin, A. Rovere, R. Piccoli, R. Morandotti, R. Macaluso, A. Toma, L. Razzari, (2019). *Antenna tapering strategy for near-field enhancement optimization in terahertz gold nanocavities*. The European Conference on Lasers and Electro-Optics.
- [8] A. Rovere, A. Bertoncini, R. Piccoli, Y.-G. Jeong, S. Payeur, F. Vidal, O-P. Kwon, S.-H. Lee, R. Morandotti, C. Liberale, L. Razzari, (2020). *Out of plane electron emission via 3D printed terahertz resonant nanocones*. Photonics West Conference: Terahertz, RF, Millimeter, and Submillimeter-Wave Technology and Applications XIII.
- [9] A. Rovere, R. Piccoli, A. Bertoncini, Y.-G. Jeong, S. Payeur, F. Vidal, O-P. Kwon, S.-H. Lee, R. Morandotti, C. Liberale, L. Razzari, (2020). *3D-printed arrays of terahertz resonant nanocones*. Conference: Photonics North.

1 INTRODUCTION

1.1 Motivation and outline of the thesis

In the last decades, the number of research studies and applications involving terahertz (THz, $1 \text{ THz} = 10^{12} \text{ Hz} = 4.1 \text{ meV} = 33.3 \text{ cm}^{-1}$, where 1 THz corresponds to a wavelength of $300 \mu\text{m}$) frequencies has known an impressive boost, especially thanks to the growing availability of amplified femtosecond lasers. Indeed, such optical sources have paved the way for the development of new techniques based on nonlinear optics for the generation and detection of THz pulses, such as *optical rectification* (OR) and *electro-optical sampling* (EOS) (Dexheimer, 2007). In particular, high-field THz pulses are of great interest to investigate the nonlinear response of matter systems at these frequencies, also allowing coherent time-domain studies (Hafez et al., 2016). In recent years, Yb-based laser technology has been found to offer both higher thermal stability and average output power than traditionally used Ti:Sapphire laser systems, which can allow further improvements for the development of table-top THz sources. Nevertheless, there are still some issues related to the implementation of intense THz sources pumped at 1030 nm (i.e., the emission wavelength of Yb-lasers). For instance, LiNbO₃ crystals present a high nonlinear coefficient, which ensures high-efficiency THz generation through OR. However, a complex, non-collinear pumping scheme is needed to achieve the necessary phase matching condition at 1030 nm, which requires a non-trivial alignment (Hebling et al., 2002). On the other hand, organic nonlinear crystals (e.g. DAST, OH1) offer a promising alternative for efficient generation of intense THz pulses, since they feature a high nonlinear response and can be pumped in a collinear scheme (Hauri et al., 2011; Kwon et al., 2008). However, the optimal wavelength to fulfill the phase matching condition in these crystals typically lies in the range of 1.3-1.5 μm , thus requiring a further optical parametric amplifier to be coupled to the femtosecond laser system.

In the first part of my thesis project, I characterized the high-field THz pulses emitted by a 2-(4-hydroxy-3-methoxystyryl)-1-methylquinolinium 2,4,6-trimethylbenzenesulfonate (HMQ-TMS) organic crystal collinearly pumped by an amplified Yb laser system. Moreover, I employed these intense THz pulses in a proof-of-principle nonlinear experiment (saturation of absorption in a doped semiconducting thin film), thus showing the potential of this novel configuration for the exploration of THz nonlinear effects (Rovere et al., 2018).

At the same time, the gain bandwidth of Yb lasers limits the pulse duration in the 250 fs - 130 fs range. In order to solve this issue, nonlinear pulse compression techniques can be employed, ensuring the

reduction of the pulse duration down to few tens of femtoseconds (Jeong et al., 2018). Thus, in a collaboration project, I exploited these compressed pulses to generate extremely broadband (up to 60 THz), high-field THz pulses via a two-color plasma source (Piccoli et al., 2019). This source can extend nonlinear THz investigations to frequencies that are particularly relevant for optical phonon dynamics in condensed matter systems.

The use of intense THz pulses is also very appealing for the extraction and acceleration of electron bunches through the field-driven photoemission from metallic nanostructures. In fact, THz radiation ensures a purely field-driven emission process. Moreover, the electrons are extracted and accelerated within a half optical cycle, thus enabling electron emission in phase with the driving electromagnetic pulse. The intrinsic carrier-envelope phase stability of OR-generated THz pulses can thus provide a precise coherent control of the extracted electron bunches (Yoshioka et al., 2013). Traditionally, non-resonant metal nanotips have been investigated for THz-driven photoemission (Herink et al., 2014; Li & Jones, 2016). In more recent studies, the higher field enhancement granted by planar resonant antennas has been exploited, enabling electron photoemission at lower incident field amplitudes (Iwaszczuk et al., 2014; Zhang et al., 2015). However, the close proximity of the substrate underneath the planar antennas hampers the practical use of the emitted electron bunches for many applications.

In the second part of this PhD project, I have thus employed the high-field THz pulses generated from the organic-crystal source to investigate THz field-driven electron photoemission from rationally-designed resonant photocathodes (Rovere et al., 2020). In particular, I have investigated the use of vertical THz resonant nanocones (RNCs) for out-of-plane field-driven electron photoemission. First, I have optimized the design via numerical simulations to tune their resonance at the source frequency peak. Furthermore, I have studied the RNC arrangement into an array form, finding that this enables a further increase in the local electric field via a collective terahertz response. Remarkably, we have proven that such collective behavior can also be used to boost the local THz field on an individual nanoemitter, by engineering an array of resonant microstructures with a single RNC in the middle. The samples have been fabricated by our collaborators at KAUST using a 3D printing nanolithography method. Our optical and electrical characterizations of the fabricated devices have confirmed the advantages of the proposed designs for THz-driven electron extraction, which have also been corroborated by further numerical and analytical modelling of the photoemission process.

The outline of the thesis is presented below:

In Chapter 1, the key theoretical concepts and the most relevant literature are introduced, such as for what concerns the generation and detection of THz pulses, the properties of resonant nanoantennas (NAs), also considering the possible strategies to improve their electromagnetic response and some possible applications, as well as the state of the art of field-driven electron photoemission from metallic nanotips.

In Chapter 2, the results regarding the two developed high-field THz sources are reported. First, the characterization of the intense THz pulses emitted via OR in the HMQ-TMS organic crystal, collinearly pumped by a Yb-based laser amplifier is presented. Then, the description of the extremely broadband THz pulses generated via a two-color-plasma technique using the Yb-laser compressed pulses is shown.

Chapter 3 includes the outcomes of the project regarding THz-driven photoemission from the 3D printed RNCs. In particular, the numerical design of the different investigated nanostructures and the subsequent characterization of their THz response is first presented. Then, the photoemission properties of the various fabricated samples are studied via optical (electron-induced gas fluorescence) and electrical measurements, complemented by numerical and analytical photoemission modelling.

Finally, in Chapter 4 the conclusions and future perspectives of this PhD project are discussed.

1.2 The rise of THz technology

Optics is the branch of physics which regards the study of the fundamental properties of light as well as the investigation of its interaction with matter. Between the end of the XIX century and the first half of the XX century, the understanding of optics has experienced enormous advances, in particular thanks to the *electromagnetic theory* from Maxwell's equations (Maxwell, 1865) and the interpretation of the *wave-particle duality* of light in the framework of quantum physics (Einstein, 1905). These theoretical concepts put the basis for the development of the first *laser* (the acronym standing for *light amplification by stimulated emission of radiation*) in 1960 (Maiman, 1960), which had a huge impact both in scientific research and in everyday life. Finally, the availability of intense laser sources opened the access to the exploration of *nonlinear optical phenomena* (Boyd, 2008), enabling the full control of the generation, detection and manipulation of light in the spectral range that goes from the infrared to the ultraviolet frequencies. This technological revolution in optics led to the birth of a new branch of applied physics research called *photonics*.

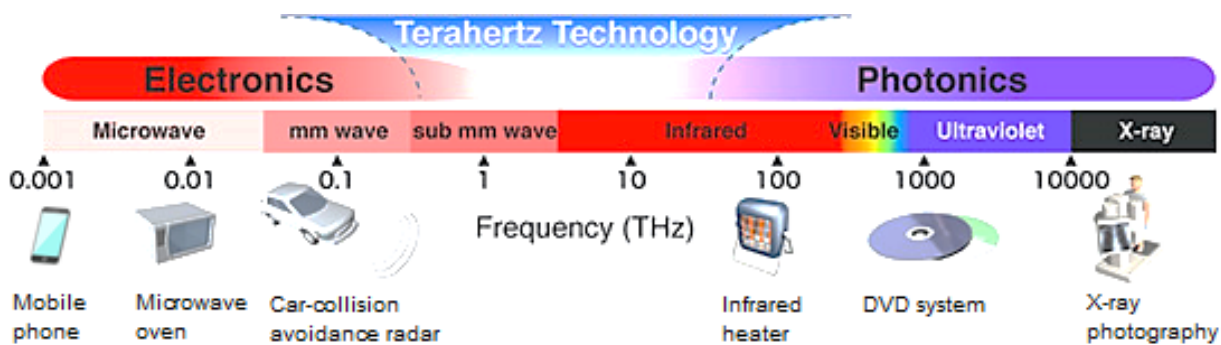


Figure 1.1 The THz range depicted in the electromagnetic spectrum
Reprinted with permission from (Fukunaga & Picollo) © 2010 Springer Nature.

In the last few decades, scientific advances in optics have made it possible to fully explore the THz frequency range, which is located in the electromagnetic spectrum between the infrared and the microwave region and is conventionally limited between 100 GHz and 10 THz. In fact, this spectral range has long been called the "*THz gap*", due to the lack of sources and detectors working at THz frequencies, which were beyond the capabilities of both electronics and conventional photonics devices (Figure 1.1). THz radiation has always been appealing for its peculiar characteristics and possible applications.

For instance, since many kinds of materials (e.g. paper, wood, bricks, clothes, and ceramics) are transparent to THz radiation, it can be employed for quality checking of products (Rutz et al., 2006), security controls (John et al., 2005) and analysis of cultural heritage (Fukunaga & Picollo, 2010).

Moreover, since THz radiation is at the same time non-ionizing and strongly absorbed by water, it can become a non-threatening alternative to X-rays for medical imaging of organic tissues (Yu et al., 2012). Furthermore, the energy scale of many collective excitations in solid-state systems (e.g. optical phonons, magnons, plasmons, etc.) and the rotational-vibrational transitions of molecules are comparable with the energy of THz photons, making THz applicable for sensing and spectroscopy (Dexheimer, 2007).

The development of efficient THz sources based on the use of intense femtosecond near-IR pulses opened the way to THz experiments at the table-top scale (Grischkowsky et al., 1990). In particular, OR and two-color plasma mixing are two common nonlinear processes employed for the generation of coherent sub-picosecond single-cycle THz pulses. Another strategy to generate and detect THz pulses is based on the use of photoconductive antennas (PCA). Since a detailed description of PCA-based methods is beyond the scope of this Thesis, we direct the interested reader to (Hafez et al., 2016) for an overview. Ultrafast THz pulses are generally used to perform broadband and time-resolved measurements in a time-domain system (THz-TDS). In some cases, the generated THz pulses can reach electric field peaks between hundreds of kV/cm and few MV/cm (Blanchard, Sharma, Razzari, Ropagnol, Bandulet, Vidal, & Morandotti, 2011), which makes them suitable to investigate nonlinear effects in numerous systems, such as: THz intervalley electron scattering in n-doped semiconductor(Razzari et al., 2009), THz nonlinear response of topological insulators (Giorgianni et al., 2016), THz high-harmonic generation in graphene(Hafez et al., 2018), THz induced molecular orientation and alignment (Fleisher et al., 2011) and THz field-driven electron photoemission from metallic nanotips (Li & Jones, 2016). Moreover, the availability of high-field THz pulses has also enabled the observation of the nonlinear process dynamics at their fundamental timescales through different pump-probe spectroscopy schemes (Hoffmann et al., 2009; Tarekegne et al., 2017).

In the next paragraphs, different kinds of table-top THz sources and coherent detection techniques will be described, introducing some fundamental notions (such as phase-matching condition, coherence length, spectral bandwidth, etc.) and the standard analysis procedure for the time-domain measurements. In particular, we will focus our attention on some cases of interest related to this thesis project.

1.2.1 Optical rectification in nonlinear crystals

In the framework of light-matter interaction, nonlinear optics involves all the optical processes where the response of a material system depends on the strength of the applied optical field in the nonlinear medium (Boyd, 2008). For instance, second harmonic generation (SH, i.e. the generation of light at twice the frequency of the excitation light field), which has been experimentally demonstrated briefly after the invention of the laser (Franken et al., 1961), is a nonlinear optical process featuring a quadratic scaling with the intensity of the input optical beam.

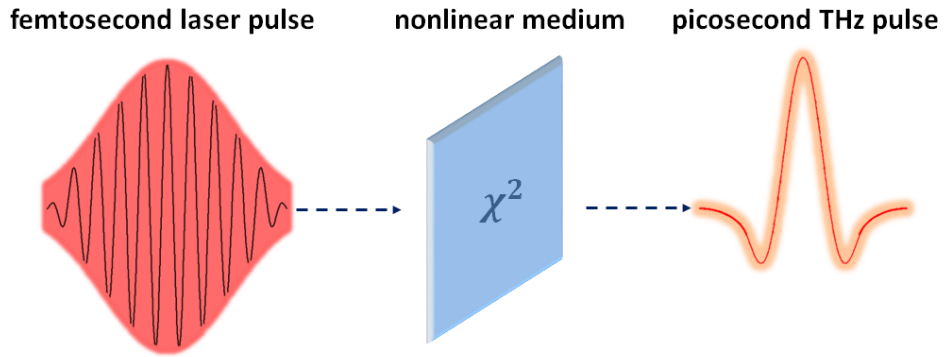


Figure 1.2 Schematic of THz generation through optical rectification

The *polarization* of a material $P(t)$ (i.e. the dipole moment per unit volume) plays a key role in the description of nonlinear optical phenomena because the time-varying polarization can act as a source of new electromagnetic components. In general, $P(t)$ can be expressed through a perturbative expansion of the field strength $E(t)$:

$$P(t) = \chi^{(1)}E(t) + \chi^{(2)}E^2(t) + \chi^{(3)}E^3(t) \dots \quad (1.1)$$

where $\chi^{(n)}$ is the n^{th} order *susceptibility* of the material. For low field intensities, the linear term, $\chi^{(1)}E(t)$ dominates the expansion, whereas for higher intensities also the other terms of the expansion start to become relevant. The quantities $\chi^{(2)}$ and $\chi^{(3)}$ are the second and third-order nonlinear optical susceptibilities, respectively. These two terms lead to different kinds of nonlinear optical phenomena. A fundamental condition for second-order nonlinear optical processes is that they can occur only in non-centrosymmetric media, i.e. media that do not display spatial inversion symmetry. Liquids, gases, amorphous solids (such as glass), and even many crystals, cannot produce second-order nonlinear optical interactions since they present inversion symmetry and consequently $\chi^{(2)} = 0$ for such media. Differently, third-order nonlinear optical interactions can occur for both centrosymmetric and non-centrosymmetric media. In particular, OR is a second-order

nonlinear process that takes place when an intense optical beam passes through a medium inducing the generation of a DC polarization. Let us consider two electric fields $E_1(t) = E_0 \cos(\omega_{01}t)$ and $E_2(t) = E_0 \cos(\omega_{02}t)$, with amplitude E_0 and oscillating at the two frequencies ω_{01} and ω_{02} , respectively. The second term of the expansion of Equation (1.1) becomes:

$$\begin{aligned} P_2(t) &= \chi^{(2)} E_1(t) E_2(t) = \chi^{(2)} \frac{E_0^2}{2} (\cos(\omega_{01} + \omega_{02})t + \cos(\omega_{01} - \omega_{02})t) \\ &= P_2^\Sigma(\omega_{01} + \omega_{02}) + P_2^\Delta(\omega_{01} - \omega_{02}) \end{aligned} \quad (1.2)$$

As one can see, the second order nonlinear polarization is formed by two terms, the first P_2^Σ proportional to the sum frequency and the second P_2^Δ proportional to the difference frequency among the two fields. OR can be conceptually understood as a special case of *difference frequency generation* (DFG) where $\omega_{01} = \omega_{02}$, which leads to the emission of a much lower frequency falling in the THz region, ω_{THz} . Note that the exact rectification process would require $\omega_{01} = \omega_{02}$ and the generation of a DC field in the crystal. Hereon, OR is loosely defined as a DFG process in which $\omega_{01} - \omega_{02} = \omega_{\text{THz}} \ll \omega_{01}, \omega_{02}$. If we now consider a femtosecond IR laser pulse with finite bandwidth, we can envision the DFG mixing between all the frequency pairs within the IR pulse spectrum. The sum of all these contributions results in the generation of a THz spectrum with finite bandwidth. Let's now consider a laser pulse with a Gaussian time profile, $E(t) = E_0 \exp(i\omega_0 t) \exp(-t^2/\tau^2)$, where ω_0 is the central frequency and τ is the pulse duration. Thus, according to the far-field solution to the wave equation (Benicewicz et al., 1994) the time profile of the generated THz pulse, $E_{\text{THz}}(t)$, will be proportional to the second time derivative of the 2nd order polarization term related to OR, $P_2^\Delta(t)$, as it is shown in Figure 1.2, which is determined by the Gaussian profile of the laser pulse:

$$E_{\text{THz}}(t) = \frac{\partial^2 P_2^\Delta(t)}{\partial t^2} = \chi^{(2)} \frac{\partial^2 E^2(t)}{\partial t^2} \quad (1.3)$$

As for any other kind of nonlinear optical process, also for OR the energy and momentum conservation among the interacting fields has to be satisfied:

$$\begin{cases} \Delta\omega_0 = \omega_{01} - \omega_{02} = \omega_{\text{THz}} \\ \Delta k_0 = k_{01} - k_{02} = k_{\text{THz}} \end{cases} \quad (1.4)$$

Dividing side by side the two equations, we get the characteristic *phase matching condition* for THz generation from OR:

$$v_{G,0} = \frac{\partial \omega_0}{\partial k_0} = \frac{\omega_{\text{THz}}}{k_{\text{THz}}} = v_{\text{ph,THz}} \quad (1.5)$$

where $v_{G,0}$ and $v_{\text{ph,THz}}$ are the group velocity of the pump optical beam and the phase velocity of the THz wave, respectively. In general, the pump optical pulse and the generated THz wave propagate with different speeds in the nonlinear medium, due to the dispersion of its refractive index. Thus, a substantial conversion efficiency is possible only if the phase matching of the nonlinear interaction is achieved, or if the phase mismatch within the crystal length is not too large. A *coherence length*, determined by the phase matching condition, can be conveniently defined as the length of the nonlinear medium wherein there is a gain in the optical to THz conversion process. The coherence length for THz generation via OR with a femtosecond infrared laser pulse can be written as:

$$l_c(\omega_{\text{THz}}) = \frac{\pi c}{\omega_{\text{THz}} |n_{o \text{ eff}}(\omega_o) - n_{\text{THz}}(\omega_{\text{THz}})|} \quad (1.6)$$

with

$$n_{o \text{ eff}} = n_o(\omega) - \lambda_o \left(\frac{\partial n_o}{\partial \lambda} \right) \Big|_{\lambda_o} \quad (1.7)$$

where c is the speed of light in vacuum, ω_{THz} is the THz frequency, ω_o (λ_o) the near-infrared excitation frequency (wavelength), n_{THz} and n_o are the refractive index at THz and near-infrared frequencies and $n_{o \text{ eff}}$ is the group refractive index of the femtosecond near-infrared laser pulse. Thus, the coherence length is an important parameter to determine the proper thickness of the nonlinear crystal for the best conversion efficiency. At the same time, the THz emission bandwidth also needs to be properly considered, since it typically reduces by increasing the crystal thickness. Thus, there is often a trade-off to be considered between the achievable bandwidth and the intensity of the generated THz pulses. In principle, the spectral bandwidth of the generated THz pulse strictly depends on the temporal duration of the pump pulse. For instance, a laser pulse of duration $\tau = 100$ fs can lead to the generation of THz pulses with $1/\tau \approx 10$ THz bandwidth. However, the final bandwidth is practically limited by imperfect phase matching conditions (as mentioned above) or by the possible presence of phonon absorptions in the nonlinear crystal. The *electro-optic coefficient* of the crystal, r_{ijk} is a key parameter that gives a quantitative estimation of the nonlinear characteristics of the material (Boyd, 2008), and depends on the second order susceptibility tensor elements, $\chi_{ijk}^{(2)}$, through the following relationship:

$$r_{ijk} = -\frac{2\varepsilon_0}{\varepsilon_{ii}\varepsilon_{jj}} \chi_{ijk}^{(2)} \quad (1.8)$$

where ε_{ij} , and ε_0 are the effective permittivity tensor elements and the vacuum permittivity, respectively. It is possible to introduce a compact (Voigt) notation for the electro-optic tensor elements, since they are intrinsically symmetric (i.e., $r_{ijk} = r_{jik}$), due to the fact that ε_{ij} is a Hermitian tensor. Thus, the intrinsic permutation symmetry is used to contract the first two subscripts, $r_{ijk} \rightarrow r_{lk}$ (Sutherland, 2003). The electro-optic coefficients of a few common nonlinear crystals employed for OR are reported in Table 1.1.

Table 1.1 Electro-optic coefficients of some THz emitters (Blanchard, Sharma, Razzari, Ropagnol, Bandulet, Vidal, Morandotti, et al., 2011; Dexheimer, 2007)

Material	Electro-optic coefficient (pm/V)
ZnTe	$r_{41} = 4.04$ (@ 633 nm)
GaP	$r_{41} = 0.97$ (@ 800 nm)
GaSe	$r_{22} = 14.4$ (@ 800 nm)
LiNbO ₃	$r_{33} = 30.9$ (@ 633 nm) $r_{51} = 32.6$ (@ 633 nm)
LiTaO ₃	$r_{33} = r_{13} = 30.5$ (@ 820 nm)
DAST	$r_{11} = 160$ (@ 820 nm)

The orientation of the crystal with respect to the incident polarization thus plays an important role for an efficient THz generation. For instance, zinc telluride (ZnTe), gallium phosphide (GaP) and gallium selenide (GaSe) are common semiconductor materials both used for THz generation and detection depending on the wavelength of the optical pump beam. All three crystals are uniaxial, which means that they have only one axis of rotational symmetry referred to as the c-axis or optical axis of the crystal. In general, the polarization of the pump beam has to be properly selected with respect to the optical axis of the crystal to maximize the emission efficiency. Therefore, efficient THz generation via OR requires transparent single crystals with high second-order nonlinearity (i.e. large electro-optic coefficient), a thickness comparable with the coherence length, and an appropriate choice of axes orientation with respect to the polarization of the pump beam. In the next section, some common nonlinear crystals used for OR will be presented.

1.2.2 Nonlinear crystals for optical-rectification-based THz sources

Several kinds of electro-optic materials have been employed for THz generation via OR, such as various semiconductors (e.g. ZnTe, ZnSe, GaSe, GaP) and inorganic oxide crystals (e.g. LiNbO₃, LiTaO₃). In particular, zinc telluride (ZnTe) and gallium phosphide (GaP) are two nonlinear crystals presenting a fairly good phase matching for pump wavelengths at 800 nm and 1030 nm, respectively (i.e., the emission wavelengths of Ti:Sapphire and Yb-lasers). Examples of measured waveforms and the corresponding spectra of the THz pulses generated by OR in these two crystals are shown in Figure 1.3. It is important to note that the achievable THz spectral bandwidth from these crystals is limited by the phonon absorptions located at 5.4 THz for ZnTe and 11 THz for GaP. Moreover, the rectified THz pulses from these crystals cannot provide electric fields larger than 100 kV/cm, due to multiphoton absorption which leads to the saturation of the THz conversion efficiency at high pump energies, unless large-area crystals are used (Blanchard et al., 2007).

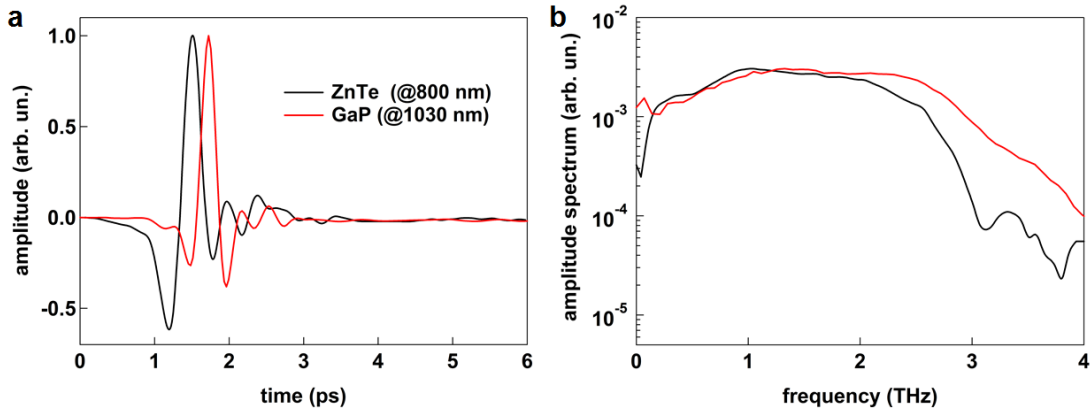


Figure 1.3 THz generation via OR in ZnTe and GaP crystals

(a) THz waveforms generated by OR pumping a <110> ZnTe crystal at 800 nm (Black) and a <110> GaP crystal at 1030 nm (Keathley et al.). Both crystals are 0.5-mm-thick. The pump pulse duration in the two cases are 30 fs and 170 fs, respectively. (b) Corresponding frequency spectra obtained via Fourier transformation. Adapted from (Blanchard, Sharma, Razzari, Ropagnol, Bandulet, Vidal, Morandotti, et al.) © 2011 IEEE.

Lithium niobate (LiNbO₃) is an inorganic crystal that is commonly used to obtain intense THz pulses, due to its high damage threshold, suitable transparent range, low absorption coefficient and a much higher electro-optic coefficient (30.9 pm/V) compared to the one of ZnTe (4.04 pm/V) and GaP (0.97 pm/V). However, the OR conversion efficiency for this crystal is severely limited, in a collinear configuration, by the large refractive index mismatch between the optical pump and the THz wave. Indeed, in LiNbO₃ the optical pump pulse propagates faster than the generated THz pulse, so that the latter is radiated into a Cherenkov cone forming an angle $\gamma = \arccos(\nu_{\text{ph,THz}}/\nu_{G,0})$ with respect to the propagation vector of the pump pulse. In order to overcome this problem, Hebling *et al.* proposed a *tilted pulse front excitation scheme* for a non-collinear generation geometry (Hebling et al., 2002),

where the pump pulse front is tilted by an angle γ inside the LiNbO₃ crystal, by using a grating and two cylindrical lenses (Figure 1.4a). This technique allows the generation of intense single-cycle THz pulses with focused peak fields of the order of MV/cm (Hirori et al., 2011). However, the spectral bandwidth of the THz pulses generated via OR in LiNbO₃ is usually limited to about 1 THz (full width half maximum, FWHM), with a central frequency below 1 THz (Figure 1.4b).

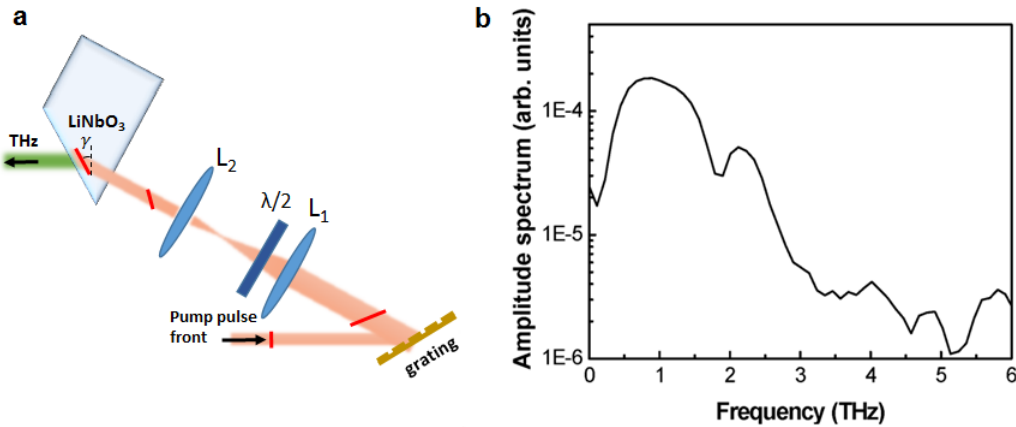


Figure 1.4 Tilted-pulse-front scheme for OR in LiNbO₃

(a) Scheme of the tilted pulse front excitation. L1 and L2 are two cylindrical lenses for the telescope, while $\lambda/2$ is a half-wave plate. (b) Amplitude spectrum of the THz pulses generated via OR in LiNbO₃. Adapted from (Blanchard, Sharma, Razzari, Ropagnol, Bandulet, Vidal, Morandotti, et al.) © 2011 IEEE.

On the other hand, organic crystals (e.g. DAST, DSTMS, OH1, HMQ-TMS, etc.) are known to offer an efficient intense THz generation (Hauri et al., 2011; Kwon et al., 2008; Schneider et al., 2006; Vicario et al., 2015), providing a higher nonlinear response than inorganic crystals. For example, DAST presents a nonlinear optical coefficient $d_{11} = 290 \text{ pm/V}$ at $1.5 \mu\text{m}$, corresponding to an electro-optic coefficient $r_{11} = 47 \text{ pm/V}$ at $1.5 \mu\text{m}$ ($r_{11} = 77 \text{ pm/V}$ at 800 nm) (Schneider et al., 2006). High THz peak electric fields up to few MV/cm (Hauri et al., 2011) can thus be generated by pumping these organic crystals in a collinear geometry. Notwithstanding this, the optimal pump wavelength to fulfill the phase matching condition typically lies in the range $1.3\text{-}1.5 \mu\text{m}$, thus usually requiring an optical parametric amplifier (OPA) to be coupled to the femtosecond laser system as a pumping source. Beside the increase in complexity and related cost of the required optical pump source, the use of OPAs inevitably decreases the overall conversion efficiency, and also leads to additional drawbacks related to transverse irregularities and hot spots often present in the output beam profile of OPAs as well as shot-to-shot amplitude fluctuations, which further limit the maximum usable fluence to pump the OR crystal. An interesting alternative was reported by (Vicario et al., 2015), who demonstrated the generation of high-energy THz pulses from DAST, DSTMS and OH1 organic crystals collinearly pumped by 30 mJ , 100 fs pulses centered at $1.25 \mu\text{m}$ delivered by an amplified Cr:Forsterite laser, obtaining broadband emission spectra between 0.1 and 4 THz (FWHM) with peak electric fields of

several MV/cm (Figure 1.5). However, as Ti:Sapphire laser, also Cr:Forsterite has to be pumped by another bulky laser (usually Nd:YAG), which limits the overall efficiency and compactness of these sources. Alternatively, Yb-doped laser systems can be directly pumped by laser diodes, thus resulting in a more compact and efficient laser technology. Moreover, thin-disk and slab Yb-doped lasers can provide output power of the order of few kW (at high repetition rates), which are not obtainable by Cr-doped laser (Koechner, 2006).

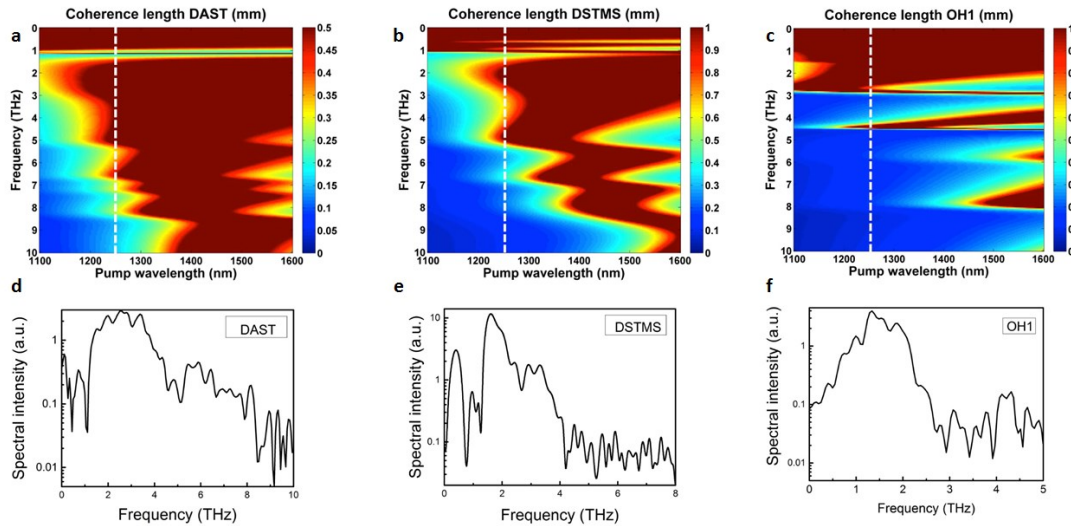


Figure 1.5 Coherence length and THz spectra of organic crystals

Calculated coherence length for (a) DAST, (b) DSTMS and (c) OH1 at different pump wavelengths and THz frequencies. The dashed white line corresponds to the CrF emission wavelength at 1250 nm. (d, e, f) THz frequency spectra obtained by pumping the three organic crystals with the CrF laser. Adapted from (Vicario et al., 2015).

Recently, the new HMQ-TMS organic crystal has been introduced for THz applications (Brunner et al., 2014; J.-H. Jeong et al., 2013; Lu et al., 2015; Vicario et al., 2015). Compared to other organic nonlinear optical crystals, HMQ-TMS possesses a larger OR phase-matching band, thus it can also be pumped at the emitting wavelengths of common laser amplifiers (e.g. 800 nm and 1030 nm), yet keeping a high conversion efficiency. Furthermore, the optimal molecular packing structure of this crystal maximizes its electro-optic response (since the second order nonlinear susceptibility is proportional to the molecular density of the crystal), which is comparable to the state-of the-art organic crystals (such as OH1, DAST, and HMQ-T (J.-H. Jeong et al., 2013)). Moreover, HMQ-TMS shows better environmental stability and many advantageous crystal characteristics, providing the possibility of an easy control of the crystal thickness and aperture size (J.-H. Jeong et al., 2013). As it will be discussed in Chapter 2, ultrafast Yb-lasers can be effectively used to pump an HMQ-TMS organic crystal to generate few-cycle high-peak-electric-field THz pulses in a simple collinear scheme, an advantageous geometry for practical implementations.

1.2.3 Electro-optical sampling detection

Electro-optical sampling (EOS) is a coherent detection technique that relies on the *Pockels effect* in electro-optic materials, where an applied DC (or low-frequency) field can change the refractive index at visible/near-IR frequencies. EOS is commonly used to retrieve the time trace of the THz electric field. In fact, optical pulses can probe instantaneously the variation of the refractive index induced by the THz electric field in the crystal, since they are much shorter in time than the THz pulse (Figure 1.6a). Thus, the THz electric field can be mapped out by delaying the arrival of the optical probe on the crystal with respect to the THz pulse, averaging over many pulses for each time point.

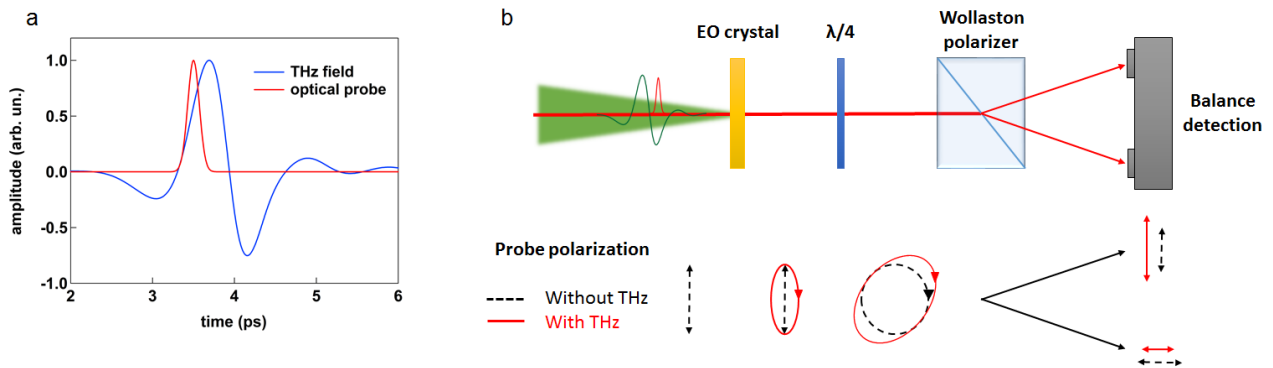


Figure 1.6 Electro-optical sampling

(a) Temporal profiles of a THz electric field (blue) and a Gaussian optical probe pulse intensity envelope with a duration ~ 100 fs (Keathley et al.). (b) Schematic of the EOS measurement and the respective probe polarization after each optical component.

In particular, the probe pulse experiences a birefringence (i.e. a refractive index that depends on the polarization and propagation direction of light) in the crystal induced by the THz electric field, which can be directly measured in terms of *optical phase retardation* between the two orthogonal polarization components of the probe propagating into the crystal. For instance, the phase retardation in a (110)-cut ZnTe crystal of thickness d can be expressed as:

$$\Delta\phi = \frac{\omega n^3 r_{41} E_{\text{THz}} d}{c} \quad (1.9)$$

where n and r_{41} are the refractive index and the relevant electro-optic coefficient of the crystal at the probe frequency ω . The schematic of an EOS measurement is shown in Figure 1.6b. The THz beam and the optical probe are spatially overlapped onto the EO crystal. The induced birefringence is measured by a balanced detection system. The probe pulse that passes through the quarter waveplate is elliptically polarized due to the phase retardation induced by the THz electric field. Thus,

the vertical and horizontal linear components of the polarization are separated in a Wollaston prism and finally detected by two balanced photodiodes. The intensities of the two signals are:

$$\begin{aligned} I_1 &= \frac{I_0}{2}(1 - \sin(\Delta\phi)) \\ I_2 &= \frac{I_0}{2}(1 + \sin(\Delta\phi)) \end{aligned} \quad (1.10)$$

where I_0 is the intensity of the optical probe. For a sufficiently low THz electric field $\Delta\phi \ll 1$, so that the intensity modulation becomes directly proportional to the THz electric field amplitude:

$$\frac{\Delta I}{I_0} = \frac{I_1 - I_2}{I_0} = \lim_{\Delta\phi \rightarrow 0} \sin\left(\frac{\omega n^3 E_{\text{THz}} r_{41} d}{c}\right) = \frac{\omega n^3 E_{\text{THz}} r_{41} d}{c} \quad (1.11)$$

Instead, for high values of the incident THz electric field on the detection crystal, the phase delay between the two polarization components might become larger than $\pi/2$ (i.e., *over-rotation effect*), thus leading to the modulation of the THz waveform peak and to an incorrect estimation of the THz electric field value (Fletcher, 2002). The detection bandwidth of EOS is determined by the phase matching condition between the THz and the optical probe in the detection crystal, the temporal duration of the probe, and possible absorptions of the crystal in the THz range (e.g. phonon absorptions). To increase the signal-to-noise ratio of the measurement, a lock-in amplifier is used to selectively amplify the acquired probe signal modulated at a given reference frequency. This modulation is usually achieved by mechanically modulating the THz signal through a chopper wheel.

As mentioned before, EOS allows to coherently resolve the time-dependent THz waveform, providing both the amplitude and the phase information of the electric field. This detection technique is usually implemented in a THz-TDS measurement, enabling to retrieve both the refractive index, $n(\omega)$, and absorption coefficient, $\alpha(\omega)$, of the sample, without referring to the Kramers-Kronig relations (Dressel & Gruner, 2003), as it will be discussed in section 1.2.5.

1.2.4 Two-color plasma THz source and air-biased-coherent-detection

As it has already been mentioned before, THz spectroscopy is an extremely appealing tool for the identification and the characterization of materials, since several excitations in condensed matter are resonant at THz frequencies (e.g. vibrational modes, superconductive gaps, phonons, magnons, etc.) (Dexheimer, 2007). For this purpose, the use of a broadband THz source that could cover the entire THz frequency range would be ideally required. Photoionization of air using ultrashort laser pulses provides a viable solution for the table-top generation of high-field and broadband THz pulses. In the first demonstration of the laser-plasma-based generation of THz pulses (Hamster et al., 1993), laser pulses with energy of few tens of μJ were focused in air. In particular, the ponderomotive force present at the focus of intense laser pulse generates a large density separation between the ionic and electronic charges, which results in the generation of an electromagnetic transient. A few years later, Cook and Hochstrasser demonstrated the enhancement of THz emission via a two-color laser-filamentation (Cook & Hochstrasser, 2000). A schematic picture of this method is shown in Figure 1.7a.

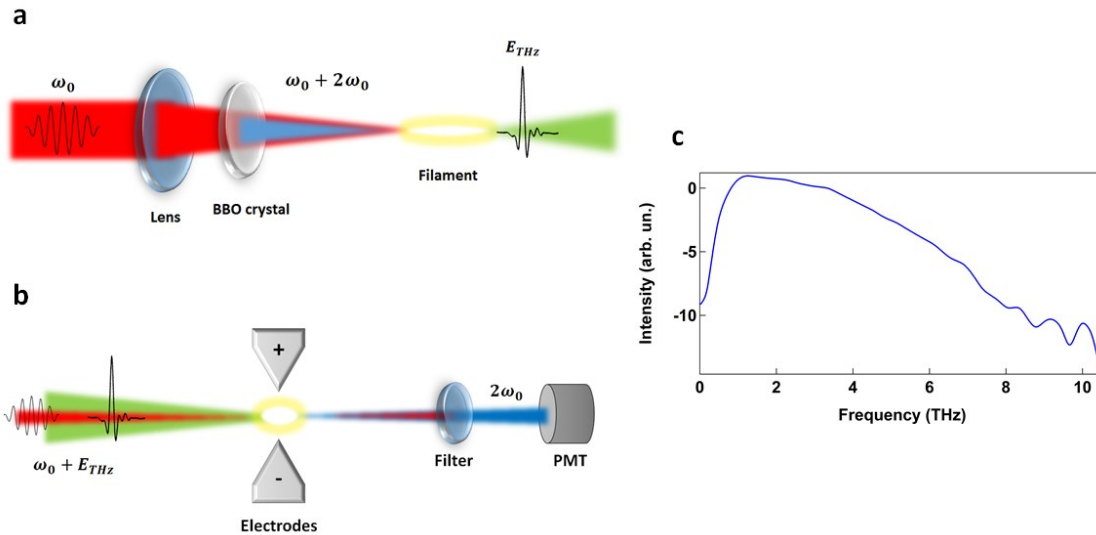


Figure 1.7 two-color-plasma-based THz source and ABCD detection schemes

(a) Schematic of a two-color-plasma-based THz source and (b) of the ABCD technique. (c) THz spectrum generated via 2 color plasma and detected through the ABCD technique. Adapted from (Tomasino et al., 2013)

A femtosecond laser pulse (ω_0) passes through a frequency doubling crystal such as beta barium borate (BBO), which generates a second harmonic pulse ($2\omega_0$). In this collinear scheme, the BBO crystal is often detuned from its optimal angle (i.e. when the ω_0 -polarization is parallel to the ordinary axis of the crystal) in such a way that the ω_0 -field component is parallel to $2\omega_0$, which is polarized along the extraordinary axis (Oh et al., 2012). Subsequently, the two beams are focused

together in air, thus achieving the ionization of gas molecules and the consequent THz emission. The mechanism at the origin of the THz radiation from two-color plasma has been firstly described as a four-wave mixing process, since ionized air can be considered as a 3rd order nonlinear medium. However, the third order nonlinearity originating from both bound electrons of ions and free electrons is too small to explain the observed THz field strength. Later, (Kim et al., 2007) proposed a semiclassical model to explain the process, where the THz generation is determined by the time variation of the electron photocurrent. In this picture, a nonvanishing electron current can arise during optical field ionization of air due to the asymmetric laser field, resulting in the emission of terahertz electromagnetic pulses. The advantage of using plasma for THz generation relies on the fact that, unlike bulk nonlinear crystals, gases do not suffer from damage thresholds and are continuously renewable, thus they can be pumped at extremely high intensities. Moreover, due to the very low dispersion of gases, their use as THz emitter and detector allows the generated THz bandwidth to be practically limited only by the laser pulse duration. The use of laser pulses with energies greater than 100 μJ and durations shorter than 100 fs makes possible to effectively generate broadband THz radiation via two-color plasma. More recently, further improvements to the two-color plasma THz source have been investigated. For instance, in (Blanchard et al., 2009) the problem related to the intensity dependent spatial drift of plasma has been overcome by substituting the focusing lens with a gold-coated off-axis parabolic mirror. This simple solution resulted in a >2 times increase in THz generation efficiency when compared to the lens configuration case. Moreover, (Clerici et al., 2013) showed theoretically and experimentally that scaling to longer pump wavelengths strongly boosts the down-conversion efficiency in the THz region, since the plasma current rises proportionally with the square of the pump wavelength, finding a scaling of the emitted THz energy that increases with $\lambda^{4.6}$ up to 1.8 μm.

The coherent detection of broadband THz pulses can be obtained through the air-biased-coherent-detection (ABCD) technique, shown in Figure 1.7b. In this process, an intense THz electric field can break the symmetry of a centrosymmetric medium (such as air) and consequently lead to the electric field induced second harmonic (EFISH) of an ultrashort optical probe pulse (Nahata & Heinz, 1998). Thus, it has been shown that the THz field can be coherently detected measuring the SH signal generated in air (via a photomultiplier tube) by applying an external AC electric field, E_{bias} , which biases the interaction between the THz and probe beams. The total intensity of the SH beam is expressed by the following equation (Karpowicz et al., 2008):

$$I_{\text{SH}} \propto (\chi^{(3)} I_{\omega_0})^2 [(E_{\text{THz}})^2 + (E_{\text{bias}})^2 \pm 2E_{\text{THz}}E_{\text{bias}}] \quad (1.12)$$

where $\chi^{(3)}$ is the third-order susceptibility of air, I_{ω_0} the optical probe intensity, and E_{THz} the THz electric field. As it is shown in Equation (1.12), the last, cross term of the equation scales linearly with the THz electric field, and can be acquired by using a lock-in amplifier synchronized to the modulation frequency of the bias voltage. Due to the very low dispersion of air, ABCD allows us to record THz pulses with bandwidths exceeding 10 THz (Figure 1.7c), although it requires kilovolt (kV) bias sources and tens of microjoule (μJ) probe energies.

Moreover, it is possible to estimate the THz electric field amplitude through the EFISH process (Tomasino et al., 2018). In fact, by applying a DC bias field, $E_{\text{bias}}^{\text{DC}}$, and synchronizing the lock-in amplifier to the chopping frequency of the THz beam, only the squared term dependent on the bias field is suppressed in Equation (1.12), resulting in

$$I_{\text{SH}} \propto (E_{\text{THz}})^2 \pm 2E_{\text{THz}}E_{\text{bias}}^{\text{DC}} \quad (1.13)$$

Thus, if we consider two measurements taken with (I_{SH}^B) and without (I_{SH}^0) applying a known static bias voltage ($V_{\text{bias}}^{\text{DC}}$), it is possible to use Equation (1.13) to retrieve the sign and the amplitude of the THz electric field:

$$E_{\text{THz}} = \frac{2E_{\text{bias}}^{\text{DC}}}{\Delta I_{\text{SH}}} = \frac{2V_{\text{bias}}^{\text{DC}}}{d \Delta I_{\text{SH}}} \quad (1.14)$$

where $\Delta I_{\text{SH}} = (I_{\text{SH}}^B - I_{\text{SH}}^0)/I_{\text{SH}}^0$ is the relative change in the EFISH intensity and d is the distance between the two tips where the bias voltage is applied.

In Chapter 2, we will present the generation of high-field and extremely broadband THz pulses (> 60 THz) via two-color laser-filamentation by using Yb laser pulses compressed through an Ar-filled hollow-core fiber. The characterization of these THz pulses has been achieved through the ABCD detection scheme.

1.2.5 THz time-domain spectroscopy and data analysis

THz-TDS is a powerful experimental technique that can be used to characterize the complete THz response of a given system. The standard experimental apparatus for THz-TDS (Figure 1.8) consists of a THz source (emitter) and a coherent detection system (e.g. EOS), which are both based on the use of a femtosecond laser. Since THz frequencies can be significantly absorbed by the water molecules in the atmosphere, usually the THz path is purged with nitrogen gas.

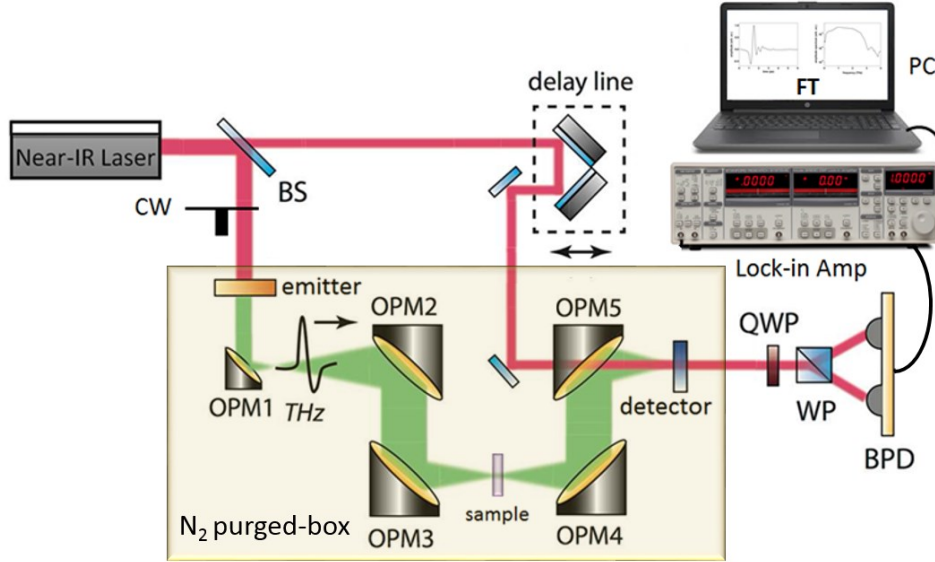


Figure 1.8 Schematic of a THz-TDS setup

BS – beam splitter, CW – chopper wheel, OPM – 90-deg off-axis parabolic mirrors, QWP – quarter wave plate, WP – Wollaston prism, BPD – balanced photodiodes. Detection is performed via EOS. The THz beam propagates into a box purged with nitrogen. A lock-in amplifier is used to improve the signal to noise ratio.

In contrast to the conventional spectroscopy techniques based on the intensity measurement of the signal (e.g. FTIR), THz-TDS allows to acquire directly the THz transient electric field, thus retrieving both the amplitude and phase information of the measured wave. As a consequence, through an appropriate measurement analysis, it is possible to obtain at the same time the dispersive and absorptive properties of the sample under investigation. This procedure is a very important and typical use of a THz-TDS measurement and is reported in what follows for completeness, focusing on the relevant case of a thin film on a transparent substrate. Let us consider the THz signal transmitted by a thin film f with a defined thickness, d_f , on a transparent substrate s , and the one transmitted only by the substrate as a reference, as shown in Figure 1.9a. The two measured THz signals are subsequently Fourier transformed to obtain the spectral information, $E(v) = A(v)e^{i\phi(v)}$ where $\phi(v)$ and $A(v)$ are the phase and the amplitude of the transmitted signal, respectively (Figure 1.9b,c). For

discretized experimental data, the Fourier transformation is replaced by a *discrete Fourier transformation* (DFT, or FFT if the *fast Fourier transform* algorithm is used).

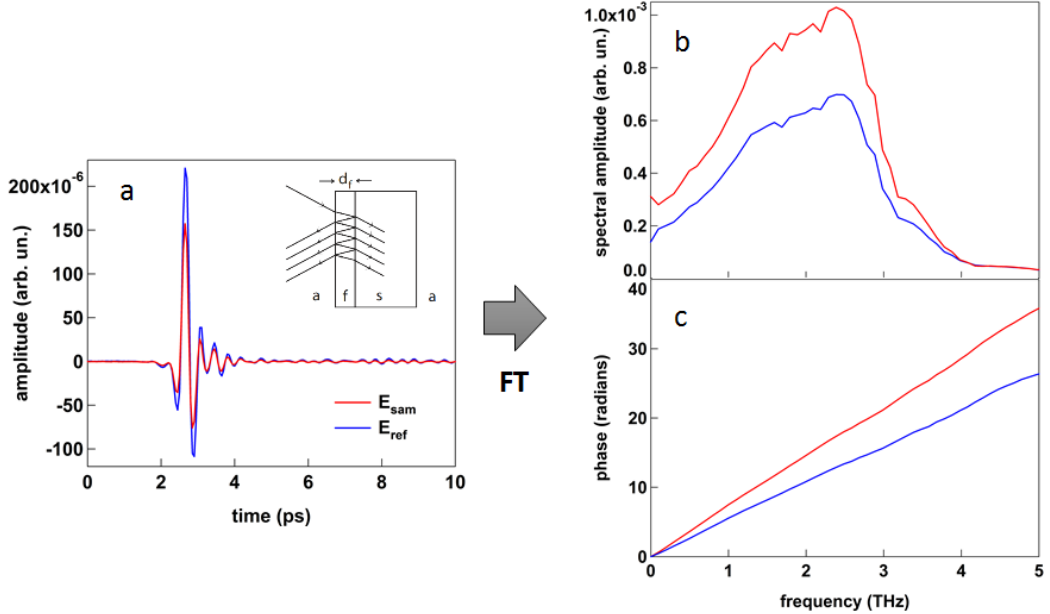


Figure 1.9 Analysis of a THz-TDS measurement

(a) THz waveforms transmitted by the sample (Keathley et al.) and the reference (blue). By applying the FFT it is possible to get (b) the amplitudes and (c) the phases of the two transmitted signals.

The complex refractive index of the film $\tilde{n} = n + ik$ can be calculated from the ratio of the complex transfer functions of the sample and reference (i.e. the substrate), $E_{\text{sam}}(\nu)$, and $E_{\text{ref}}(\nu)$, respectively (Hecht, 2014). The transfer function for the sample is given by:

$$E_{\text{sam}} = E_0 t_{\text{af}} P_f t_{\text{fs}} P_s t_{\text{sa}} F P_{\text{afs}} F P_{\text{fsa}} \quad (1.15)$$

where E_0 is the amplitude of the incident electric field. The complex transmission and reflection Fresnel coefficients, t_{jk} and r_{jk} , are

$$t_{jk} = \frac{2n_j}{n_j + n_k} \quad r_{jk} = \frac{n_j - n_k}{n_j + n_k} \quad (1.16)$$

The propagation through layer j is

$$P_j = e^{-ik_0 d_j n_j} \quad (1.17)$$

where $k_0 = 2\pi\nu/c$ is the wave vector in vacuum. The Fabry-Pérot etalon due to the partial reflections of pulses is given by

$$FP_{jkl} = \sum_{m=0}^M (r_{kl}P_k r_{jk}P_k)^m \quad (1.18)$$

where M is the number of internal reflections measured and depends on the time separation between the reflections as well as the length of the THz-TDS signal time trace. The transfer function of the reference is given by

$$E_{\text{ref}} = E_0 t_{\text{as}} P_s t_{\text{sa}} P_a F P_{\text{asa}} \quad (1.19)$$

So, dividing Equation (1.15) by Equation (1.19), we get

$$\frac{E_{\text{sam}}}{E_{\text{ref}}} = \frac{E_0 t_{\text{af}} P_f t_{\text{fs}} P_s t_{\text{sa}} F P_{\text{afs}} F P_{\text{fsa}}}{E_0 t_{\text{as}} P_s t_{\text{sa}} P_a F P_{\text{asa}}} = \frac{t_{\text{af}} t_{\text{fs}}}{t_{\text{as}}} \frac{P_f}{P_a} \frac{F P_{\text{afs}} F P_{\text{fsa}}}{F P_{\text{asa}}} \quad (1.20)$$

The last equation relates the two experimentally measured THz fields to the unknown refractive index of the film \tilde{n} , and can be solved numerically, knowing the thickness and the refractive index of the substrate. Equation (1.18) can be further simplified for the common case of a thin film on a thick substrate. In fact, for a substrate of high resistivity silicon wafer with a thickness $d_{\text{sub}} = 500 \mu\text{m}$ and a refractive index $n = 3.42$, the first reflection of the THz pulse arrives with a time delay with respect to the transmitted signal given by $\Delta t = 2nd_{\text{sub}}/c \approx 11 \text{ ps}$. Thus, cutting the measurement just before the first internal reflection in the substrate, it is possible to simplify the Fabry-Pérot etalon terms to $F P_{\text{fsa}} = F P_{\text{asa}} = 1$. Furthermore, if the film is so thin that all internal reflections can be considered included in the measurement, Equation (1.18) describing the Fabry-Pérot reflections becomes an infinite sum and simplifies to:

$$FP_{jkl} = \sum_{m=0}^{M=\infty} (r_{kl}P_k r_{jk}P_k)^m = \frac{1}{1 + r_{jk}r_{kl}P_k^2} \quad (1.21)$$

Finally, Equation (1.20) becomes:

$$\frac{E_{\text{sam}}}{E_{\text{ref}}} = |A(\nu)| e^{i\Phi(\nu)} = \frac{t_{\text{af}} t_{\text{fs}}}{t_{\text{as}}} \frac{P_f}{P_a} \frac{1}{1 + r_{\text{af}} r_{\text{fs}} P_f^2} \quad (1.22)$$

Thus, it is possible to solve numerically the last complex equation to retrieve the real and imaginary part of the refractive index of the film.

1.3 Optical nanoantennas

At the end of 1959, in his famous lecture “*There’s Plenty of Room at the Bottom*”, Richard Feynman envisioned the promising opportunities offered by the progresses in the fabrication of nano-size structures. After 60 years, many of the conjectures proposed by Feynman have been realized and nowadays *nanotechnology* is an established reality with a profound impact both in scientific research and industry.

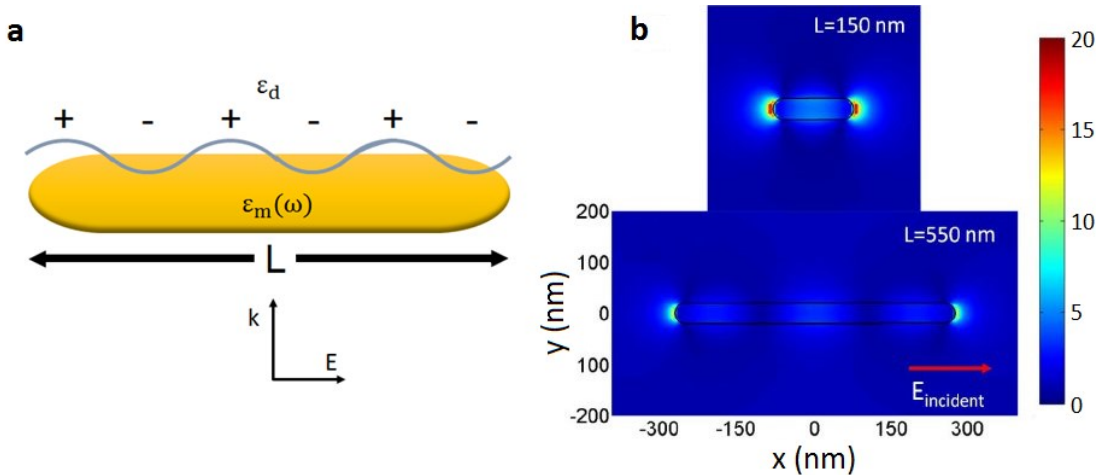


Figure 1.10 Optical plasmonic nanoantennas

(a) When a polarized plane wave illuminates a rod nanoantenna, the oscillating electric field gives rise to a standing surface charge wave. (b) Electric field amplitude distribution for an incident wavelength of $\lambda = 830$ nm and antenna lengths of $L = \lambda_{\text{eff}} / 2$ and $L = 3 \lambda_{\text{eff}} / 2$. Adapted with permission from (Cubukcu et al., 2008) © 2008 IEEE.

In the last decades, the enormous advances of nanofabrication techniques have paved the way to the development of *nano-optics*, an interdisciplinary field of research concerning the study of nano-scale optical elements, such as *optical nanoantennas* (NAs) (Agio & Alù, 2013) and their interaction with light. Similarly to their radio wave and microwave counterparts, optical NAs are devices able to harvest propagating electromagnetic waves and convert them in confined energy, and vice versa, allowing the manipulation and the control of light beyond the diffraction limit. This is made possible by the excitation of surface (*plasmonic*) modes at the interface between the conductive surface of the NAs and the dielectric surrounding environment (Maier, 2007), as shown in Figure 1.10a. The confinement of the electromagnetic energy in subwavelength volumes leads to the local enhancement of the electric/magnetic fields, which can be used to intensify light-matter interaction at the nanoscale. Thus, optical NAs have been extensively employed in several applications, such as enhanced nonlinear phenomena (Kauranen & Zayats, 2012), sensing of electrochemical processes (Hoener et al., 2018), and single-molecule imaging (Taminiau et al., 2007). Moreover, such localized high fields have been exploited in spectroscopy techniques for the associated capability of increasing the sensitivity of traditional spectroscopies, such as in *surface enhanced Raman spectroscopy* (SERS)

(Pilot et al., 2019) and in *surface enhanced infrared absorption* (SEIRA) (Neubrech et al., 2017), as well as in near-field imaging, enabling the direct investigation of systems at sub-wavelength scale through *scanning near-field optical microscopy* (SNOM) (Bazylewski et al., 2017).

The resonance frequency of the optical NA is mainly determined by its geometrical dimensions, which need to be tuned with the wavelength of the incoming radiation, λ . For instance, at microwave wavelengths, a metallic rod of length $L = \lambda/2$ acts as an ideal half-wave dipole resonator. However, scaling towards higher frequencies (i.e. IR/vis/UV) and smaller antenna sections (down to the nanoscale), the radiation can partially penetrate into the NA, giving rise to oscillations of the free-electron gas. The finite effective mass of the free carriers introduces a phase delay with respect to the oscillations of the electromagnetic radiation. When this phase delay is equal to $\pi/2$, the amplitude of the charge oscillation reaches a maximum and is only limited by the internal (ohmic and radiative) losses of the system (Biagioni et al., 2012). For metallic nanostructures, this condition corresponds to the NA resonance, which can be tuned in frequency by scaling the NA's size. Thus, at optical frequencies an antenna responds to a shorter effective wavelength λ_{eff} which is related to the incident wavelength, λ , through the following empirical relation (Novotny, 2007):

$$\lambda_{\text{eff}} = n_1 + n_2[\lambda/\lambda_p] \quad (1.23)$$

Where λ_p is the plasma wavelength of the metal, and n_1 and n_2 are constants depending on the geometrical and dielectric properties of the antenna. According to this wavelength scaling rule, an optical half-wave antenna has thus a shorter length of $\lambda_{\text{eff}}/2$ (Figure 1.10b) with respect to the free-space wavelength, if compared to a radiofrequency antenna. In general, the nanoantenna resonance quality factor, Q , can be estimated as $Q = \omega_{\text{res}}/\Gamma$, where ω_{res} is the resonance central frequency, and Γ the resonance spectral bandwidth, which accounts for both the radiative and non-radiative losses (Ismail et al., 2016). The resonance quality factor can be improved by properly choosing the material and the shape of the optical NA. Conventionally, optical NAs are made of metallic materials (e.g. gold, silver, aluminum), because of their high free carrier concentration. However, at optical frequencies metals present also significant losses which strongly affect Q . Other kinds of conductive materials have also been investigated in different frequency regions, such as highly-doped semiconductors (Law et al., 2013) and transparent conductive oxides (e.g. ITO, AZO) (Abb et al., 2013).

1.3.1 Strategies to improve the resonance quality factor: surface lattice modes and out-of-plane configuration

In principle, the NA Q -factor can be significantly improved when multiple nanostructures are arranged in periodic arrays (Kravets et al., 2018). Indeed, by appropriately choosing the array period as well as the right combination of size and shape of the NAs, it is possible to obtain a constructive interference between the local electric field acting on each NA and the scattered fields from the surrounding nanostructures of the array. When extended over a large array of NAs, these scattered fields can act in phase significantly increasing the effective NA quality factor, with a narrowing of the resonance width accompanied by a significant enhancement of the local electric field at the NA hotspot.

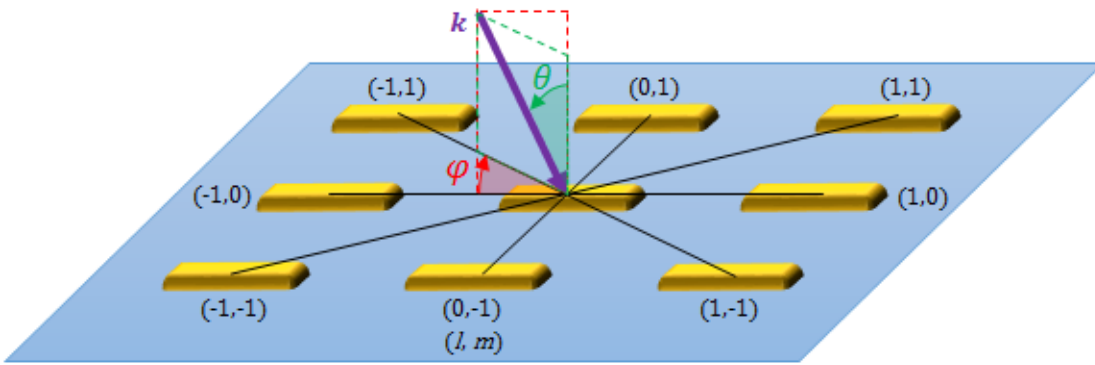


Figure 1.11 Sketch highlighting the primary lattice modes

This “cooperative” effect can be explained in terms of a Fano-coupling between the broad NA resonance and the so-called *surface lattice mode* (also known as *diffraction mode* or *Wood-Rayleigh anomaly*) of the periodic array. This surface lattice mode corresponds to the appearance of diffracted orders in a periodic system and is associated with a wave propagating in the plane of the array (Rayleigh, 1907). Let’s consider the wavenumber of a lattice resonance in a rectangular lattice cell of a periodic structure:

$$k_{\text{lat}} = |\mathbf{k} + \mathbf{G}| \quad (1.24)$$

In this equation, $\mathbf{k} = \hat{\mathbf{e}}_x k_x + \hat{\mathbf{e}}_y k_y$ is the wavevector of the incident electromagnetic wave on the x-y plane, where $\hat{\mathbf{e}}_{x,y}$ and $k_{x,y}$ are respectively the unit vector and the wavenumber along the x or y-axis, $\mathbf{G} = lG_x \hat{\mathbf{e}}_x + mG_y \hat{\mathbf{e}}_y$ is the reciprocal lattice vector, given by the combination (weighted by the mode orders l, m) of $G_{x,y} = \frac{2\pi}{g_{x,y}}$, where $g_{x,y}$ is the geometrical spacing among the nanostructures in the x-y directions, respectively. The wavenumber of a lattice resonance can be generally written as $k_{\text{lat}} = n \cdot$

k_0 , where k_0 is the wavenumber in free space and n is the refractive index of the considered medium. It is possible to decompose the wavevector \mathbf{k} considering its polar (θ) and azimuthal (φ) angles (Figure 1.11). Thus the x and y components of the impinging wavevector can be written as:

$$\begin{aligned} k_x &= k_0 \sin \theta \cos \varphi = A \cdot k_0 \\ k_y &= k_0 \sin \theta \sin \varphi = B \cdot k_0 \end{aligned} \quad (1.25)$$

where $A = \sin \theta \cos \varphi$ and $B = \sin \theta \sin \varphi$. Substituting these two identities in Equation (1.24), we obtain:

$$n^2 k_0^2 = (A k_0 + l G_x)^2 + (B k_0 + m G_y)^2 \quad (1.26)$$

Finally, solving the quadratic Equation (1.26) for k_0 , and keeping only the physical solution, we obtain:

$$k_0 = \frac{2(AlG_x + BmG_y) + \sqrt{4(AlG_x + BmG_y)^2 + 4(n^2 - A^2 - B^2)(l^2 G_x^2 + m^2 G_y^2)}}{2(n^2 - A^2 - B^2)} \quad (1.27)$$

Thus, the corresponding wavelength and frequency of the lattice mode are $\lambda_0 = \frac{2\pi}{k_0}$ and $\nu_0 = \frac{ck_0}{2\pi}$.

Therefore, the resonance position of the lattice mode depends on the periodicity of the array, on the angle of incidence of the input light and on the surrounding dielectric properties. Fixing the incident angle and the refractive index, the lattice mode with the lowest frequency will be determined by the array spacing and the combination of (l, m) . Indeed, as it is possible to see from Equation (1.27), if $g_x > g_y$ the first lattice mode in frequency is given by $l = -1$ and $m = 0$. Symmetrically, if $g_y > g_x$ the first lattice mode in frequency corresponds to $l = 0$ and $m = -1$. In particular, for the case of a square array (i.e. $g_x = g_y$) both combinations $(l = -1, m = 0)$ and $(l = 0, m = -1)$ give the solutions corresponding to the lowest lattice mode frequency. Equation (1.27) will be applied to the case of the squared arrays of RNCs described in Chapter 3.

At the same time, an out-of-plane configuration can reduce the contact area between the structure and the substrate by a factor proportional to the aspect ratio of the NA (i.e. the ratio between the long and the short axis of the NA), which can be advantageous for certain application, as we will see in Chapter 3. Moreover, this geometrical configuration can be further exploited to reshape the NA resonant behavior. In fact, the presence of a metallic layer (mirror-image plane) between the vertical antenna and the dielectric substrate allows to virtually double the length of the antenna. This can be

understood through the concept of the image charges: when charges accumulate at the tip of an antenna with length L , charges of the opposite sign are induced in the metallic substrate, which acts as a reservoir. Therefore, the situation is equivalent to an antenna of length $2L$ with no substrate inserted in a homogenous background. Since the electric potential must coincide in both cases and the incident electric field is the same, it follows that charge density at the tip of the L -long antenna must be twice the density of the $2L$ -long antenna (Figure 1.12).

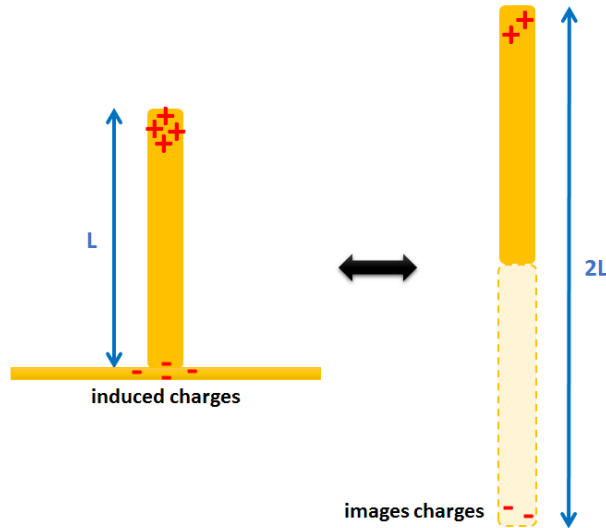


Figure 1.12 Effect on induced charges when the antenna is placed over a metallic substrate

In a recent work (Malerba et al., 2015), it has been demonstrated how the transition from planar to vertical IR resonant structures enables a stronger plasmonic response, leading to higher harvesting capabilities and field enhancements. In particular, the optical response of a silver planar nanorod on a dielectric substrate and of a silver vertical nanocylinder on a metallic substrate (sketch in Figure 1.13a), has been retrieved via numerical simulations. The two nanostructures present a resonance at approximately $\lambda_{\text{res}} = 8.5 \mu\text{m}$ and are illuminated with the same angle of incidence of 45° . As it is shown in Figure 1.13b, the extinction cross section of the vertical nanocylinder is much higher than the one of the planar nanostructure, which is mainly determined by the scattering contribution. Moreover, the near field response of the nanocylinder exhibits a monopole-like modal response (Figure 1.13c), due to the presence of the metallic substrate. This monopole-like mode presents a charge density at the tip-end which is doubled with respect to that of the standard dipole of the planar nanorod, corresponding to a two-fold increase of the electric field enhancement.

Additionally, the intrinsic features of the 3D configuration can lead to a further improvement of the optical response when multiple nanostructures are arranged in a periodic array. In fact, while in the planar configuration the incident light is mainly back reflected by the NAs or transmitted through the

substrate, in the out-of-plane configuration, light is continuously re-scattered along the substrate plane, thanks to the enhanced lateral scattering of the vertical nanostructures, thus promoting a more effective harvesting of collective (lattice-related) effects.

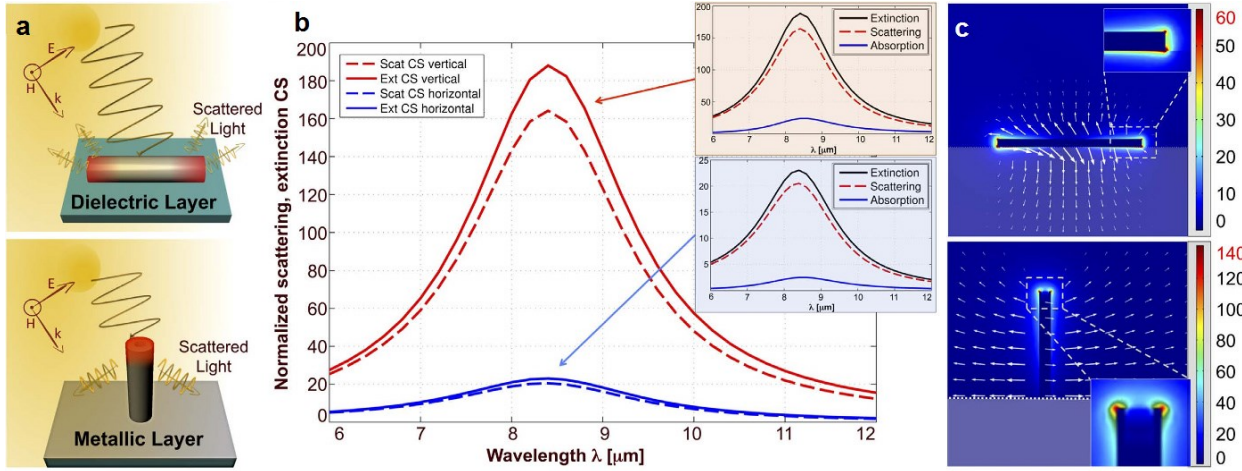


Figure 1.13 Comparison between monopolar and dipolar resonances

(a) Sketch of a planar nanorod on a dielectric substrate and an out-of-plane nanocylinder on a metallic substrate, illuminated by a planar wave with impinging angle of 45° (b) Simulated extinction (solid lines) and scattering (dashed lines) cross sections for the vertical (Keathley et al.) and planar (blue) nanostructures. (c) The near-field response of the planar configuration (top figure) shows a standard dipole mode (colour plot, intensity normalized to the incident field) and the rescattered light is partially directed into the substrate (arrows represent the Poynting vector), whereas the vertical configuration (bottom figure) exhibits a monopolar electric field distribution and a convenient radial energy flow. Adapted from (Malerba et al., 2015).

Indeed, under precise geometrical conditions (i.e. when the distance between the antennas is comparable with $\lambda_{\text{res}}/2$) the scattered fields can lead to a strong constructive coupling between neighbouring 3D NAs, which results in a narrower resonance bandwidth (i.e. a higher resonance quality factor) and a stronger field enhancement. This has been confirmed in the same work, by the measured and simulated far-field response of several arrays of nanocylinders in a reflection configuration, where both the periodicities of the arrays and the heights of the nanocylinders have been tuned to achieve the cooperative effect between the surface lattice mode and the monopole resonance (Figure 1.14a). The corresponding values of the resonance quality factors (retrieved by the relation $Q = \omega_{\text{res}}/\Gamma$) are shown in Figure 1.14b (red circles), highlighted over the values exhibited by non-optimized arrays (light gray background curves). Fairly good experimental quality-factors exceeding values of 20–25 in the whole mid-IR range are clearly visible, with an almost constant trend that opens promising expectations in the far-IR and THz frequency regions. Finally, the quality factor retrieved by the experimental measurement of a single vertical nanocylinder and the numerically calculated values for a single planar nanorod and an optimized array of NAs on a

silicon substrate are shown in Figure 1.14b for direct comparison. The quality factor of surface plasmons in bulk silver is also reported as a reference (dark black line).

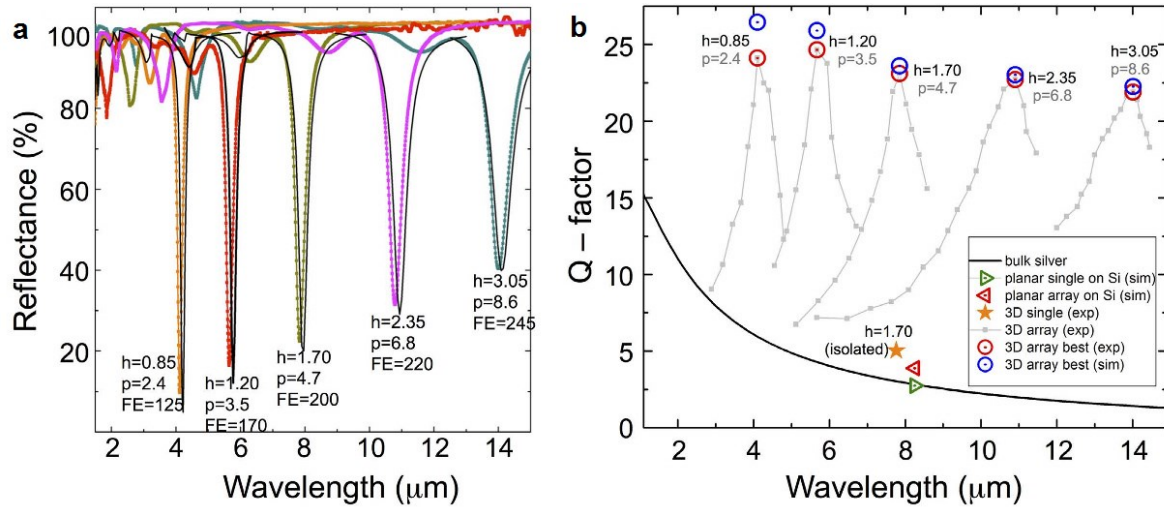


Figure 1.14 Lattice mode characterization

(a) Measured reflectance plots (dotted lines) of arrays of silver nanocylinders with different heights. The corresponding results from numerical simulations are shown (solid curves). The field enhancement factors (FE) are also reported. (b) Q-factors calculated from the experimental curves of panel (a), together with the ones estimated for a single vertical nanocylinder, a single planar nanorod, a 2D array and the value for surface plasmons in bulk silver. Adapted from (Malerba et al., 2015).

In Chapter 3, it will be shown how this cooperative effect arising from the periodic array configuration can be exploited also at THz frequencies, for the case of an array of vertical gold nanocones, presenting a monopole resonance centered at 1 THz. In particular, the large field enhancement obtained through the engineering of the optical response of the array has been used to induce THz field-driven electron emission from the nanocones apex.

In the following paragraphs we will discuss more in detail the properties of arrays of THz resonant NAs, focusing on the ways to improve the response of these nanostructures and on some possible applications at THz frequencies.

1.3.2 Planar arrays of THz dipole nanoantennas

THz spectroscopy is a powerful tool for the characterization of some fundamental properties of matter systems, due to the presence of numerous rotational and vibrational excitations resonating at THz frequencies. However, the study of few molecules or nano-objects is generally limited by the low spatial resolution and sensitivity of such spectroscopy, due to the relatively large scale of THz wavelengths. Optical NAs resonating at THz frequencies offer a viable solution to this problem, since they are able to confine the tens/hundreds-of-microns-long THz wavelengths into nanometer-sized hotspots, leading to an extremely high local field enhancement that can be used to strongly intensify light-matter interaction at THz frequencies.

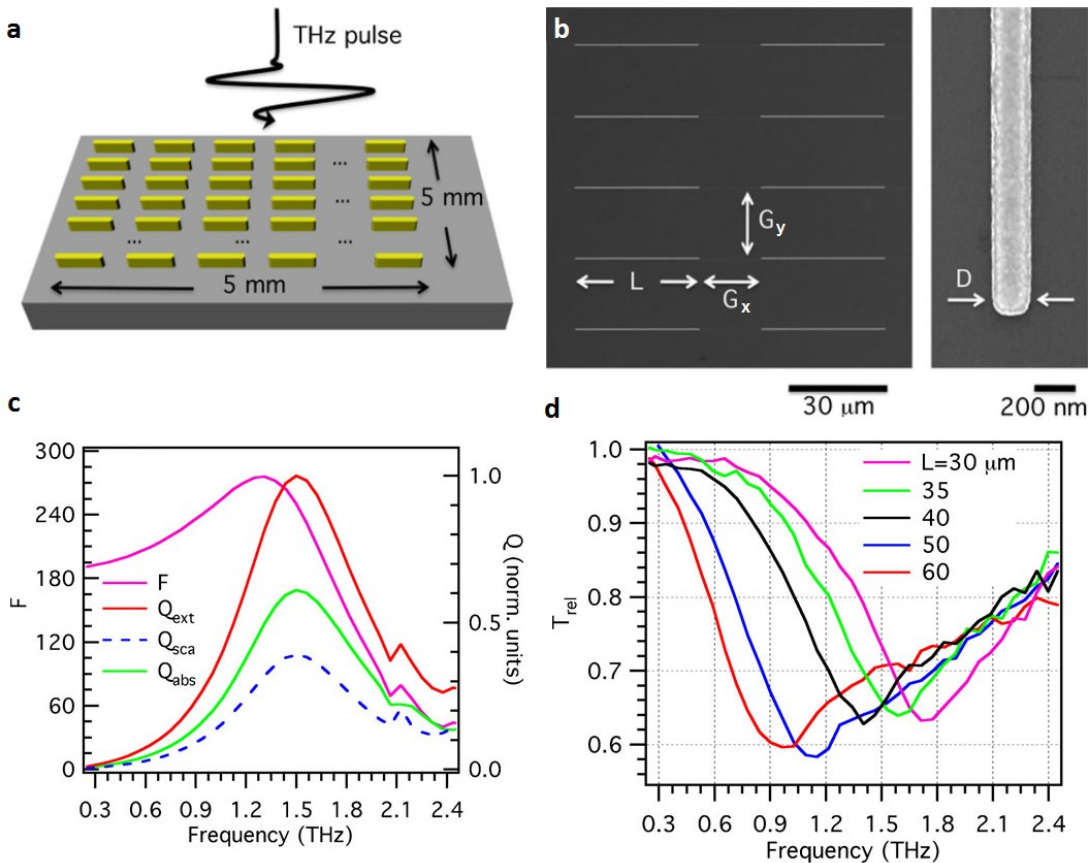


Figure 1.15 Array of THz dipole nanoantennas

(a) Sketch of an array of THz gold NAs on a transparent high-resistivity silicon substrate. (b) SEM images of the fabricated array. L and D represent the length and the width of the NA, respectively, while G_x and G_y are the periodicities of the array. (c) Numerical results of the field enhancement factor calculated nearby the antenna end and the absorption, scattering and extinction cross section as a function of frequency. (d) Transmission curves of the arrays for different antenna lengths. Adapted from (Razzari et al., 2013).

In particular, *arrays of THz dipole NAs* (Razzari et al., 2013) combine a strongly localized field enhancement with a spatially extended interaction with the incoming radiation, which improves far-field detectability (Figure 1.15a) and can thus find important applications as a platform for ultra-

sensitive THz spectroscopy and antenna-enhanced THz nonlinear experiments. Arrays of THz gold NAs are typically fabricated via electron beam lithography on high-resistivity (Krause et al.) silicon substrate ($\geq 10,000 \Omega \cdot \text{cm}$), which provides both negligible loss and chromatic dispersion at THz frequencies (Figure 1.15b). The central wavelength of resonance, λ_{res} , moves with the length of the NA, L , according to the following relation:

$$\lambda_{\text{res}} = 2n_{\text{eff}}(L + 2\delta) \quad (1.28)$$

where n_{eff} is the effective refractive index of the surface charge wave, and δ is introduced to take into account the apparent increase of the antenna length, due to the reactance of the antenna ends, which is of the order of the lateral dimension of the antenna, D , and so can be usually neglected since $L \gg D$. In general, the optical response of the NA is characterized both by its near- and far-field responses. The NA near-field behavior is described by the *field enhancement distribution* (defined as the ratio of the local electric field to the free-space field), whereas the far-field response is related to the extinction efficiency, $Q_{\text{ext}} = \frac{\sigma_{\text{ext}}}{\sigma_{\text{geo}}} = Q_{\text{abs}} + Q_{\text{sca}} = \frac{\sigma_{\text{abs}}}{\sigma_{\text{geo}}} + \frac{\sigma_{\text{sca}}}{\sigma_{\text{geo}}}$, where Q_{abs} and Q_{sca} are the absorption and scattering efficiencies, whereas σ_{ext} , σ_{abs} and σ_{sca} , are the related cross sections, while $\sigma_{\text{geo}} = L \cdot D$ is the geometrical NA area. This information can be fully retrieved by means of numerical electromagnetic simulations, as it is shown for example in Figure 1.15c for an array of dipole NAs with a length of $L = 40 \mu\text{m}$. In this case, both absorption and scattering significantly contribute to the far-field resonance properties of the NAs, showing a broad peak at the same frequency of 1.5 THz. As one can see, the central frequency of the field enhancement peak is instead redshifted of 200 GHz with respect to the far-field peak, which is a consequence of the ohmic damping of the NA response, similarly to what happens to the amplitude response of a damped harmonic oscillator (Zuloaga & Nordlander, 2011). The far-field THz response of the array can be experimentally characterized via far-field extinction spectroscopy by using linearly polarized THz radiation. In fact, when the polarization of the THz light is parallel to the NA long axis, the dipole mode of the antenna is excited, and THz radiation is consequently absorbed and scattered in correspondence of the resonance frequency. Whereas, when the polarization is perpendicular to the long axis, the transmitted THz radiation is negligibly affected by the presence of the NAs. Thus, it is finally possible to obtain the THz transmission response of the array through the ratio between the two acquired transmission spectra. As it is shown in Figure 1.15d, the relative transmission curves measured for different THz arrays of dipole NAs present a broadband resonance dip, which shifts in frequency according to the antenna length.

1.3.3 Localization of THz fields in nanocavities

In order to improve the field localization, nano-gaps between end-to-end-coupled NAs (instead of single antennas) have been explored, which can further squeeze the local field in nano-sized volumes and achieve higher field enhancement factors by reducing the gap width (Figure 1.16a). This solution has been effectively employed to retrieve the spectroscopic properties of an ultra-low amount of nanocompounds in an approach called *nanoantenna enhanced terahertz spectroscopy* (NETS) (Toma et al., 2014). In this work, an array of THz NAs has been covered by a monolayer of CdSe quantum dots (QDs) (Figure 1.16b) and the resonance of the array has been tuned at the same frequency of a phonon resonance of the QDs. The coupling between the NA mode and the QDs phonon mode in the nano-gaps results in a Fano interference which is observable in the far-field transmission of the sample (Figure 1.16c, red curve - see black dashed line for the phonon resonance position). Thus, it has been possible to retrieve the resonance characteristics of the QDs phonon resonance (i.e. the central frequency and the resonance bandwidth) by means of a simple analytical model consisting of two coupled harmonic oscillators.

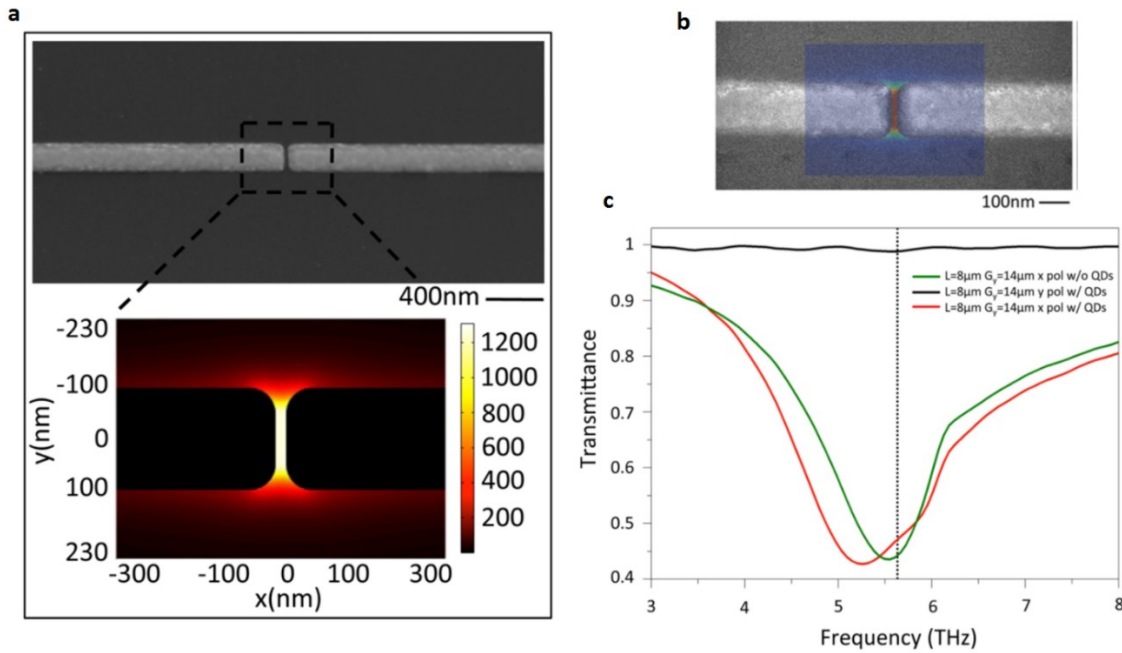


Figure 1.16 Fano coupling in THz nanogaps

(a) SEM detail of a nanogap region (upper panel); field enhancement distribution around the gap region (lower panel). (b) SEM image of a nanocavity covered with QDs. (c) Transmittance of the array with $L = 8 \mu\text{m}$ and $G_y = 14 \mu\text{m}$, for THz polarization set along the nanoantenna long axis and without QDs over the surface (Hafez et al.); transmittance of the same array covered with a QD monolayer, for THz polarization set along the short (Black) and long (Keathley et al.) axis. Adapted with permission from (Toma et al.) © (2014) American Chemical Society.

The confinement efficiency of the nanocavity is related to the *cavity mode volume*, V_{mod} , (i.e., the effective volume occupied by the radiation in the plasmonic nanocavity surroundings), which can be estimated as follows:

$$V_{\text{mod}} = \int \varepsilon(r)|E(r)|^2 dr / \max(\varepsilon(r)|E(r)|^2) \quad (1.29)$$

where ε is the dielectric permittivity and E is the electric field at the point r , the integral being calculated in a volume comprising the whole NA structure (Koenderink, 2010). Thus, through this quantity it is possible to retrieve the THz *vacuum electric field* within the cavity, E_{vac} , which is defined as (Yoshie et al., 2004):

$$|E_{\text{vac}}| = \sqrt{h\nu_{\text{res}}/(2\varepsilon\varepsilon_0 V_{\text{mod}})} \quad (1.30)$$

where h is the Plank constant, ν_{res} is the resonance frequency and ε_0 is the vacuum permittivity. This parameter plays a fundamental role in light-matter coupled systems, since the *coupling strength* scales proportionally with E_{vac} (Yoshie et al., 2004).

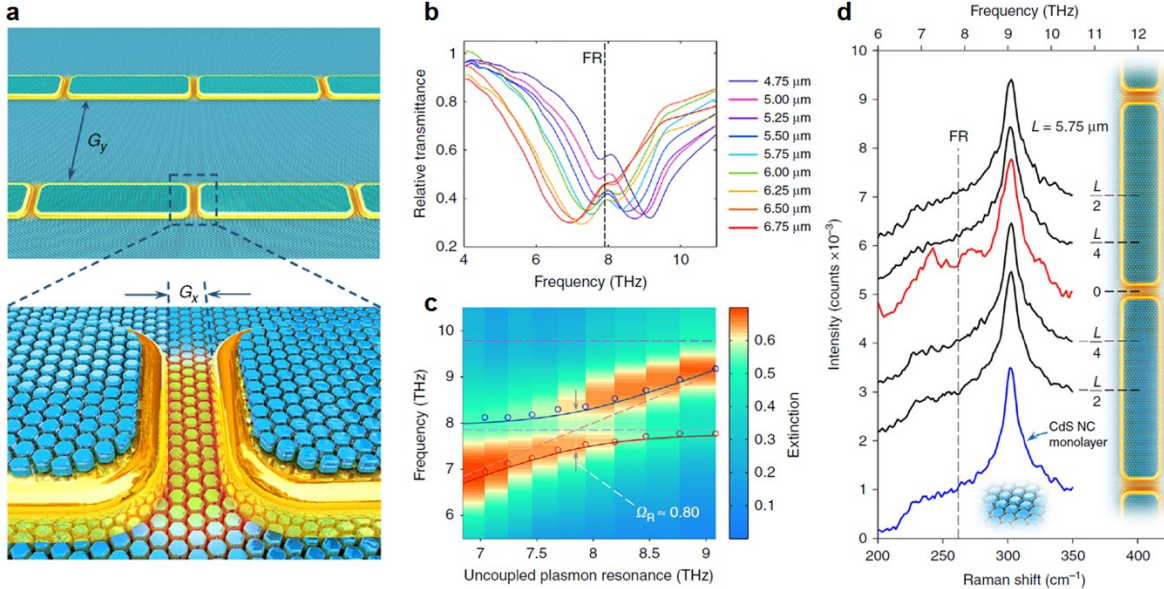


Figure 1.17 Strong coupling in THz nanogaps

(a) Sketch of a plasmonic NA array covered with a monolayer of CdS nanocrystals. (b) Measured transmission of the arrays with different NA lengths, covered with a single layer of nanocrystals. The vertical dashed line refers to the position of the Fröhlich (FR) phonon resonance. (c) Experimental 2D maps of the dispersion of the hybrid system resonance. The colour bar corresponds to the values of the extinction E , retrieved from the transmission T as $E = 1 - T$. The blue (Keathley et al.) solid lines are the trends of the high-energy (low-energy) "polariton" branch, while the purple dashed line defines the lattice mode position of the investigated NA array. (d) Raman spectra of the CdS nanocrystals taken in different positions along the NAs composing a nanocavity (black lines), in the nanogap region (red line) and outside the cavity on the silicon substrate (blue line). The spectra are vertically shifted for clarity. Adapted from (Jin et al., 2018).

As we have shown in a recent work (Jin et al., 2018), THz NAs with extremely small mode volumes can be properly designed to observe the strong coupling regime between the cavity mode of the THz NAs and the optically-active phonon mode (called *Fröhlich* mode (Irmer et al., 2004)) of CdS nanocrystals (Figure 1.17a). Such effect is observable in the far-field THz response of the system through the appearance of two hybridized “polariton” branches (a polariton being a quasiparticle resulting from strong coupling of electromagnetic waves with an electric dipole excitation (Shelton, 2014)) at the sides of the original phonon mode position (Figure 1.17b). This coupling is quantifiable through the “Rabi splitting” between such hybridized resonances (i.e., their separation in frequency when the uncoupled NA resonance is aligned to the uncoupled Fröhlich mode), which has been found to be equal to 0.8 THz for the case presented in Figure 1.17c (1 monolayer of CdS nanocrystals over the NAs). Remarkably, the high THz vacuum electric field confined in an ultra-low cavity mode volume can lead to an effective “reshaping” of the optical phonon energy spectrum of the CdS nanocrystals within the nanocavity, which has been confirmed by the appearance of two peaks also in the Raman response of the nanocrystals (with no THz illumination) collected in correspondence of the nano-gap area (Figure 1.17d).

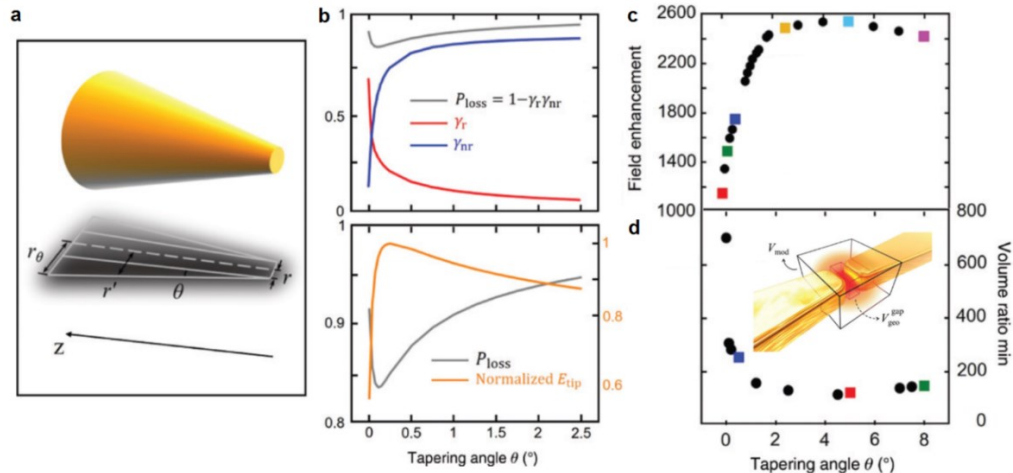


Figure 1.18 Analytical and numerical investigation of THz tapered NAs

(a) Sketch of a conical tapered NA as the one considered in the quasi-analytical model in (Aglieri et al., 2020). (b) Top: key quantities extracted from the analytical model, where γ_r and γ_{nr} are related to the radiative (Keathley et al.) and nonradiative loss (blue) contributions, respectively, while $P_{\text{loss}} = 1 - \gamma_r \gamma_{\text{nr}}$ is the total normalized power loss (dark gray), revealing a minimum for an optimum angle. Bottom: normalized absolute value of the tip field amplitude at the resonance frequency ($f_{\text{res}} = 1.1$ THz) as a function of the tapering angle θ (orange). (c) Numerically evaluated near-field enhancement at resonance as a function of the tapering angle for an NA dimer. (d) Volume ratio ($V_{\text{ratio}} = V_{\text{mod}}/V_{\text{geo}}^{\text{gap}}$) minima (at resonance) as a function of the tapering angle. Inset: sketch of the NA dimer, highlighting the mode volume V_{mod} and the geometrical volume of the gap $V_{\text{geo}}^{\text{gap}}$. Adapted from (Aglieri et al., 2020).

In an effort to further improve the THz field confinement in planar nanocavities, we have also explored new kinds of geometries (Aglieri et al., 2020), to show how properly tapered NA pairs (dimers, in a so-called “bow-tie” configuration) can effectively minimize the nanoresonator loss,

leading to an overall higher field enhancement and a smaller mode volume in the nanocavities. Firstly, the NA has been considered as a conical Fabry-Perot resonator in a quasi-analytical model (Figure 1.18a), to evaluate both the Ohmic effects within the metal (nonradiative loss) and the loss related to the radiation coupling into free space at the antenna extremities (radiative loss). The key quantities for the evaluation of the total loss $P_{\text{loss}} = 1 - \gamma_r \gamma_{\text{nr}}$, are γ_{nr} and γ_r for the non-radiative and radiative effects, respectively, which are defined as:

$$\begin{aligned}\gamma_{\text{nr}} &= e^{-4k_0 \int_0^L \text{Im}\{n_{\text{eff}}(z)\} dz} \\ \gamma_r &= R^2 R_\theta^2\end{aligned}\quad (1.31)$$

Where θ is the tapering angle, $k_0 = \omega/c$ (with ω the angular frequency and c is the speed of light in vacuum), $n_{\text{eff}}(z)$ is the complex effective refractive index of the NA (Tuccio et al., 2014) (z being the coordinate along the antenna length), while R and R_θ are the reflection coefficient at the tip and at the larger extremity, respectively. In this way, it has been possible to highlight a trade-off between a reduced nonradiative loss for large tapering angles and a corresponding increased radiative loss, due to a drop in the reflection coefficient for the surface mode at the enlarged antenna extremity (Figure 1.18b-c).

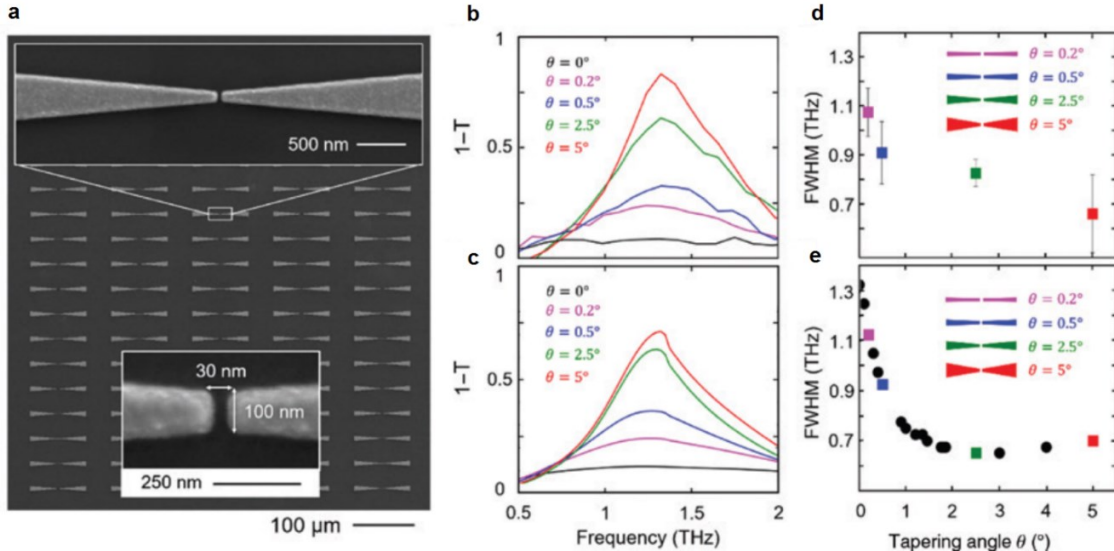


Figure 1.19 Experimental characterization of THz tapered NAs

(a) SEM images of the gold NA dimer array with $\theta = 5^\circ$. The insets show further details of a tapered NA dimer (top) and a zoom of the gap area (bottom). (b, c) Experimental (top) and simulated (bottom) extinction spectra of the fabricated samples obtained through the relation $1-T$, where T is the normalized transmission (the normalization is performed using the transmission of a bare silicon substrate). (d, e) FWHM values of the experimental and simulated spectral responses, respectively. Adapted from (Aglieri et al., 2020).

This behavior has then been confirmed by means of numerical simulations for a planar bow-tie geometry over a HR silicon substrate (gap width 30 nm, while both the NAs are 45-μm-long, 60 nm-

thick and 100 nm wide at the nanogap), with a resonance centered at 1 THz. Both the local field enhancement value at resonance and the ratio of the mode volume to the fixed geometric volume of the nano-gaps ($V_{geo}^{gap} = 30 \times 60 \times 100 \text{ nm}^3$) as a function of θ are reported in Figure 1.18c and 1.18d, respectively. As it is possible to see, the largest enhancements are observed in the region $\theta = 3\text{--}5^\circ$, with values ~ 2.2 times higher than the rod-shaped NA case ($\theta = 0^\circ$), whereas the mode volume decreases drastically for $\theta > 2^\circ$, with v_{ratio} values slightly over 100 times at resonance, approximately a 7-fold reduction with respect to the rod-shaped case.

To experimentally confirm the results of the numerical simulations, five samples of NA dimer arrays with tapering angles $\theta = 0^\circ, 0.2^\circ, 0.5^\circ, 2.5^\circ$, and 5° have been fabricated. The nanostructures have been prepared on top of a HR silicon substrate via electron beam lithography (Figure 1.19a). As expected from the simulations, the dipole resonance of the dimers become observable in the spectral response when the tapering angle is increased, as observable from the THz-TDS characterization of the different arrays (Figure 1.19b). The resonance FWHM has been retrieved for the various arrays, since this parameter is a direct indicator of the total loss (radiative and nonradiative) of a resonator. As it is possible to see in Figure 1.19d, an evident decrease of FWHM is observed in the experimental spectra for the tapered NA dimer arrays, thus confirming the decrease of the total loss. Finally, the corresponding simulated spectral responses and related FWHM values (Figure 1.19c and 1.19e) are shown to be in agreement with the experimental results.

1.3.4 Use of THz resonant nanoantennas for localized nonlinear processes

In the last years, the interest regarding nonlinear phenomena prompted by high-field THz pulses has considerably increased, also thanks to the development of intense, ultrafast THz sources (Hafez et al., 2016). For instance, few-cycle, high-field THz pulses have been employed so far in: ultrafast nonlinear THz spectroscopy of condensed matter via two-color pump-probe schemes (Hwang et al., 2013), nonlinear THz optics (Chai et al., 2018), resonant and non-resonant control of material degrees of freedom (Kampfrath et al., 2013), and the control of the nonlinear response of metamaterials (Fan et al., 2013). However, most of such nonlinear applications require THz field strengths of the order of tens of MV/cm, which is still challenging to generate in free space from table-top laser systems. Such high field strengths can be achieved by means of the large field enhancement offered by THz plasmonic resonators in combination with the high-field THz pulses generated by intense table-top THz sources (e.g. optical rectification in LiNbO₃).

In this paragraph, we will report different examples of nonlinear and strong-field phenomena observed by using THz resonant antennas. For instance, ultrafast *impact ionization* (i.e., a charge carrier accelerated by a strong electric field in a semiconductor can induce the creation of other charge carriers through the impact with neighbours atoms) in a HR silicon substrate has been demonstrated by means of high field THz pulses (up to 251 kV/cm) locally enhanced at the extremities of THz gold antennas arranged in a periodic array (Tarekegne et al., 2015). The linear far-field response of the array shows a broad resonance centered at 0.6 THz. The nonlinear effect has been indirectly observed by measuring the transmission spectrum of the array as a function of the incident THz electric field. In fact, for THz peak field strengths higher than the local threshold for impact ionization in HR silicon (estimated to be 570 kV/cm), the effective refractive index of the substrate in proximity of the antenna ends increases, due to multiplication of the local carrier density, which finally results in the redshift of the resonance frequency (Figure 1.20a). In a similar study, nonlinear THz absorption has been observed in an intrinsic GaAs wafer patterned with nanometer-width slot antenna array (Y.-G. Jeong et al., 2013). In particular, the near-field THz strength reaches a maximum value of 20 MV/cm (due to the field enhancement factor of ~50 in the plasmonic nanostructure), which is strong enough to induce the generation of free carriers ($> 10^{17} \text{ cm}^{-3}$) in the conductive band of GaAs through inter-band transitions associated with impact ionization, observable through a notable 35% increase of the THz absorption (Figure 1.20b). Additionally, it has been shown that THz field-driven carrier generation in an undoped GaAs substrate can lead to bright visible electroluminescence in the proximity of the hotspot of the metamaterial, as it has been observed by (Lange et al., 2014) (Figure 1.20c).

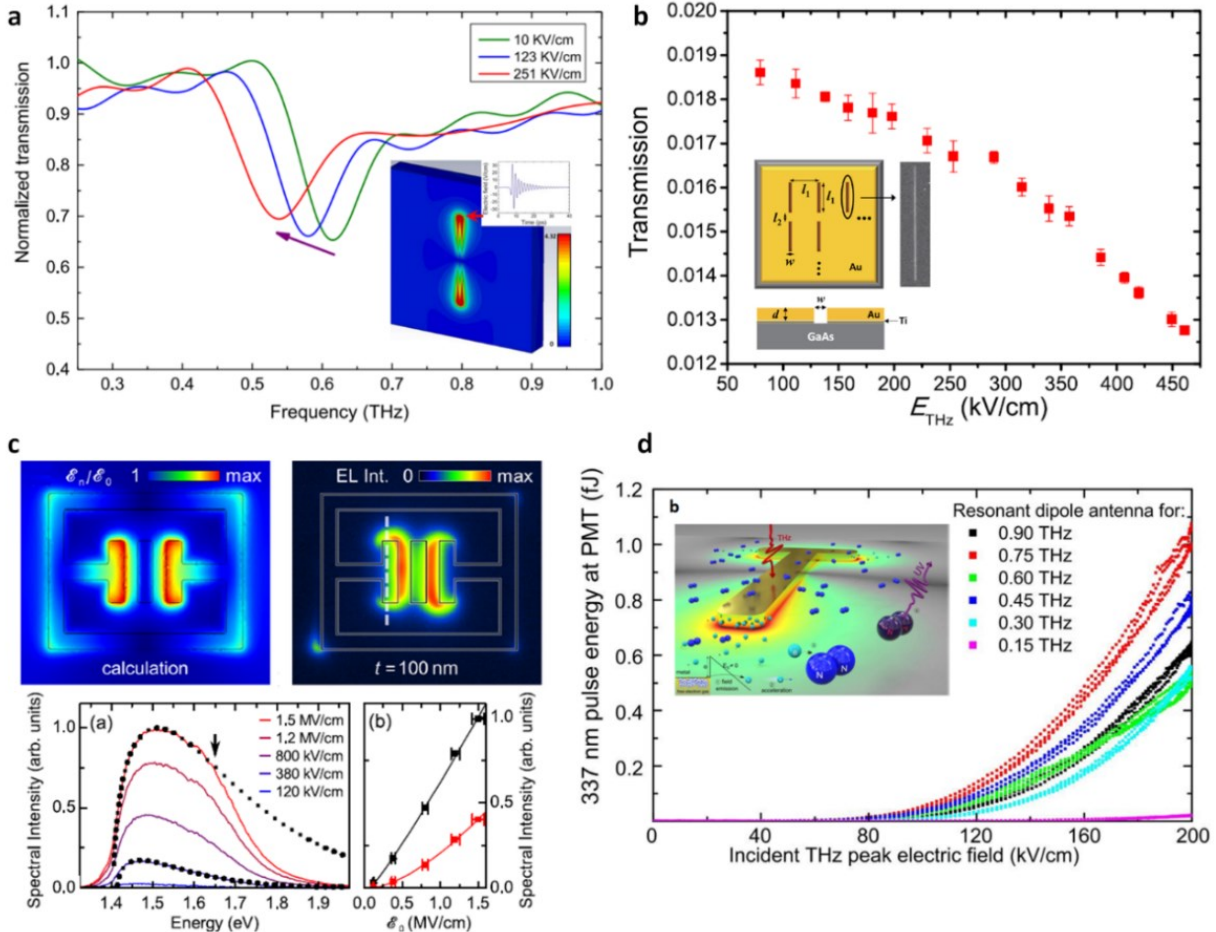


Figure 1.20 Nonlinear experiments with THz NAs

(a) Redshift of the antenna resonance frequency for high incident THz peak fields, due to impact ionization in the HR-Si substrate. The inset shows THz near field distribution for a single antenna at the resonance frequency. Adapted from (Tarekegne et al., 2015) © 2015 IOP Publishing Ltd. **(b)** Spectrally integrated transmission of patterned THz resonant gold nanoslots on a GaAs substrate as a function of the incident THz field. The sketch of the sample is reported in the inset. Adapted with permission from (Y.-G. Jeong et al.) © 2013 AIP Publishing. **(c)** The enhanced THz near-field in correspondence of the resonance of the metamatteal can induce the formation of a hot electron-hole plasma in the GaAs substrate, which leads to a visible electroluminescence. Adapted with permission from (Lange et al.) © 2014 American Physical Society. **(d)** Fluorescence emission as a function of the incident THz peak electric field for dipolar antennas with various resonant frequencies. The process of THz driven electron tunneling and consequent excitation of the nitrogen molecules is showed in the inset. Adapted with permission from (Iwaszcuk et al.), © 2014 OSA.

In another work, the local field enhancement offered by resonant THz gold antennas can promote the access to strong-field phenomena, such as THz field-driven electron tunneling. In particular, for high THz electric field strengths, it is possible to bend the energy barrier at the gold surface of the antenna, allowing the tunneling of the electrons from the metal within one semi-optical cycle of the THz pulse, as it has been demonstrated by (Iwaszcuk et al., 2014). In this work, the electron photoemission has been indirectly characterized by the analysis of the UV-fluorescence emitted by the nitrogen plasma generated by the photoemitted electrons. As it is possible to observe from Figure 1.20d, the measured fluorescence as a function of the incident THz peak field shows a nonlinear trend that can be well

described by the *Fowler-Nordheim theory* for field-driven electron emission. As part of the project of this thesis work, we have conducted a similar study on out-of-plane THz resonant nanostructures (i.e. vertical nanocones) in different arrangements, as it will be seen in Chapter 3.

In the next paragraph, the theory of field-driven electron tunneling will be presented, by introducing a simple two-step model to describe the photoemission process. Then, different examples of field-driven photoemission from metallic nanostructures will be considered.

1.4 Electron photoemission

Since the last century, electron beams have been extensively used for several applications in different domains (e.g. in medical diagnosis, material science, electron beam lithography, electron microscopy, particles accelerators, etc.). Electrons are typically extracted from a metal surface, due to the high free electron density of metals ($\sim 10^{23} \text{ cm}^{-3}$). Although valence electrons can move freely inside the metal under the potential of the crystal lattice, they are confined within the metal and do not escape its surface. In order to let an electron overcome the potential barrier at the surface, it is necessary to provide an *ionization energy* higher than the *work function*, ϕ , of the metal, which can be supplied in different ways. For instance, by increasing the temperature of the metal (*thermionic emission*), by applying an electrostatic field (*cold field electron emission*) or through a combination of the two (*Schottky emission*).

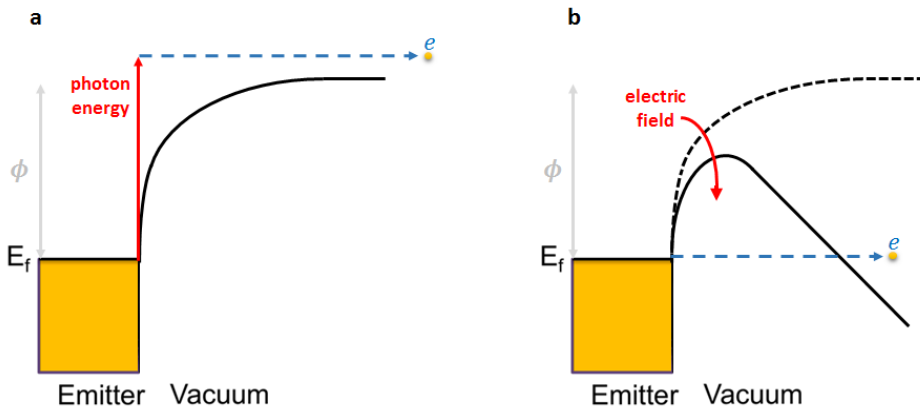


Figure 1.21 Energy schematic for photoemission processes
(a) Photon-driven and **(b)** field-driven electron photoemissions.

In the case of *electron photoemission*, the ionization process is induced by an incident light beam and it can be distinguished in two different regimes: the *photon-driven* regime and the *field-driven* regime. In the first case, also known as *photoelectric effect*, the electron is ejected from the metal by absorbing the energy of the impinging photon (Figure 1.21a). Furthermore, the use of powerful ultrashort laser pulses has enabled the observation of a nonlinear photoelectric effect (i.e. *multiphoton regime*), where the ionization process is originated from the simultaneous absorption of n photons, individually having an energy lower than the work function of the metal. In the field-driven regime, instead, the electric field associated with a laser pulse can instantaneously bend the potential barrier, enabling the tunneling of the electrons from the metal surface (Figure 1.21b). In the Keldysh formalism, the multiphoton and the tunneling regimes can be seen as two limiting cases of the same ionization process (Keldysh, 1965). The latter can be described via the Keldysh parameter $\gamma = \sqrt{\phi/2U_p}$, where ϕ is the work function of the material and U_p is the electron *ponderomotive energy*,

which represents the cycle-averaged kinetic energy of a free electron in an electromagnetic field, and is defined as:

$$U_p = \frac{e^2 E^2}{4m_e \omega^2} \quad (1.32)$$

where e is the electron charge, E is the optical field strength amplitude, m_e is the electron mass and ω is the optical frequency. The two regimes are then classified through the γ parameter: $\gamma \ll 1$ for the field-driven regime and $\gamma \gg 1$ for the photon-driven regime. It is important to note that the use of lower optical frequencies (i.e. longer wavelengths) favours the field-driven regime, since γ is directly proportional to the optical frequency ω . In particular, by means of intense fs-laser pulses it is possible to induce the *photoemission* of ultrashort electron bunches, which are extremely appealing for 4-dimensional time-resolved microscopy and diffraction techniques. In these techniques, ultrashort and confined electron bunches are extracted via photon-driven photoemission and employed in these 4D ultrafast techniques to study the dynamics of ultrafast phenomena (e.g. chemical reactions, phase transitions, membrane mechanical drumming, etc.) (Carbone et al., 2009; Park et al., 2009; Yurtsever et al., 2012; Zewail, 2010).

In the field-driven regime the coherent emission of electron bunches occurs within half of the optical cycle of the laser pulse, when the electric field is pointing toward the metal half space (Figure 1.22a), which can also ensure a precise synchronization between the emitted electrons and the optical pulse as well as the possibility of optical control over the photoemission process. In general, electron tunneling is traditionally obtained by focusing amplified high-power femtosecond laser pulses on selected photocathodes (i.e., cathodes which emit electrons under illumination). However, the electron emission area on the photocathode results limited by the radiation wavelength (via the minimum spot size achievable) of the incident optical pulses. Moreover, the light intensities necessary to reach $\gamma = 1$ are of the order of 10^{13} W/cm^2 at the wavelength of 800 nm, which exceeds the damage threshold of metals (Wellershoff et al., 1999). These constraints can be overcome by the use of metallic nanotips. In fact, the local electric field enhancement factor, β , provided by the so-called "*lightning rod effect*" (i.e., the confinement of the electric field on a conductive surface with a small radius of curvature) (Ermushev et al., 1993) of metallic nanotips can help to relax the required optical intensity for the tunneling emission, and to localize the tunneling process on the nanotip apex. This, in turn, provides a better spatial resolution than the one achievable with conventional optical pulses (Bormann et al., 2010; Hommelhoff et al., 2006).

1.4.1 Simple man's model for field-driven photoemission from metal nanotips

Many important phenomena occurring in the tunneling regime, such as *high harmonic generation* (HHG), *attosecond pulse generation* and *above threshold ionization*, can be explained using a simple physical picture, the so-called *simple man's model* (Corkum, 1993), which is based on the separation of the process in two steps: (i) electron emission and (ii) subsequent acceleration of free electrons in the optical field. In the framework of this model, the electron dynamics after the extraction from the metal surface is described using classical equations of motion for an electron in the presence of the laser field, neglecting the effect of the atomic potential. In the first step, the strong electric field bends the potential barrier at the metal surface, enabling the tunneling of the electrons. The emission process can be approximated as a static field emission, so that it is possible to retrieve the emission current density J via the Fowler–Nordheim (FN) equation (Fowler & Nordheim, 1929):

$$J = \frac{aE^2}{\phi} \exp\left(-\frac{b\phi^{3/2}}{E}\right) \quad (1.33)$$

Here, $E = \beta E_0$ is the product between the field enhancement factor β and the time-dependent optical field strength E_0 within the adiabatic approximation, while $a = \frac{e^3}{16\pi^2\hbar} = 1.53 \cdot 10^{-6} \text{ A eV V}^{-2}$ and $b = \frac{4\sqrt{2m_e}}{3\hbar e} = 6.829 \cdot 10^9 \text{ eV}^{-3/2} \text{ V m}^{-1}$ are the first and the second Fowler-Nordheim constants, respectively. Equation (1.33) can be conveniently re-written as:

$$\log\left(\frac{J}{E^2}\right) = C_1 + C_2 \frac{1}{E} \quad (1.34)$$

where $C_1 = \log\left(\frac{\phi}{a\beta^2}\right)$ and $C_2 = -\frac{b\phi^{3/2}}{\beta}$. In this way, it is possible to represent experimental data in a linear plot, allowing to retrieve the field enhancement factor β from the slope of the linear fit (as it will be done in Chapter 3 of this thesis):

$$\beta = -b\phi^{\frac{3}{2}}/C_2 \quad (1.35)$$

After the emission, the metal potential is neglected (strong-field approximation) and the classical equation of motion is solved for a free electron in an oscillating electric field, with zero initial velocity. Depending on the time of emission, the electron might return to the metal surface. Then it can be

reabsorbed, leading to the emission of a photon (HHG). Alternatively, the electron is elastically or inelastically scattered.

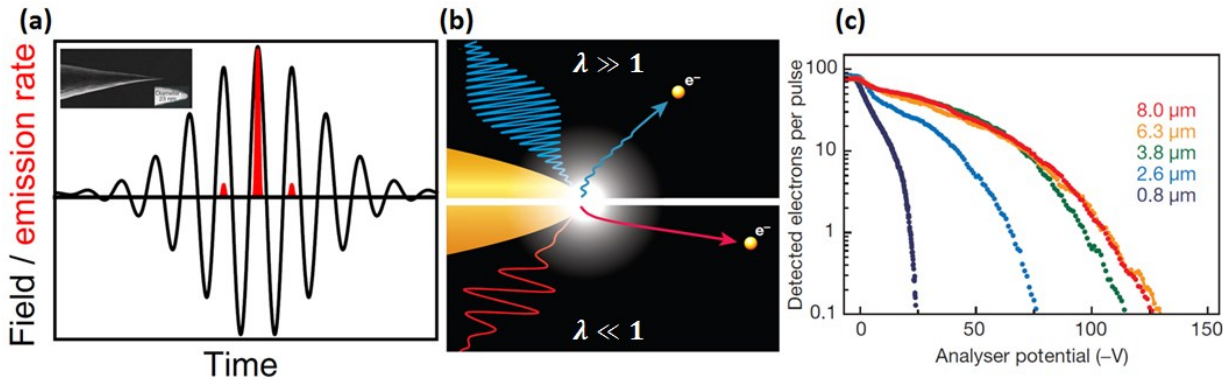


Figure 1.22 Electron photoemission from metallic nanotips

(a) The highly nonlinear time-dependent emission rate adiabatically follows the electric field. (b) Sketch of the trajectory of extracted electrons whether the quiver amplitude is smaller (top, short wavelength excitation) or larger (bottom, long wavelength excitation) than the decay length of the optical near-field. (c) Energy spectra of the photoemitted electrons, showing the energy cut-off for different incident wavelengths. Adapted with permission from (Echternkamp et al.) © 2016 Springer Nature and (Herink et al.) © 2012 Springer Nature.

Recently, increasing interest has been paid towards novel features offered by the sub-wavelength spatial confinement of the optical fields. In particular, it has been demonstrated that for sufficiently long wavelengths of the driving optical field, the extracted electrons can leave the vicinity of the nanotip within half of the optical-cycle (Herink et al., 2012). Thus, increasing the wavelength, the electron dynamics move from the classical quiver motion in an oscillating field towards a “sub-cycle” regime, where the energy transfer is directly proportional to the locally enhanced optical field. This transition is characterized by a spatial Keldysh parameter, δ , which relates the decay length l_F of the local optical field from the metal surface to the electron quiver amplitude $l_q = eE/m_e\omega^2$ as follows:

$$\delta = \frac{l_F}{l_q} = \frac{l_F m_e \omega^2}{e E} \quad (1.36)$$

Whereas the Keldysh parameter describes the degree of adiabaticity of the emission process (step 1 of the Simple man’s model), the ratio δ characterizes the propagation and acceleration of electrons (step 2 in the Simple man’s model). Thus, for $\delta \gg 1$, the electron quivers in a nearly homogeneous field over multiple optical cycles in the classical way. For $\delta \ll 1$, electrons rapidly escape from the tip-enhanced field within a time much shorter than an optical cycle (Figure 1.22b). The δ -parameter scales proportionally to E^{-1} and has an inversely quadratic dependence with the optical wavelength. Experimentally, δ can be reduced by increasing the intensity or the wavelength, or by reducing the

field decay length by using more confined fields at sharper tips. Therefore, the sub-cycle regime ($\delta \ll 1$) can be reached more easily at larger wavelengths, and at reduced (non-destructive) intensities.

The energy spectra of the photoemitted electrons depends on the final kinetic energy of the accelerated electrons retrieved from the step 2 as well as from the current emission rate calculated in the step 1 of the Simple man's model. From the scaling of the ponderomotive potential U_p (Equation (1.32)), one expects the cut-off energies for a constant local intensity to depend quadratically on the wavelength. However, in (Herink et al., 2012), the authors have observed that the cut-off energy begins to saturate for longer wavelengths, since the quiver amplitude starts to exceed the nanolocalized field decay length and the electrons escape the high driving field region within a fraction of the driving period (Figure 1.22c).

1.4.2 THz field-driven electron emission from metallic nanostructures

As mentioned above, according to the Keldysh theory, the field-driven photoemission process can be facilitated by employing long radiation wavelengths. In particular, THz frequencies are highly suitable for field-driven photoemission (Herink et al., 2014; Iwasczuk et al., 2014; Li & Jones, 2016; Zhang et al., 2015), providing the additional possibility of a precise temporal control of the emitted electron bunches, thanks to the intrinsic carrier envelope phase stability (i.e. the stability of the phase between the carrier wave and the position of the intensity envelope of the pulse) of the THz pulses (Yoshioka et al., 2013). As it has been observed in a recent work (Li & Jones, 2016), intense single-cycle THz pulses (max peak electric field of 400 kV/cm; central frequency of ~ 0.15 THz), can lead to the emission of ultrafast electron bunches with measured maximum cut-off energies up to 5 keV from tungsten nanotips with a weak dependence from the tip radius R , that span the range 10 – 1000 nm (Figure 1.23a and 1.23b).

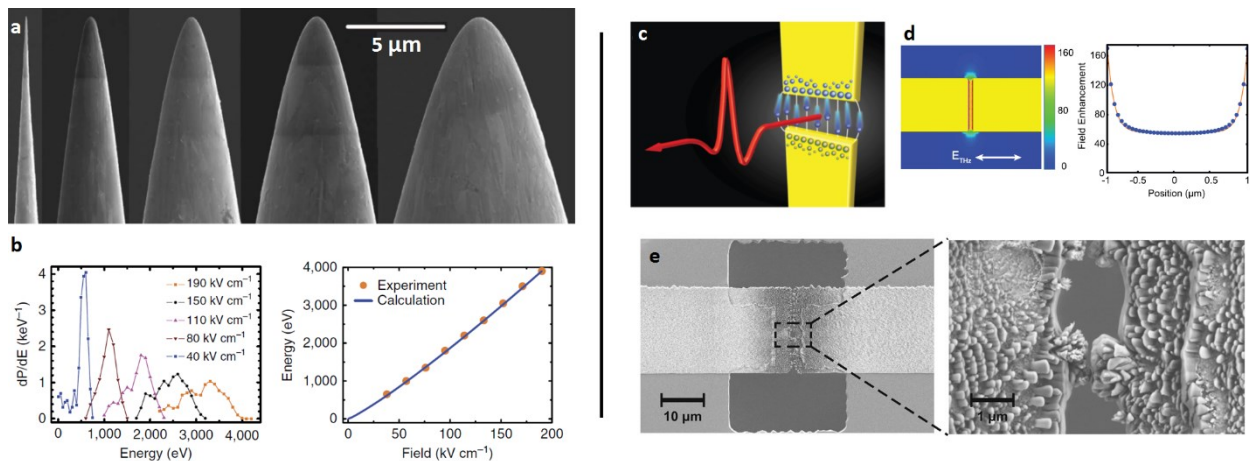


Figure 1.23 THz field-driven photoemission from metallic nanotips

(a) SEM images of the five tungsten tips used for THz-field photoemission. From left to right, the tip radii are $R = 20, 100, 200, 400$, and 800 nm. (b) Energy distribution of the electrons emitted from a tip with $R = 130$ nm for different incident terahertz fields. The relative cut-off energies show a linear dependence on the impinging THz field. Adapted from (Li & Jones, 2016). (c) Sketch of THz field-driven electron emission in a vacuum split-gap dipole antenna within the antenna gap. (d) Estimated field enhancement factors within the gap. (e) SEM image of the gap after a long term (>1 h) exposure to the high-field THz radiation, which restructures induces the deformation of the antenna gap shape. Adapted with permission from (Zhang et al.) © (2015) AIP Publishing.

In this configuration, the electron acceleration process can be described as follows: an electron ejected from the surface rapidly accelerates away from the tip in the locally enhanced field, $E = \beta E_0$, where E_0 is the incident THz peak field. The local field drops rapidly down to E_0 as the electron travels a distance comparable, and proportional, to R . Thus, the electron energy cut-off can be retrieved calculating the work done by the enhanced local field, which is given by the product

between the average Coulomb force, $\frac{1}{2}e\beta E_0$ on an electron with charge, e , and the field decay length, which is comparable with the tip radius, R

$$\Delta E = \frac{1}{2}e\beta E_0 R \quad (1.37)$$

At the same time, THz resonant arrays of dipole antennas have also been employed for field-driven photoemission, offering an additional improvement thanks to the stronger local field enhancement provided by the sub-wavelength confinement of the incident light at the resonance condition. For instance, (Zhang et al., 2015) has observed THz field-driven photoemission across the gap between two dipole antennas resonating at 0.6 THz (Figure 1.23c), illuminated by intense THz pulses from a LiNbO₃ source (maximum incident field amplitude of 200 kV/cm). The estimated field enhancement varied in this case between 60 and 160 across the gap (Figure 1.23d), with a field threshold value for an observable tunneling current of 10.2 MV/cm. The measured photoemitted current across the gap was well described by the Fowler-Nordheim equation, confirming the pure field-driven nature of the process. Moreover, the quiver amplitude is much larger than both the decay length and the 2-μm-long gap ($\delta \ll 1$), thus the photoemitted electrons are able to arrive to the other extremity of the gap with a straight trajectory. However, as it is possible to observe from the SEM images taken after a long exposure (> 1 h) to intense THz pulses, the antenna extremities resulted in severe damage (Figure 1.23e). This was due to the collision of the high-energy field-emitted electrons on the other side of the antenna gap, where the excess kinetic energy melts the gold surface (Caverley, 1959). Furthermore, the closure of the gap can also be due to the electromigration driven by intense THz electric fields, where the electron tunneling across the gap results in a strong DC potential that tear gold ions from one side to the other of the gap (Black, 1969).

Only planar resonant nanostructures have been explored so far for field-driven photoemission. In such case, the close presence of the substrate (or the proximity of another antenna in a dimer configuration, as in the case presented above) clearly hampers the use of the emitted electron bunches for further applications. In Chapter 3 we will see how this limit can be overcome by means of THz resonant gold nanostructures in an out-of-plane configuration.

2 DEVELOPMENT OF YTTERBIUM BASED THZ SOURCES

The use of THz radiation in scientific and industrial applications has been continuously growing over the last decades (Mittleman, 2017), also thanks to the increasing availability of new THz sources. In particular, THz pulses with a bandwidth wider than 10 THz are desired to investigate optical properties and fingerprints of materials in a wide frequency range (Zalkovskij et al., 2012), as well as to study the dynamics in condensed-matter systems via ultrafast THz 2D spectroscopy (Woerner et al., 2013) with high temporal resolution. At the same time, high THz electric fields (>100 kV/cm) are required to enable, e.g., field-driven electron photoemission (Li & Jones, 2016), or the study of localized nonlinear phenomena (Tarekegne et al., 2015). Such broadband and intense THz pulses can be obtained via, e.g., OR in organic crystals (Schneider et al., 2006) and two-color plasma sources (Blanchard et al., 2009). Moreover, the use of driving lasers with high average powers (i.e. high repetition rates) represents an asset for improving the signal-to-noise ratio in THz measurements. In this regard, Yb-laser systems have been surpassing the well-established Ti:Sapphire laser technology in terms of efficiency, cost-effectiveness, and average output power, due to (i) the availability of efficient high-power diodes to pump Yb transitions, (ii) the small quantum defect ($<10\%$) of Yb-doped materials resulting in a lower heat deposition, and (iii) the possibility of engineering the surface-to-volume ratio in thin-disks-, fibers- or slab-based architectures, which significantly improves heat removal.

In this Thesis work, Yb-laser pulses have been used to drive the generation of high-field THz pulses via collinear OR in an HMQ-TMS organic crystal (since it presents a good phase-matching at the emission wavelength of Yb-lasers) as well as for the emission of extremely broadband THz pulses via two-color mixing in air plasma. In particular, I have employed a Yb-doped potassium gadolinium tungstate (Yb:KGW) laser (*Pharos PH1-SP-1mJ, Light Conversion*), emitting 170-fs-long pulses centered at 1030 nm with a maximum pulse energy of 1 mJ and a tunable repetition rate up to 1 MHz (6 W of average power: 1 mJ @ 6 kHz). Both THz sources will be described in this chapter, presenting the full characterization of the generated THz pulses.

The discussion and the images of this chapter were adapted from:

A. Rovere, Y. G. Jeong, R. Piccoli, S. H. Lee, S. C. Lee, O. P. Kwon, M. Jazbinsek, R. Morandotti, L. Razzari, "Generation of high-field terahertz pulses in an HMQ-TMS organic crystal pumped by an ytterbium laser at 1030 nm" *Opt. Express*, 2018, 26, 2509-2516 and:

R. Piccoli, A. Rovere, Y. G. Jeong, Y. Jia, L. Zanotto, F. Légaré, B. E. Schmidt, R. Morandotti, L. Razzari, "Extremely broadband terahertz generation via pulse compression of an Ytterbium laser amplifier" *Opt. Express*, 2019, 22, 32659-32665

These articles are published under the OSA Open Access Publishing Agreement.

2.1 Intense THz pulses from HMQ-TMS organic crystal pumped at 1030 nm

For the work presented in this section, I have designed and set up the THz system, performed the experimental characterization of the source, and led the data analysis. I also carried out the proof-of-principle nonlinear test.

As it has already been mentioned before, one of the most commonly used mechanism to generate intense few-cycle THz pulses relies on OR in nonlinear organic crystals (Dexheimer, 2007). In particular, HMQ-TMS possesses a high electro-optic response, and presents a large OR phase-matching band compared to other organic nonlinear optical crystals. As it has been already observed by (Vicario et al., 2015), the THz spectral bandwidth and the central frequency of the THz pulses generated via OR in HMQ-TMS can be straightforwardly controlled by varying the pump wavelength by means of a tunable OPA laser (Figure 2.1a).

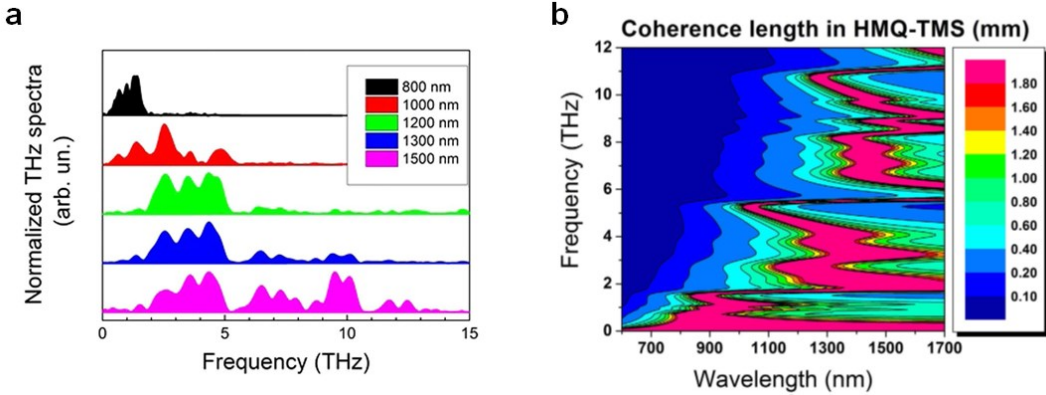


Figure 2.1 THz spectra and coherence length for HMQ-TMS

(a) Shaping of the Terahertz spectral output by tuning the pump laser central wavelength. (b) Two-dimensional plot of the coherence length for HMQ-TMS, giving a direct representation of the optical rectification phase matching condition for different pump wavelengths. Adapted from (Vicario et al., 2015).

Figure 2.1b shows the two-dimensional map of the coherence length for HMQ-TMS as a function of the pump wavelength and the emitted THz frequency. As one can see, toward longer pump wavelengths the coherence length is significant for a larger range of THz frequencies. Nevertheless, HMQ-TMS can also be pumped at wavelengths shorter than those typically required by, e.g., DAST and OH1, which are usually in the range 1.3-1.5 μm , yet keeping a good conversion efficiency. In what follows, we will show how 1030 nm pulses from an amplified Yb-laser can be effectively used to pump an HMQ-TMS organic crystal to generate few-cycle high-peak-electric-field THz pulses in a simple collinear scheme, providing an advantageous geometry for many practical implementations (Rovere et al., 2018).

2.1.1 Characterization of the high-field THz pulses

In this measurement, an HMQ-TMS crystal with a thickness of 630 μm has been used for the generation of THz pulses. For the THz electric field characterization, we have exploited a standard THz-TDS setup in a nitrogen-purged environment, as shown in Figure 2.2. The residual pump radiation after the HMQ-TMS crystal has been blocked by means of a 100- μm -thick black polyethylene sheet. The generated THz radiation has been collected and finally focused onto a 300- μm -thick $<110>$ GaP crystal by means of a set of gold off-axis parabolic mirrors (OPMs). We have acquired the time trace of the THz electric field through the standard EOS technique (Section 1.2.3 in the previous Chapter), using the GaP crystal as the detector, with a delay step of 15 fs. Since the laser output beam waist (4.5 mm in diameter at $1/e^2$ of the intensity) is larger than the clear aperture of the HMQ-TMS crystal (diameter of 3 mm), a pinhole has been used to limit the pump beam size to the crystal's aperture. We have found this configuration more efficient than the use of an optical telescope to reduce the pump beam size, since long term exposure (i.e., several hours) of the organic crystal to a pump beam with a spot size < 3 mm eventually resulted in local damage and a subsequent reduction of the conversion efficiency. Note that all the measurements presented in the following have been performed in a nitrogen-purged environment.

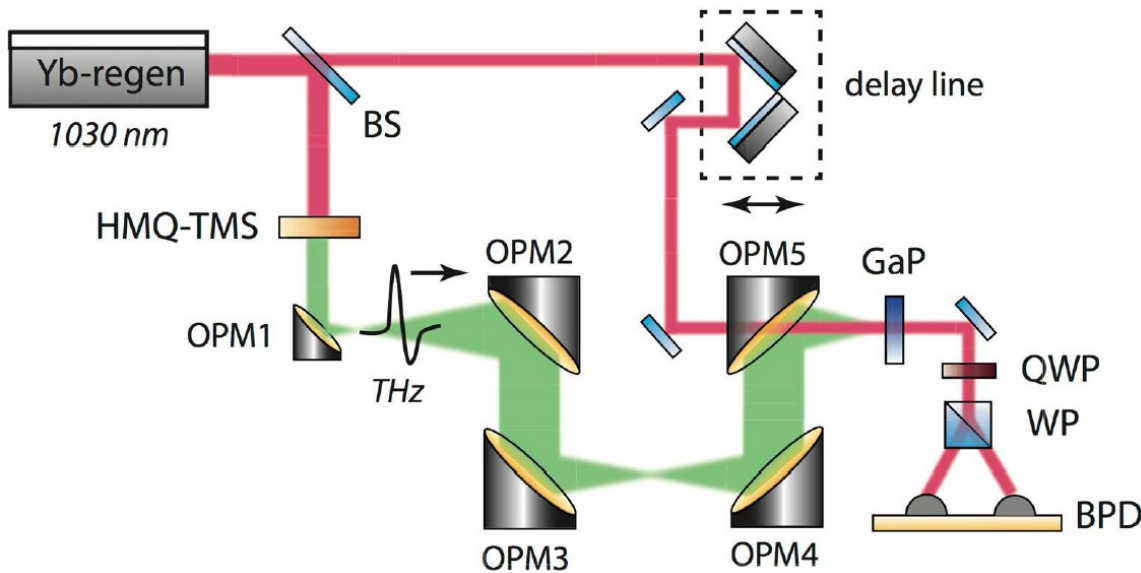


Figure 2.2 TDS setup used for the characterization of the HMQ-TMS THz source

BS – beam splitter 80:20, OPM – 90-deg off-axis parabolic mirrors (focal length of OPM1: 0.5", OPM2: 6", OPM3 and OPM4: 3", OPM5: 2"), QWP – quarter wave plate, WP – Wollaston prism, BPD – balanced photodiodes. Detection is performed via EOS in a 300- μm -thick $<110>$ GaP crystal. Reprinted with permission from (Rovere et al.) © 2018 The Optical Society.

This source provides few-cycle THz pulses (Figure 2.3a) with an emission spectrum extending beyond 3 THz (Figure 2.3b). The dip in the frequency spectrum located at 1.7 THz is associated with

a phonon mode of the HMQ-TMS crystal (Vicario et al., 2015). It has also been possible to numerically simulate the detected output spectrum of the THz source, under the plane-wave non-depleted pump approximation and not considering cascaded nonlinear effects (see Appendix I for details). More specifically, in the calculations done by our collaborator at the Zurich University of Applied Sciences (ZHAW), the output power spectrum of our Yb laser system, the refractive index, and absorption coefficient of the organic crystal at both optical and THz frequencies (Brunner et al., 2014) have been considered, as well as the GaP detector response function, taking into account its THz (Leitenstorfer et al., 1999) and optical characteristics (Aspnes & Studna, 1983). As it is possible to observe in Figure 2.3b, there is a very good agreement between the experimental and numerical results, especially in terms of the overall emission band and the position of the phonon absorption.

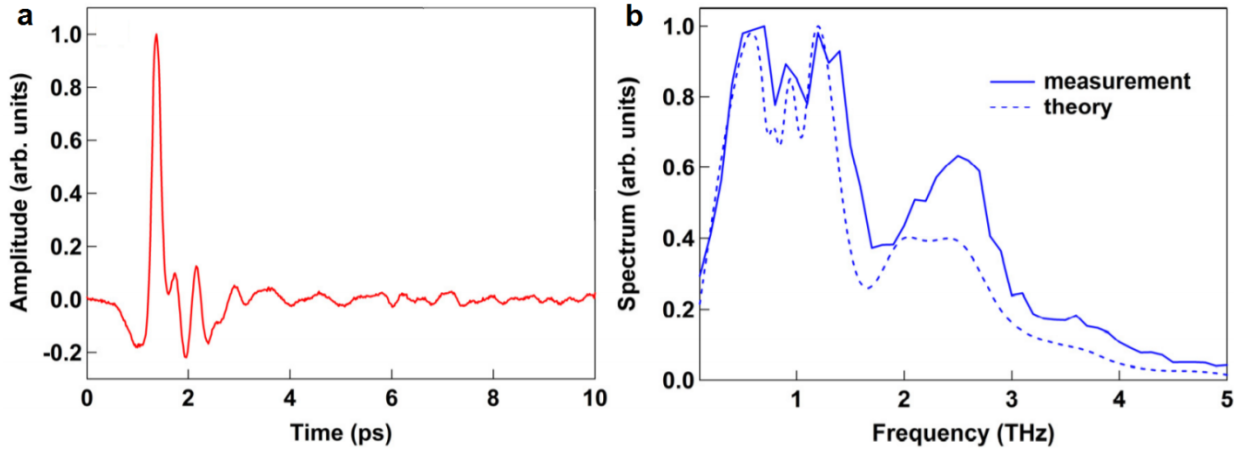


Figure 2.3 THz waveform and spectrum generated by OR in HMQ-TMS crystal

(a) THz electric field waveform emitted by the 630- μm -thick HMQ-TMS crystal and retrieved via EOS using a GaP detection crystal. (b) Measured (solid) and calculated (dashed) THz emission spectra. Reprinted with permission from (Rovere et al.) © 2018 The Optical Society.

We have then estimated the strength of the THz peak electric field retrieved through EOS. For small modulations, the differential intensity measured by the balanced photodiodes (see Figure 2.2) is directly proportional to the THz field strength, as shown by the following relation (see Section 1.2.3 of the Introduction):

$$\frac{\Delta I}{I} = \frac{2\pi d n_0^3 r_{41} t E_{\text{THz}}}{\lambda_0} \quad (2.1)$$

where $\Delta I/I$ is the normalized intensity modulation, E_{THz} is the THz peak electric field, λ_0 is the pump central wavelength, while $n_0 = 3.11$, $t = 0.46$, $d = 300 \mu\text{m}$, and $r_{41} = 0.97 \text{ pm/V}$ are the refractive index at λ_0 , the THz transmission coefficient, the thickness and the electro-optic coefficient of the $<110>$ -oriented GaP crystal, respectively. In order to avoid over-rotation in the GaP crystal, as well as additional nonlinear effects, the incident THz signal has been attenuated by placing 2 HR (> 5000

$\Omega \cdot \text{cm}$) silicon wafers in the beam path (each of them providing about 70% of electric field transmission). The measured THz peak electric field as a function of the pump fluence (which is estimated as the ratio between the incident pump energy on the crystal and the area of the pin-hole) is reported in Figure 2.4a, showing a quasi-linear trend with a maximum THz peak electric field of around 200 kV/cm. However, it has to be noted that since the optical probe pulse is relatively long (FWHM of 170 fs), it does not allow to fully resolve the amplitude of the generated THz electric field oscillations. To illustrate this, we show, in the inset of Figure 2.4a, the absolute value of the measured electric field trace E_{meas} (blue) compared to the one of a THz waveform E_{dec} (Keathley et al.) obtained by deconvoluting the measured trace with a Gaussian optical probe G of 170 fs, according to the formula: $E_{\text{meas}} = E_{\text{dec}} * G$. As it is evident from this evaluation, the effective THz peak value can be up to 1.8 times higher than the one extracted from our EOS measurement, which corresponds to a peak electric field of about 350 kV/cm at the detection crystal position.

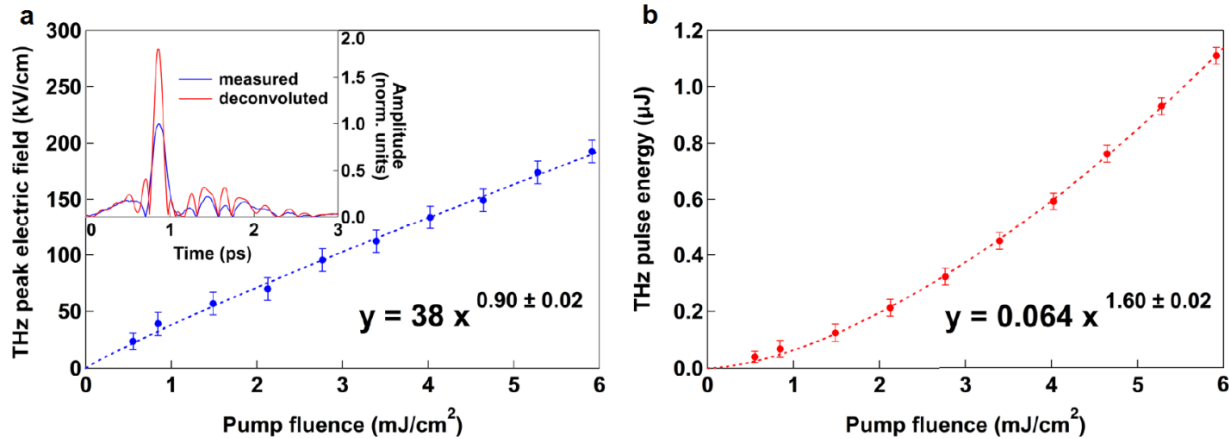


Figure 2.4 THz electric field peak and energy scaling versus pump fluence

(a) Peak electric field and (b) energy of the THz pulses generated by the 630- μm -thick HMQ-TMS crystal as a function of the incident pump fluence. The inset shows the normalized absolute values of the measured THz field (blue) and of a waveform obtained by deconvoluting the measured trace with a Gaussian optical probe of 170 fs - FWHM (Keathley et al.). The formulas reported in both figures represent the best fit of the experimental data (dashed lines). Reprinted with permission from (Rovere et al.) © 2018 The Optical Society.

We also measured the THz pulse energy by means of a pyroelectric detector (THZ-I-BNC from *Gentec-EI*). The generated THz energy is presented in Figure 2.4b, showing a super-linear dependence on the pump pulse fluence. At the maximum incident pump fluence of about 5.9 mJ/cm² (well below the damage threshold previously reported for the HMQ-TMS crystal, i.e. > 20 mJ/cm² (Vicario et al., 2015)), the generated THz pulses reach an energy value of about 1.1 μJ per pulse, corresponding to a significant conversion efficiency of 0.26%. Remarkably, the investigated THz generation process can be scaled up, in terms of THz energy and peak electric field, by employing larger aperture crystals and higher pump energies.

2.1.2 Nonlinear transmission in a InGaAs thin film

In order to demonstrate the potential of this source for nonlinear THz investigations, we have performed a proof-of-principle experiment (open-aperture Z-scan) on a $d = 500\text{-nm-thick}$ n-doped $\text{In}_{0.53}\text{Ga}_{0.47}\text{As}$ thin film (carrier density of $\sim 2 \times 10^{18} \text{ cm}^{-3}$, band gap of 0.75 eV), deposited on an InP substrate of refractive index $n = 3.1$. Indeed, Z-scan is a very common nonlinear characterization technique that enables, for instance, the determination of the Kerr nonlinearity as well as the nonlinear absorption coefficients of a material from intensity-dependent transmission changes (Zhang et al., 2012). Note that a more detailed and quantitative description of the physical phenomena underlying the observed nonlinear response can be found in (Razzari et al., 2009).

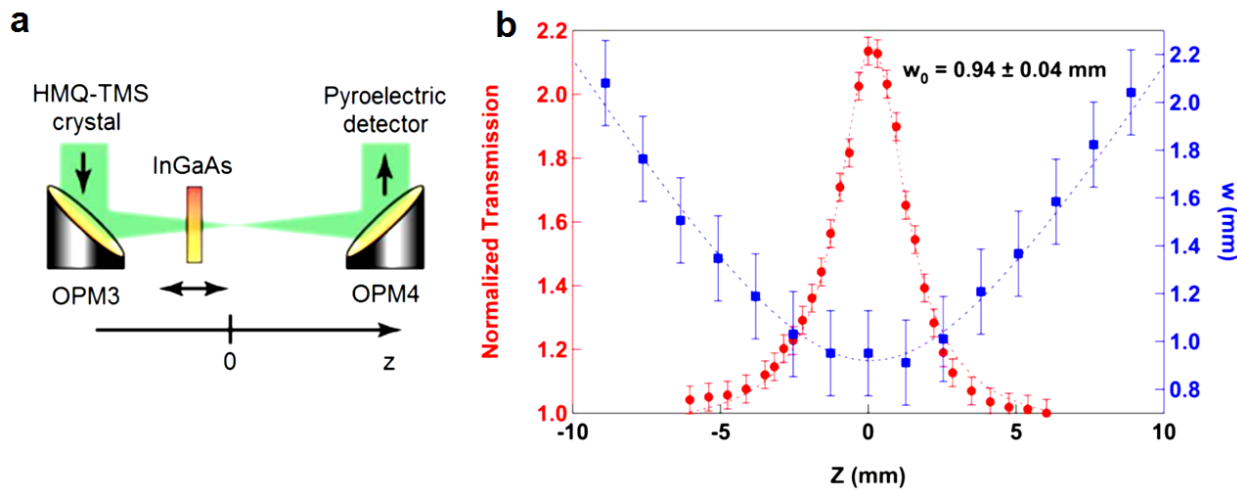


Figure 2.5 Z-scan measurement

(a) Schematic of the setup for the Z-scan measurement. (b) Normalized transmission of the InGaAs film (red points) and THz beam waist values (blue points) measured as a function of the z position ($z = 0$ corresponds to the THz focal position). Reprinted with permission from (Rovere et al.) © 2018 The Optical Society.

In this measurement, we have recorded the THz energy transmitted through the sample while it was scanned along the propagation direction z across the focused THz beam (see Figure 2.5a). In particular, the THz transmission of the sample can be expressed by:

$$E_t = \frac{1}{Y_0 + Y_s} (2Y_0 E_i - Jd) \quad (2.2)$$

where E_t and E_i are the transmitted and incident THz fields, respectively, $Y_0 = (377 \Omega)^{-1}$ and $Y_s = nY_0$ are the free-space and substrate admittances, while J is the current density in the film (Razzari et al., 2009). The transmission of the sample at low excitation levels ("linear regime") is approximately 3%, which is mainly related to the high conductivity of the InGaAs thin film, since measurements on the InP substrate only have shown an overall transmission (including absorption and reflection losses) of about 60%. For the case of the selected sample, the strong transmitted THz field can induce

an intervalley transition (from the Γ to the L valley) of the carriers within the InGaAs conduction band, thus affecting the current density J in Equation 2.2. Since the carrier mobility in the satellite L valley is lower, the film conductivity is consequently reduced (and so the driven current), thus resulting in a higher THz transmission. For each point of the scan along the z direction we have extracted the normalized transmission as the detected transmitted energy divided by the one measured at low THz intensity (i.e., away from the THz focus, at one extremity of the scanned range). The results of this measurement are shown in Figure 2.5b (red circles). We have observed a significant saturation of the THz absorption, with a maximum transmission increase of about 2.2 times at the focus. This transmission change is related to the change of the THz beam waist (and thus to the change in its intensity) along the z direction between OPM3 and OPM4, which have been retrieved via knife-edge measurements on the THz beam. The results of this characterization are also reported in Figure 2.5b (blue squares). In this way, we have estimated a THz beam waist of 940 μm at the focal position of OPM3. In a previous Z-scan experiment performed on the same sample (using THz pulses generated via OR in a large-aperture ZnTe crystal pumped by 30 mJ, 30-fs-long optical pulses at 800 nm(Razzari et al., 2009)) a similar increase in THz transmission was found for a peak electric field of around 200 kV/cm. This value is in fair agreement with our EOS measurement. Indeed, considering the longer focal length of OPM3 ($f = 3''$) in comparison to OPM5 ($f = 2''$), the THz beam waist at the Z-scan sample position is 1.5 larger than the one at the GaP detection crystal (a value also confirmed by an additional knife-edge measurement, not shown). Thus, the THz peak electric field that we can estimate from our EOS characterization at the Z-scan sample position is about 230 kV/cm (taking into account the deconvolution factor mentioned above). However, a direct comparison with the experiment reported in (Razzari et al., 2009) is difficult, due to differences in the temporal and spectral shapes of the THz pulses employed in the two cases, which also affect the nonlinear response of the doped InGaAs sample. This characterization further confirms the significant electric field strength of the THz pulses generated using the proposed configuration. As we will see in Chapter 3, this source has also been used to drive electron emission from vertical, THz resonant nanostructures.

2.2 Two-color plasma generation of ultra-broadband high-field THz pulses

For the work presented in this section, I was in charge of the experimental part regarding the generation and detection of the broadband THz pulses, while R. Piccoli took care of the pulse compression stage for the Yb-laser pulses and led the data analysis.

Two-color plasma sources are advantageous with respect to OR for the generation of intense broadband THz pulses. In fact, unlike bulk nonlinear crystals, gases are continuously renewable and are thus not limited by damage issues, thus they can be pumped at extremely high intensities, being capable of providing peak electric fields higher than MV/cm (Oh et al., 2013). Moreover, the generated THz bandwidth is practically limited only by the laser pump pulse duration, thanks to the very low dispersion of gases (Karpowicz et al., 2008). In this section, we report the generation of ultra-broadband THz pulses via a two-color plasma source, employing Yb-laser pulses compressed in time by means of a nonlinear technique exploiting a gas-filled hollow-core fiber (HCF), which is described in the following paragraph. HCFs are known to withstand average powers higher than 100 W (Hädrich et al., 2013) and high pulse energies (Cardin et al., 2015). These make the combination of Yb lasers and HCFs, a unique tool for the generation of high-average-power, high-field and extremely broadband THz radiation via two-color-excited air plasma.

2.2.1 Spectral broadening and temporal compression of Yb-laser pulses using an argon-filled hollow-core fiber

In general, the post pulse compression process can be divided in two steps: the initial spectral broadening of the optical pulses and the subsequent compression of the pulse duration. The spectral broadening can be achieved through a nonlinear interaction, named *self-phase modulation* (SPM), in a gas-filled HCF (a capillary fiber made of fused-silica) (Nisoli et al., 1996). The fiber is kept stretched and the propagation of the laser pulse along the fiber occurs through grazing incidence reflections at the dielectric inner surface. The losses caused by these multiple reflections greatly affect higher order modes, thus only the fundamental mode can propagate in a sufficiently long fiber. The SPM leads to the chirp of the optical pulses (i.e., the temporal dispersion of the pulse instantaneous frequency) and the generation of new frequencies (see Appendix II for a detailed description of the SPM process). Subsequently, the pulse duration can be strongly reduced by dispersive compression (using gratings, prisms, chirped mirrors, etc.), through the (total or partial) compensation of the SPM-induced chirp. In a seminal paper, (Matsubara et al., 2012) demonstrated how 35-fs-long pulses emitted by a Ti:Sapphire laser can be compressed down to 10 fs via SPM-induced broadening in an Ar-filled HCF, followed by a chirped mirror pair (i.e., mirrors with a pre-designed dispersion, see Figure 2.6a).

These ultrashort compressed laser pulses have then been used in a two-color plasma source for the generation of ultrabroadband THz pulses, coherently detected via EO sampling (Figure 2.6b). In a previous work by our group, it has been shown that the hundreds of fs-long pulses emitted by commercially-available Yb amplified laser systems can be extremely broadened in gas-filled HCF and then compressed down to the single-cycle level, achieving high compression factors, high transmission, and high beam quality (Jeong et al., 2018). Note that the use of compressed Yb-laser pulses for the generation and detection of extremely broadband THz pulses would allow to obtain THz sources with higher repetition rates and output power levels than the ones provided by the Ti:Sapphire lasers. Considering this, we have developed a Yb-laser-based ultrabroadband THz source, as resumed in what follows.

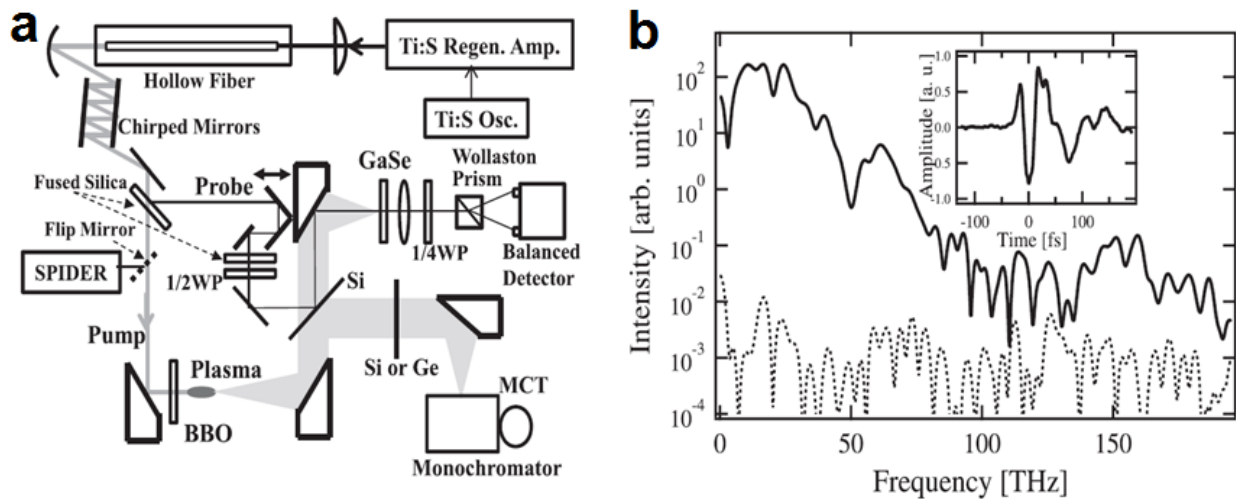


Figure 2.6 Ultrabroadband THz pulses generated by using a Ti:Sapphire laser
(a) Experimental setup for the ultrabroadband infrared pulse generation and detection (MCT: cooled mercury cadmium telluride detector; 1/4WP: Quarter-waveplate). **(b)** Fourier transformed spectrum of the THz pulse measured by EO sampling with a 20- μm thick GaSe crystal. Inset shows the temporal electric field profile. Adapted with permission from (Matsubara et al.) © 2012 AIP Publishing.

The 170-fs-long laser pulses (energy per pulse of 0.94 mJ, repetition rate of 6 kHz) emitted by the Yb:KGW regenerative amplifier were focused into a 1.6-m-long HCF (500 μm of inner diameter - *few-cycle Inc.*) filled with Ar gas at the static pressure of 2.8 bar, to provide the required third-order nonlinearity and broaden the pulse spectrum via SPM. The input 1-mm-thick fused silica window was anti-reflection coated at 1030 nm, while the output window was uncoated, not to introduce an additional spectral phase to the output pulses. After the fiber, the output beam was collimated with an Al-coated mirror ($f = 1 \text{ m}$) and compressed by four bounces on broadband chirped mirrors (PC1611, *UltraFast Innovations*). Such chirped mirrors present high-reflectivity between 800 nm and 1200 nm, providing -150 fs² at each bounce, for a total *group delay dispersion* (GDD) of -600 fs². The

GDD is related to the chromatic dispersion of an optical element and it is defined as the derivative of the group delay with respect to the angular frequency.

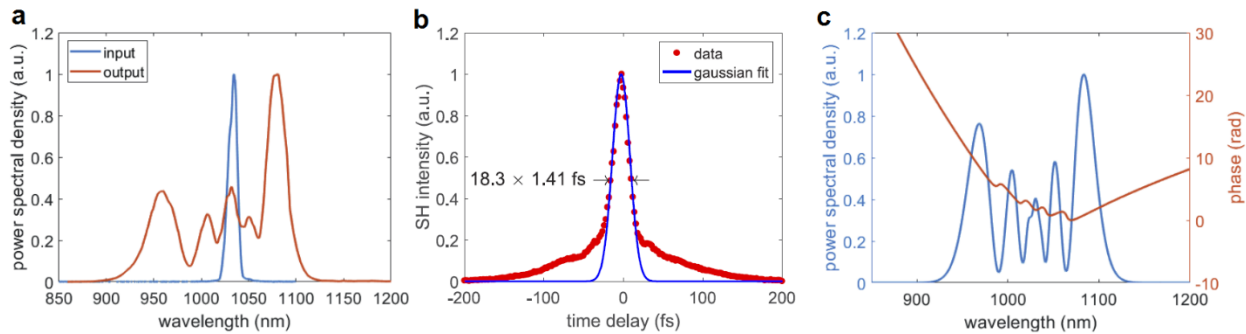


Figure 2.7 Compressed pulse characterization

(a) Input (blue) and HCF output (orange) experimental laser pulse spectrum. (b) Autocorrelation trace corresponding to the compressed spectrum, showing a $\sim 18\text{-fs}$ -long pulse (assuming the deconvolution factor for a Gaussian pulse of 1.41). (c) Simulated output spectrum (blue) and spectral phase (orange) at the output of the HCF. Reprinted with permission from (Piccoli et al.) © 2019 The Optical Society.

The spectrum of the compressed pulses was recorded (Figure 2.7a) with two real-time spectrometers (*Avantes UV-NIR Duo*), while their temporal duration was estimated via a second-harmonic autocorrelator employing a 50- μm -thick-BaB₂O₄ (BBO) crystal (Figure 2.7b). The spectrum is broadened along the propagation in the HCF by SPM between approximately 900 nm and 1100 nm, with an overall transmission efficiency exceeding 70%. After the chirped mirrors, the pump pulses are compressed down to ~ 18 fs FWHM (compression factor of about 9) which is close to the Fourier limit of ~ 15 fs calculated by taking the direct Fourier transformation of the output spectrum (orange line) illustrated in Figure 2.7a. A lower pedestal remained visible after compression (red dots in Figure 2.7b), as the compensation of higher orders dispersion terms was not optimal in our configuration. The output spectrum in Figure 2.7a shows a very good agreement with the numerical results reported in Figure 2.7c. In particular, the simulated spectrum has been retrieved through a 1D + 1 numerical model based on the generalized nonlinear Schrödinger equation, which includes dispersion, the nonlinear Kerr terms, self-steepening (Boyd, 2008), multi-photon absorption and ionization (Jeong et al., 2018).

2.2.2 Characterization of the broadband THz pulses

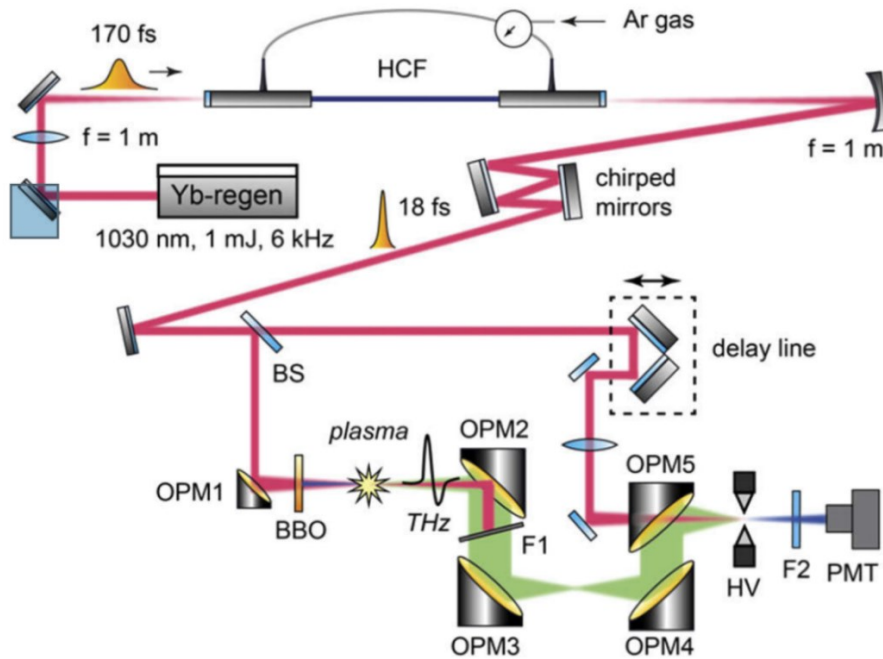


Figure 2.8 Schematic of the setup for the generation and characterization of broadband THz pulses
HCF – hollow-core fiber; BS – 90:10 beam splitter; OPM1 – off-axis parabolic mirror $f = 4''$; OPM2, OPM3, and OPM4 $f = 3''$; OPM5 $f = 2''$; F1 – long-pass filter; HV – high voltage electrodes; F2 – short-pass filter for 515 nm; PMT – photomultiplier tube. Reprinted with permission from (Piccoli et al.) © 2019 The Optical Society.

The compressed pulses have then been employed in a THz-TDS setup, as shown in Figure 2.8. The input beam (waist of 2.4 mm at $1/e^2$ of the intensity) has been separated by a 90:10 beam-splitter towards the pump and probe paths. The pump beam, which accounted for about $471 \mu\text{J}$ of energy ($\approx 26 \text{ GW}$ of peak power), has been focused into a 100- μm -thick-BBO crystal by means of an off-axis parabolic mirror (OPM1) with a focal length of 4 inches. The thickness of the BBO crystal has been chosen not to significantly alter the pump pulse duration (total crystal GDD of about 4.2 fs^2). The fundamental and second harmonic waves have been mixed together at the focal position in order to generate a two-color plasma filament in air (length of about 3 mm). A second off-axis mirror OPM2 with both focal length and diameter of 2 inches has been used to collimate the emitted ultra-broadband THz radiation, while a 1-mm-thick filter (Edmund long-pass 1.65 μm , a multilayer dielectric film on a silicon substrate) has been used to reflect the residual pump and second harmonic light. An appropriate selection of this filter for Yb-based systems becomes particularly critical since silicon plates, typically employed in THz setups utilizing Ti:Sapphire lasers, are not suitable to properly block light at wavelengths longer than 1000 nm (silicon bandgap at 1.14 eV $\approx 1087 \text{ nm}$). Moreover, it is important to notice that highly-reflective coatings are a stringent requirement for the envisioned high-average power operation of such kind of Yb-based THz sources, due to the fact that,

in such case, even a small fraction of optical absorption would thermally damage the filter. A set of OPMs of focal lengths equal to 3, 3, and 2 inches, respectively, has been used to direct the radiation towards the detection stage (see Figure 2.8). The ultra-broadband THz pulses have been coherently detected via the ABCD technique (Karpowicz et al., 2008) (see section 1.2.4 in the Introduction). To this end, the THz and the probe pulses have been focused together within a 1-mm-wide gap between two electrodes, to which a square bipolar voltage (up to 1.7 kV peak-to-peak, synchronized at half of the repetition rate of the laser) has been applied. The THz waveform has been acquired in a nitrogen-purged environment, by recording the THz-field-induced second-harmonic light in air with a photomultiplier tube (PMM01, Thorlabs) as a function of the relative delay between the THz and probe pulses (with a step of 5 fs).

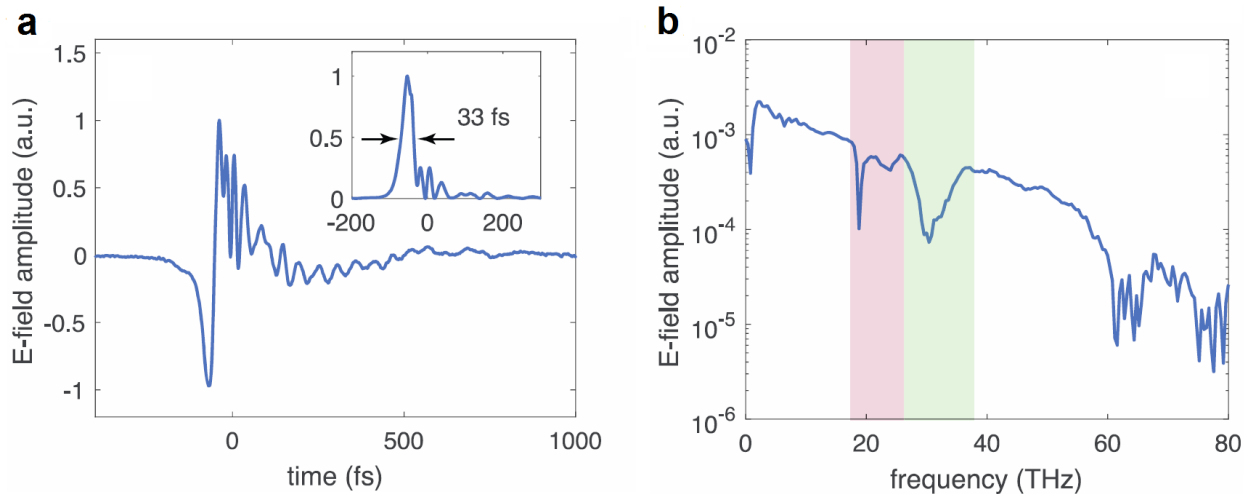


Figure 2.9 Electric-field waveform and spectrum of the ultrabroadband THz source

(a) Electric field waveform of the THz pulses retrieved via the ABCD method. Inset shows the intensity envelope featuring a main peak with a time duration of 33 fs FWHM. (b) Corresponding electric field spectrum calculated via FFT. The red and green shaded areas highlight the absorption bands coming from the spectral properties of the filter we have employed. Reprinted with permission from (Piccoli et al.) © 2019 The Optical Society.

As illustrated in Figure 2.9a, the THz waveform shows a prominent, nearly single-cycle oscillation with sub-50 fs temporal features. A peak THz electric field of 55 kV/cm was estimated by using the method described in section 1.2.4 of the Introduction. A maximum dynamic range, defined as the ratio between the maximum amplitude of the signal and the standard deviation of the noise level (Naftaly & Dudley, 2009), of 200 was measured at the maximum bias voltage of 1.7 kV, thus suggesting that this THz setup is good enough to be employed in THz-TDS spectroscopy measurements. The corresponding spectrum, numerically calculated via FFT, extends up to 60 THz (at the noise floor in logarithmic scale) (Figure 2.9b), thus effectively exploiting the frequency content of the compressed pump pulses ($1/18 \text{ fs} = 55.6 \text{ THz}$). The oscillation in time on the trailing edge of the THz pulse, and the corresponding absorption dips in the spectrum, come from the spectral

properties of the long-pass filter used to block the residual pump/second-harmonic light in our setup. To verify this, we employed two different Fourier-transform spectrometers (FTSs), in order to cover the entire THz emission band: a custom-made THz-FTS for the 2–12 THz region (*Blue Sky Spectroscopy*) and an IR-FTS (*Bruker*) for the region above 12 THz. As it is shown in Figure 2.10, the filter transmission in the range 1–30 THz, where most of the THz pulse energy is located, is below 50%. Moreover, the two absorption dips appearing in the THz pulse spectrum at around 18 and 30 THz (Figure 2.9b) are also clearly visible in the FTS spectral transmission of the filter. The first sharp feature (red shaded area in Figure 2.9b and Figure 2.10) is related to the two-phonon absorption of the silicon substrate (Deinzer & Strauch, 2004), while the second one (green shaded area in Figure 2.9b and Figure 2.10) is likely due to the THz response of the highly-reflective dielectric coating of the filter.

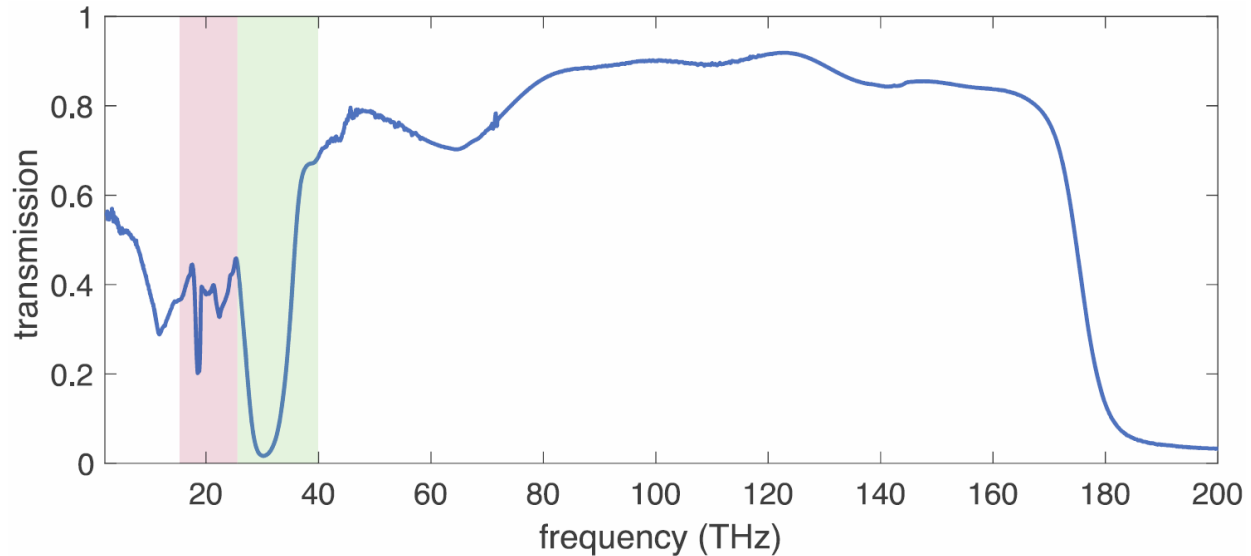


Figure 2.10 Transmission of the employed filter
Reprinted with permission from (Piccoli et al.) © 2019 The Optical Society.

This evidence underlines the importance for this type of Yb-based ultrabroadband THz source (and especially for high power applications) of a properly designed filter. In particular, the latter ideally needs to possess high and uniform transmission in the range 1–100 THz, as well as high reflectivity within the 800–1200 nm band. We also investigated the dependence of the THz emission on the input pump pulse energy. Figure 2.11a shows spectra (in logarithmic scale) recorded by varying the pump power in the range 100 - 471 μ J, while Figure 2.11b illustrates the peak electric field as a function of the input pulse energy. As it is possible to see from Figure 2.11b, the peak electric field shows a (quasi) quadratic dependence on the input pulse energy ($E_{\text{THz}} \propto \varepsilon_p^{2.15}$ through a least square fitting), which is consistent with the expected scaling for sub-mJ input energies, as reported in (Xie et al.,

2006). Finally, we measured the THz pulse energy by means of a pyroelectric detector (THZ-I-BNC, *Gentec-EO*). At the maximum incident pump energy of about $471 \mu\text{J}$, the generated THz pulses reached an energy value of about 35 nJ per pulse (average power of $210 \mu\text{W}$ at 6 kHz), corresponding to an energy conversion efficiency of 7.4×10^{-5} .

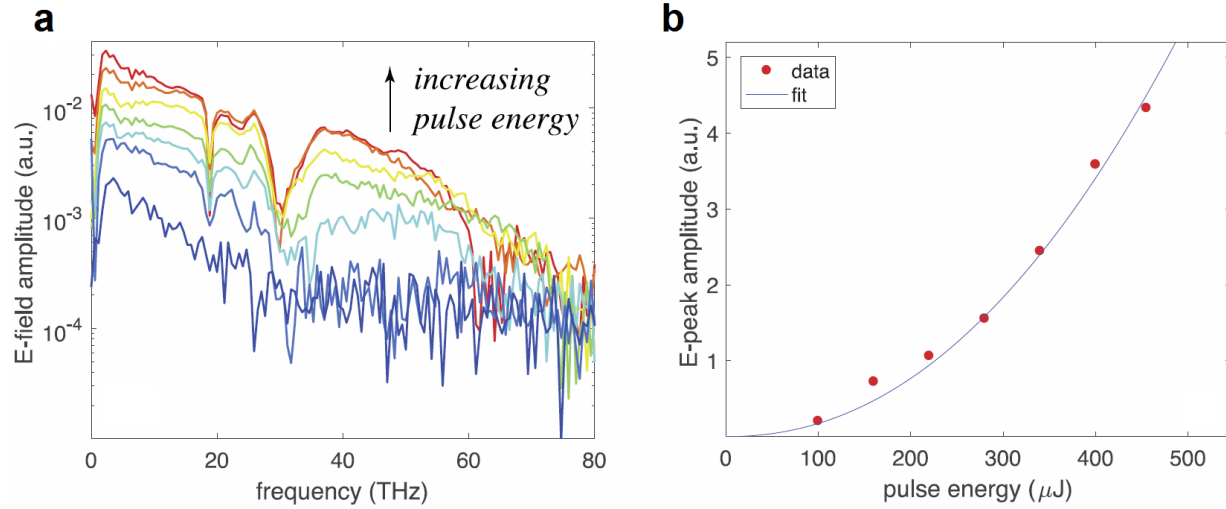


Figure 2.11 Ultrabroadband THz generation as a function of the input pulse energy
(a) Spectra and **(b)** peak electric fields recorded by varying the input pulse energy from 100 to $471 \mu\text{J}$. Reprinted with permission from (Piccoli et al.) © 2019 The Optical Society.

This broadband THz source can be employed in the future for nonlinear experiments at THz frequencies. For instance, a possible experiment concerns the use of this source for the nonlinear investigation of the strongly coupled system introduced in section 1.3.3 (composed of NA cavities and CdS nanocrystals), exploiting the fact that the developed source can provide intense pulses with a frequency content covering the hybridized resonance region, which is around 8 THz .

3 3D-PRINTED THZ RESONANT NANOCONES FOR OUT-OF-PLANE ULTRAFAST FIELD-DRIVEN PHOTOEMISSION

As already discussed in Chapter 1, the field enhancement of non-resonant metal nanotips has been extensively investigated for THz field-driven photoemission (Herink et al., 2014; Li & Jones, 2016), to achieve nanoscale-localized electron extraction together with local THz electric field amplitudes of a few MV/cm, which are required to observe measurable photocurrents. Concomitantly, other studies have exploited the higher field enhancement granted by planar resonant antennas with respect to non-resonant nanotips for a variety of driving optical frequencies, enabling electron photoemission at lower incident field amplitudes (Dombi et al., 2013; Iwaszczuk et al., 2014; Keathley et al., 2019; Kusa et al., 2015; Zhang et al., 2015). However, the close proximity of the substrate underneath the planar antennas limits the use of the emitted electron bunches for the most relevant applications.

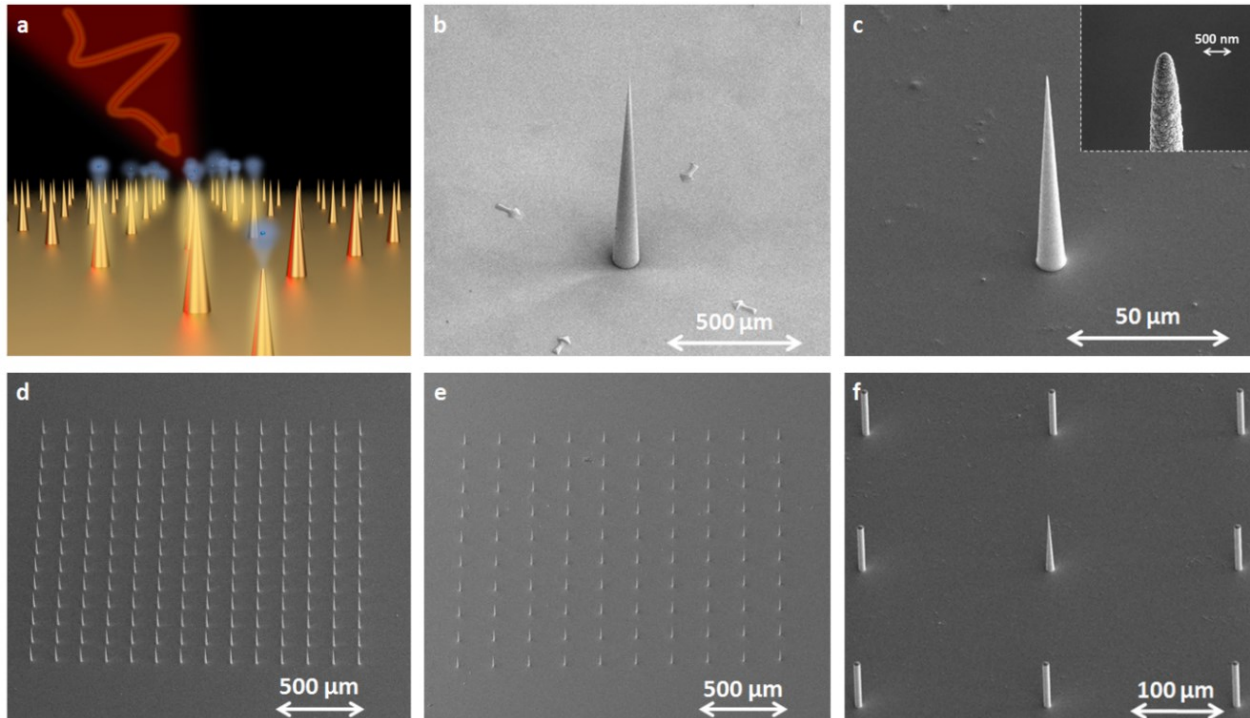


Figure 3.1 THz field-driven electron emission from vertical resonant NCs

(a) Illustration of THz field-driven electron photoemission from an array of monopolar resonant gold NCs. SEM pictures of the fabricated samples: (b) the 1-mm-high non-resonant nanotip, (c) the single RNC (note the image scale difference with respect to (b)), (d) the array of RNCs, (e) the array of cooperative RNCs, and (f) the single RNC in an array of cylinders. The apex detail of a fabricated RNC is shown in the inset of Figure 3.1c.

The discussion and the images of this chapter were adapted from:

A. Rovere, R. Piccoli, A. Bertoncini, Y.-G. Jeong, S. Payeur, F. Vidal, S.-H. Lee, J.-H. Seok, O-P. Kwon, R. Morandotti, C. Liberale, L. Razzari, (2020). 3D-Printed Photocathodes for Resonant, Terahertz-Field-Driven Ultrafast Electron Emission. (ArXiv: 2010.12098.)

In my thesis work, an innovative photocathode design for out-of-plane THz-driven photoemission is presented, enabled by the high reproducibility and precise control offered by advanced 3D printing lithography. In particular, out-of-plane gold resonant nanocones (RNCs) have been investigated, presenting a monopole resonance centered at 1 THz, due to the presence of a conductive gold surface at the bottom of the RNCs that acts as a mirror-image plane (sketch in Figure 3.1a). Moreover, the collective response of a RNC array can be finely tuned to achieve an even higher local THz field at the RNC apices. Such enhancement can be exploited to achieve a significant boost in field-driven electron emission in comparison with standard non-resonant nanotips. Finally, taking advantage of the geometrical freedom granted by 3D printing fabrication, we demonstrate that this “cooperative effect” can also be engineered to confine the field-driven photoemission to an individual RNC emitter. This isolated emission is achieved by positioning a single emitting RNC in an array of resonant and cooperative gold cylinders.

In this study, we have investigated different types of nanostructures and arrangements. We have first considered the case of a standard 1-mm-long nanotip (*non-resonant nanotip*, Figure 3.1b), which provides a field enhancement on its apex due to the lightening-rod effect (see section 1.4.1 of the Introduction). This reference structure has been compared to the newly-designed resonant structures: a *single RNC* (Figure 3.1c), featuring a monopolar resonance at 1 THz; an *array of RNCs* (Figure 3.1d), presenting a response similar to the one of the single RNC; an *array of cooperative RNCs* (Figure 3.1e) in which, by properly tuning the geometrical parameters, a surface lattice mode has been exploited to boost the THz field localization performance (see section 1.3.1 of the Introduction for further details on this cooperative effect); and finally, a *single RNC in an array of cylinders* (Figure 3.1f), which preserves the advantages of the cooperative effect while allowing photoemission from a single element of the array (the RNC). In the cases of the resonant structures, we have tailored their THz response by means of numerical simulations (COMSOL Multiphysics software) centering the monopole resonance at around 1 THz. The samples have then been fabricated by our collaborators at the King Abdullah University of Science and Technology (KAUST, Saudi Arabia) via a 3D printing technique based on two-photon absorption in a photopolymer (Nanoscribe). The fabricated RNCs feature an aspect ratio of 1/10 (base diameter/height) and an apex radius of curvature of 150 nm (inset of Figure 3.1c), determined by the maximum resolution of the 3D printing system. Subsequently, the entire area, measuring 1.8×1.8 mm², has been covered by the sputtering of a 200-nm-thick gold layer, thus coating the fabricated RNCs as well as their substrate (i.e., the surface whereon the RNCs are placed). The THz response of the arrays has been characterized by means of a THz-TDS setup. Afterwards, the photoemission characteristics of the different nanostructures have

been investigated and compared through both the analysis of gas-fluorescence induced by the emitted electrons, as well as via direct measurements of the photoemission current. Finally, a theoretical analysis based on the two-step model has been performed to corroborate the experimental evidences and calculate the electron energy distributions for the different nanoemitters.

3.1 Numerical design and experimental characterization of the THz response

The numerical simulations have been performed by means of COMSOL Multiphysics, a Finite Element Method (FEM)-based software. The model consists of different configurations of THz gold RNCs on a metallic surface, with a Drude gold permittivity defined as:

$$\varepsilon_{\text{Au}} = 1 - \frac{\omega_p^2}{\omega^2 + j\omega \frac{1}{\tau}} \quad (3.1)$$

where $\omega_p = 2\pi \cdot 2080 \text{ THz}$ is the plasma frequency of gold thin films, and $\tau = 18 \text{ fs}$, the carrier life time (Walther et al., 2007), while an air domain with $\varepsilon_{\text{air}} = 1$ has been considered on top of this system. The illuminating field is sent from the top of the model as a p-polarized plane monochromatic wave arriving at an incident angle of $\theta = 30^\circ$ with respect to the principal axis of the RNC (defined as the z axis, Figure 3.2a), within a frequency range between 0.1 and 10 THz. Note that only the z-component of the THz electric field ($E_z = E_0 \sin \theta$) contributes to excite the monopolar resonance of the RNC. Above and on the lateral sides of the overall geometrical model, so-called “perfectly matched layers” have been introduced to avoid reflection artifacts. To simulate an infinite array, periodic boundary conditions have been applied at the lateral sides of the model. The reflectance of the RNCs has been retrieved using the following formula $R = 1 - (P_{\text{abs}} + P_{\text{sca}})/P_0$, where P_0 is the incident power, while $P_{\text{abs}} = I_0 \sigma_{\text{abs}} = \int Q_h dV$ and $P_{\text{sca}} = I_0 \sigma_{\text{sca}} = \int W dS$ are the calculated absorbed and scattered powers from the RNC, respectively, I_0 being the intensity of the incident field, Q_h is the dissipated energy in the RNC volume and W is the Poynting flux outwards of the RNC. The geometrical parameters of the simulated nanostructures are reported in Table 3.1.

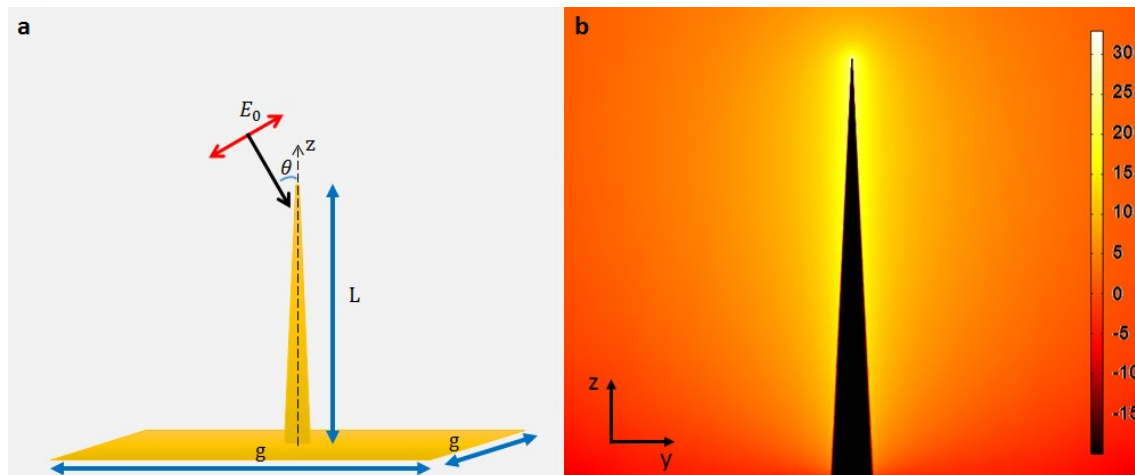


Figure 3.1 Model of a THz resonant RNC

(a) Sketch of the simulation model where the plane wave impinges on the gold RNC with an angle $\theta = 30^\circ$. (b) near-field distribution (in dB) in correspondence of the monopolar resonance frequency of the RNC.

The near-field distribution in correspondence of the monopolar resonance frequency of the RNC is shown in Figure 3.2b. In addition, it is possible to retrieve the field enhancement as $F = E_{\text{loc}}/E_0$, where E_{loc} is the local electric field calculated 1 nm above the apex of the RNC and E_0 is the incident electric field. For the case of a non-resonant metal nanotip, the field enhancement can be analytically evaluated considering a hemisphere-capped cylindrical rod of radius R (Podenok et al., 2006). In this case, the field enhancement is given by $F = \alpha(\lambda / R)$, with $\alpha = 0.06$ (Li & Jones, 2016) (Figure 3.3a).

Table 3.1 Geometrical parameters of the different simulated nanostructures

Parameter	Single RNC	Array of RNCs	Array of cooperative RNCs	RNC in an array of cylinders
L [μm]	81.6	120	81.6	Cone: 81.6 Cylinders: 66
R_b [μm]	4.08	6.87	4.08	Cone: 4.08 Cylinders: 3.3
g [μm]	-	140	200	200

L: nanocone length, R_b: bottom radius and g: periodicity

After the fabrication of the numerically-designed samples (performed by our collaborators), the THz spectral characterization of the arrays has been carried out in a reflection geometry using a THz-TDS setup. In particular, THz radiation has been generated by OR in a 500-μm-thick GaP crystal, pumped by our amplified Yb-laser, and detected via EOS in a second, 3-mm-thick GaP crystal. The measurements have been taken in a nitrogen-purged atmosphere and the corresponding reflectance spectra have been extracted considering the response of a bare gold surface as a reference.

Firstly, the case of a single resonant RNC on an infinite conductive gold surface has been considered. The calculated maximum value of the field enhancement is $F \approx 900$ in correspondence of the resonance frequency, when the height of the RNC is set at $\lambda_{\text{res}}/4 \approx 80 \mu\text{m}$ (Figure 3.3b). The numerically-calculated extinction cross-section of the single RNC also presents a monopolar resonance centered at around 1 THz, with a bandwidth (full-width at half maximum - FWHM) of 250 GHz. Note that the THz response of the single RNC could not be directly measured via far-field THz spectroscopy due to the very low extinction cross-section associated with an individual nanostructure.

The response of a periodic array of THz resonant RNCs has then been investigated. This design enables a coherent emission of electrons from multiple RNCs, returning a spatially-structured electron pattern that also leads to a higher overall current in comparison with a single emitter. The fabricated RNCs, separated by 140 μm , are in this case 120- μm -high, to compensate for the array induced-shift of the resonance position, providing a field enhancement factor of about 1850 at around 1 THz. The THz reflectance of the array is reported in Figure 3.3c (solid line) and shows a very good agreement with the numerical simulations (dashed line), both in terms of the resonance central frequency and bandwidth (about 115 GHz FWHM in the array case).

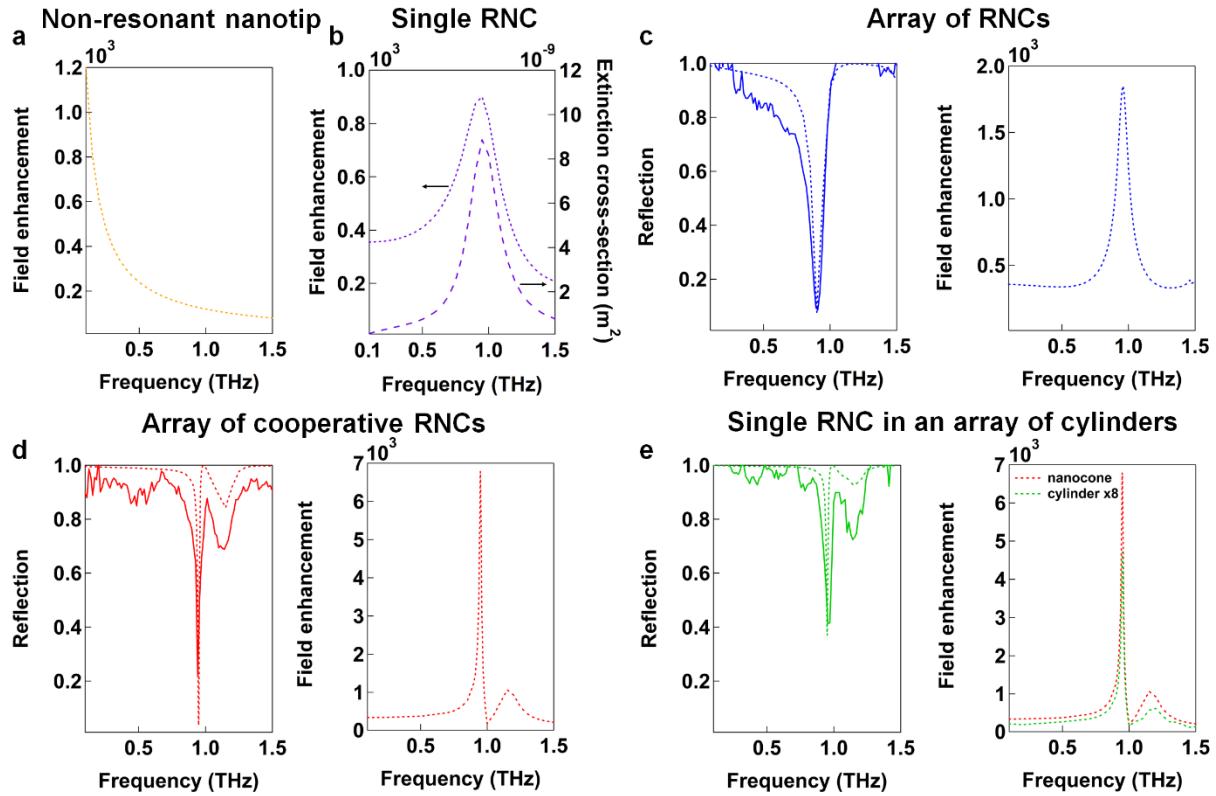


Figure 3.2 THz frequency responses of the investigated RNCs

Near- and far-field properties of the samples, as numerically calculated via COMSOL Multiphysics (or analytically retrieved for the case of the non-resonant tip field enhancement) (dotted lines), as well as measured reflectance of the arrays (solid lines). (a) Non-resonant nanotip, (b) Single RNC, (c) Array of RNCs and (d) Array of cooperative RNCs and (e) Single RNC in an array of cylinders. In the latter case, we simulated an array of cylinders with a radius of curvature at their edges equivalent to the one of the apex of the RNCs. As can be seen, the field enhancement at the top of the cylinders is about 10 times lower than the one of the central RNC (considered equivalent to the one retrieved for the array of cooperative RNCs).

As already mentioned in Chapter 1, the collective electromagnetic response of an array of resonant nanostructures can be further optimized via a proper harvesting of the radiation re-scattered by the various elements. This has been done for the array of cooperative RNCs, by tuning the periodicity of the array. In this sample, the fabricated RNCs are 81.6- μm -high, as in the case of the single RNC. Equation (1.23) reported in Chapter 1 can be used to fix the lattice resonance at 1 THz (i.e. $\lambda_0 =$

$300 \mu\text{m}$). Thus, by considering $n = 1$, $\theta = 30^\circ$, $\varphi = 0^\circ$, and the order $(l, m) = (-1, 0)$, it is possible to find a lattice periodicity of $g = 200 \mu\text{m}$. The cooperative effect in this array results in a significant boost in the local field enhancement, with a peak value of about 6800 and a narrower resonance bandwidth ($\sim 60 \text{ GHz FWHM}$ from the reflectance measurement, see Figure 3.3d) with respect to the non-cooperative array of RNCs. As mentioned, the benefit offered by this cooperative effect can also be maintained for the case of a single RNC surrounded by resonant cylinders, where the photoemission can thus be promoted in one element of the array (single RNC in an array of cylinders). In this sample, the height of the central RNC and the periodicity of the array are the same as the ones of the array of cooperative RNCs, while the height of the cylinders is reduced down to $66 \mu\text{m}$, to match their monopolar resonance to the one of the RNC. Figure 3.3e shows that the THz reflectance measurement on this sample presents features similar to those of the array of cooperative RNCs. The electric field enhancement value in proximity of the RNC apex is in this case assumed to be the same of the one extracted for the case of the cooperative RNC array, as suggested by numerical simulations conducted on a simplified model of a single RNC surrounded by 8 cylinders (Figure 3.4a and b, note that a larger number of cylinders would be extremely challenging to simulate from a computational point of view). As can be seen from Figure 3.3e, the maximum field enhancement at the RNC apex is 11 times higher than the one reached on the cylinders. As a consequence, since field-driven photoemission is highly nonlinear with respect to the THz local electric field (as described by the FN Equation (1.32) presented in Chapter 1), this hybrid geometry guarantees an individual electron emission “hot spot”.

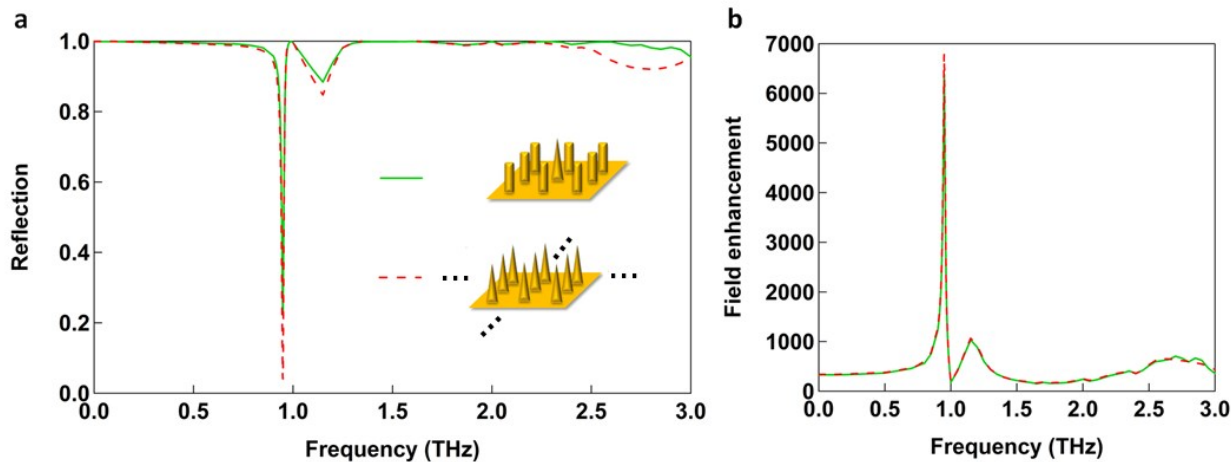


Figure 3.3 Numerical simulation of a NC surrounded by just 8 cylinders
Comparison between the simulated (a) reflection spectra and (b) field enhancements for a RNC surrounded by 8 cylinders (green curve) and the array of cooperative RNCs (red curve).

3.2 Study of the THz field-driven photoemission

In this section, a study of the ultrafast tunneling process from the THz gold RNCs is presented. First, we show the experimental results of the fluorescence analysis, which has allowed us to compare the photoemission properties of the different emitters and evaluate their effective time-domain field enhancement. Subsequently, direct measurements of the photoemission current are also reported via an in-house built setup. The observed current trends have shown the expected threshold-like behaviour, thus qualitatively confirming the tunneling regime of the process. Finally, a two-step analytical model has been used to calculate the kinetic energy distributions of the photoemitted electron bunches from each sample.

3.2.1 Experimental setup for the fluorescence measurement

To get access to a simple optical evaluation of the THz-field-induced electron emission characteristics of the fabricated samples, we have characterized the fluorescence signal emitted by argon gas atoms surrounding the metallic nanostructures under a controlled static pressure, following a procedure first introduced in (Iwaszczuk et al., 2014). In brief, the gas atoms are excited by the impact with the extracted electrons, leading to a fluorescence emission due to the radiative de-excitation of the Ar atoms, which can be directly described by the FN equation (see paragraph 1.4.1 of the Introduction), thus returning the key photoemission characteristics. A scheme of the experimental setup used for this measurement is shown in Figure 3.5a.

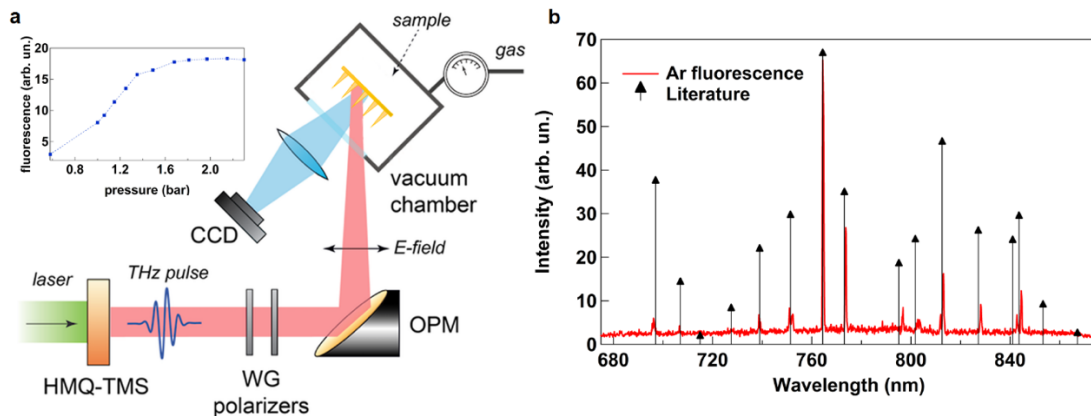


Figure 3.4 Experimental setup for the fluorescence measurements

(a) Schematic of the setup used for the fluorescence measurements. WG polarizers – wire grid polarizers; OPM – 90 deg off-axis parabolic mirror. The measured fluorescence intensity as a function of the Ar pressure is reported in the inset. (b) Spectrum of argon fluorescence emission under THz excitation acquired by using a monochromator, compared with the argon emission lines taken from literature (Saloman, 2010).

Broadband (0.1 – 3.0 THz) THz pulses with a maximum peak electric field of 180 kV/cm have been generated via OR in the HMQ-TMS nonlinear organic crystal pumped by our amplified Yb laser (Rovere et al., 2018). The sample under investigation has been placed in a sealed chamber filled with

argon gas. First, keeping the incident THz field to the maximum, we have acquired the fluorescence intensity as a function of the argon pressure in the chamber. As it is shown in the inset in Figure 3.5a, the measured fluorescence intensity typically shows a plateau for an argon pressure level higher than 1.4 bar. We have also acquired the fluorescence emission spectrum by means of an Oriel monochromator (calibrated with an argon lamp) in the wavelength range comprised between 680-870 nm. The measured spectrum matches well with the argon emission lines from literature (Figure 3.5b) (Saloman, 2010). In the subsequent experiments, two wire-grid polarizers have been used in series on the beam path to vary the incident THz field amplitude while maintaining a p-polarization at their output. The THz field has been sent through a z-cut quartz window onto the sample with an incident angle of 30 degrees with respect to the principal axis of the RNCs. The effective incident electric field on the sample E_{exc} can thus be retrieved considering the transmission of the chamber window and the electric field projection on the main axis of the RNCs (note that $\max_t(E_{\text{exc}}) = 80$ kV/cm for the maximum input peak electric field in our experiments).

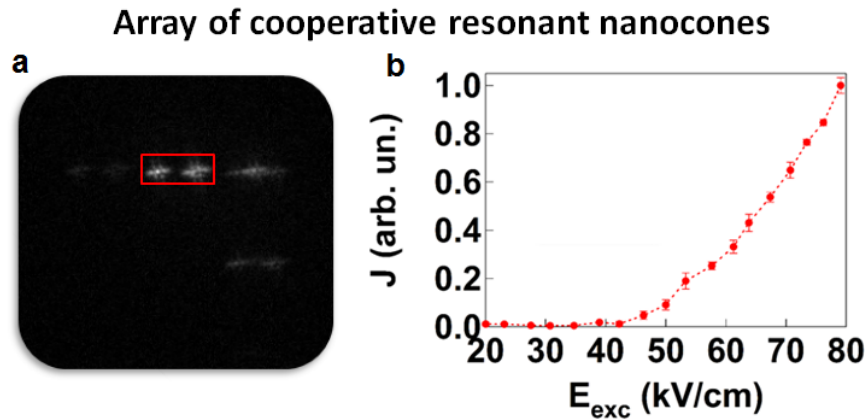


Figure 3.5 Fluorescence measurements

(a) Example of a fluorescence image acquired with the CCD camera for the case of the array of cooperative RNCs. The origin of the double-spot feature observed for all the structures is the reflection of the emitted fluorescence off the gold-coated bottom plane. (b) Experimental data of the measured argon fluorescence from the same sample as a function of E_{exc} .

The fluorescence light has been collected by a telescope (with a magnification of about 2, imaging the apexes of the nanostructures) and acquired with a CCD camera, allowing a relative evaluation of the local fluorescence intensity for each individual nanostructure in a sample (Figure 3.6a). Each image is normalized to the background (i.e., image taken without fluorescence) and then the fluorescence intensity is integrated in a selected area for the considered emitter. Thus, the integrated intensity values have been plotted as a function of the incident THz field, obtaining a trend (see an example in Figure 3.6b for the case of the array of cooperative RNCs) that can be well described by the FN equation, as we will see in the next section.

3.2.2 Analysis of the fluorescence measurements

It is important to note that the sharp resonance of the metallic RNCs acts as a frequency bandpass filter for the illuminating broadband THz radiation. Therefore, the observed photoemission process arises from a trade-off between the absolute field enhancement peak value at the resonance frequency and the portion of the THz excitation spectrum effectively filling the RNC resonance bandwidth. A reference parameter can be defined, i.e., the time-domain THz peak electric field enhancement:

$$\beta_{\text{calc}} = \max_t(E_{\text{local}}) / \max_t(E_{\text{exc}}) \quad (3.2)$$

where E_{local} is the time-domain local electric field evaluated 1 nm above the nanostructure apex. Thus, β_{calc} implicitly takes into account the spectral overlap between the incident THz pulses and the resonance of the investigated samples.

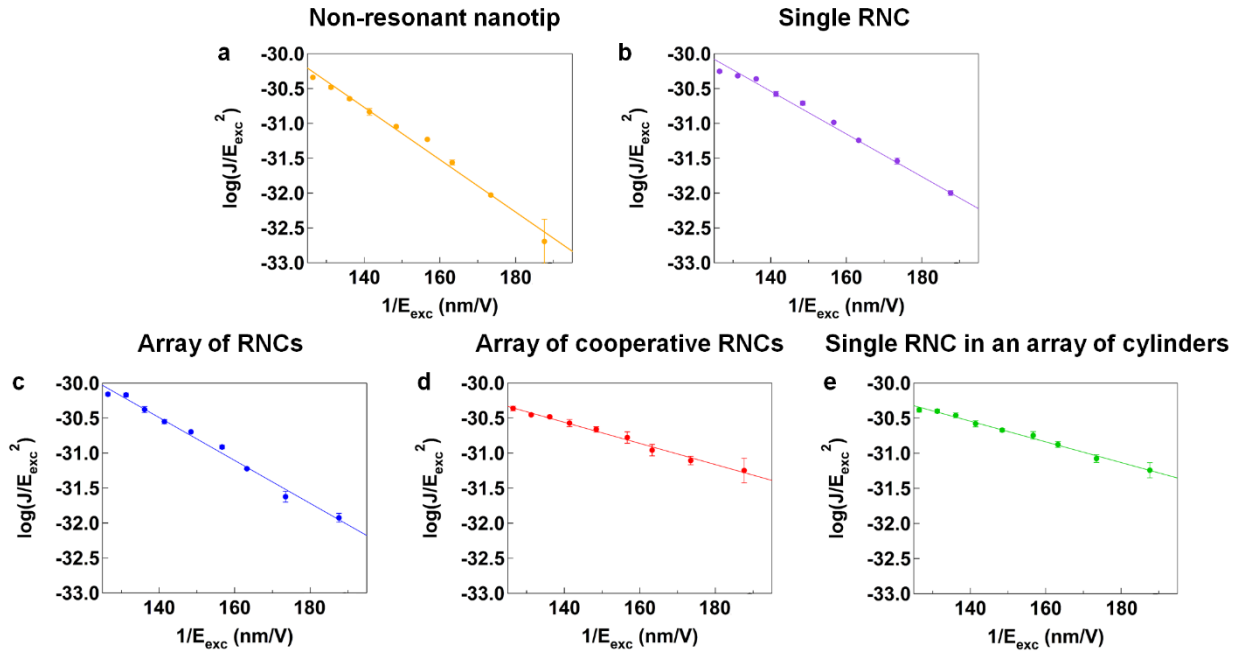


Figure 3.6 FN plots of the fluorescence measurements

(a-e) Experimental data (dots) of the measured argon fluorescence and linear fit using Equation 3.3 (solid lines) for the various samples. From the slope of the fit, it is possible to retrieve an experimental estimation of the time-domain field enhancement for each sample.

Noteworthy, it is possible to retrieve the experimental values of such time-domain THz-peak electric field enhancement for our samples from the fluorescence measurements. As already discussed in the Introduction, the FN equation (Equation (1.33)) can be conveniently rewritten as:

$$\log\left(\frac{J}{E_{\text{exc}}^2}\right) = C_1 + C_2/E_{\text{exc}} \quad (3.3)$$

where $C_1 = \log\left(\frac{\phi}{a\beta^2}\right)$ and $C_2 = -\frac{b\phi^{3/2}}{\beta}$. In this way, it is possible to represent the experimental data in a linear plot. All our fluorescence measurements exhibit a high degree of linearity, as can be seen in Figure 3.7, confirming the field-driven nature of the photoemission process. Using this representation, we can extract, by means of a simple linear fit, the slope factor C_2 for each sample, which is directly related to the time-domain field enhancement factor, β_{exp} :

$$\beta_{\text{exp}} = -\frac{b\phi^{3/2}}{C_2} \quad (3.4)$$

The values of β_{exp} retrieved by fitting the data from the fluorescence experiments with Equation (3.4) represent an effective way to compare the photoemission performance of the different nanostructures. In this comparison, we have considered an effective work function of $\phi = 0.78 \pm 0.03$ eV for all the gold nanostructures. Such value has been retrieved by fitting the experimental data for the non-resonant nanotip while fixing $\beta = 128$ since, as explained above, a well-established analytical formula exists for this case (Podenok et al., 2006). As already observed by (Iwaszczuk et al., 2014) for evaporated gold antennas, the obtained value is lower than the work function typically reported for bulk gold (~ 5 eV) (Lide, 2008). This difference has been attributed to i) impurities and adsorbates from air locally deposited on the photoemission area, which can lower ϕ of a metal under field-driven electron tunneling(Duke & Alferieff, 1967); ii) the intrinsic roughness of the evaporated gold surface, with nanometer-scale features at the apex, which may lead to an increased local field enhancement. Indeed, an underestimation of β would result in a decreased retrieved value for ϕ , due to the dependence of the slope factor in Equation 3.4 on both these two parameters. Table 3.2 summarizes the time-domain field enhancement values β_{exp} we have obtained from the luminescence experiments. They are in good agreement with the corresponding enhancement factors β_{calc} returned by the numerical simulations (Equation 3.2, also reported in Table 3.2). As one can see, the β values related to the resonant NCs are higher than the one of the non-resonant nanotip, indicating a more efficient electron photoemission. Additionally, the cooperative effect in an array geometry leads to a final ~ 2.5 fold increase in the time-domain field enhancement factor with respect to the non-resonant case ($\beta_{\text{exp}} > 300$ for the cooperative case, meaning that the local field at the RNC apex reaches values greater than 24 MV/cm in our experimental conditions). Finally, a similar

photoemission boost is confirmed for the case of the array of cooperative RNCs and the single RNC in the array of cooperative cylinders.

Table 3.2 Results from the analysis fluorescence measurement

Parameter	Non-resonant nanotip	Single RNC	Array of RNCs	Array of cooperative RNCs	RNC in an array of cylinders
$C_2 (\times 10^7)$	(-3.7 ± 0.2)	(-3.1 ± 0.1)	(-3.1 ± 0.1)	(-1.51 ± 0.06)	(-1.47 ± 0.05)
β_{exp}	128 (analytical)	153 ± 10	153 ± 10	314 ± 21	322 ± 21
β_{calc}	128 (analytical)	204	209	344	344

Slope factors C_2 for each sample, retrieved from the fit of the fluorescence experiments presented in Figure 3.7 using Equation 3.4. The corresponding field enhancement values extracted from the measurements (β_{exp}) and the calculations (β_{calc}). The case of the non-resonant tip has been used as a reference to estimate the gold work function ($\phi = 0.78 \pm 0.03$ eV), by fixing β to the value retrieved analytically.

3.2.3 Direct measurement of the photoemission current

Proof-of-principle electrical measurements have also been performed, to provide a direct evidence of electron emission. For this, a solid-state electrometer (*Keithley 610C*) has been employed. The sample under investigation has been placed in a chamber under ultra-high vacuum ($\sim 10^{-6}$ mbar) and a copper foil (anode, 2×2 cm 2 in size) connected to the electrometer has been used to collect the emitted electrons (see sketch in Figure 3.8a). The measured photocurrents produced by the array of RNCs and the array of cooperative RNCs (Figure 3.8b) as a function of E_{exc} show the characteristic threshold-like behavior similar to the one observed in the fluorescence experiments, thus confirming the field-driven process. The current starts to be observable for $E_{\text{exc}} \sim 50$ kV/cm and reaches a maximum at 80 kV/cm of about 1.5 pA for the array of RNCs and 1.15 pA for the cooperative array, corresponding to 6 fC and 4.6 fC per pulse (3.75×10^4 and 2.87×10^4 electrons per pulse), respectively.

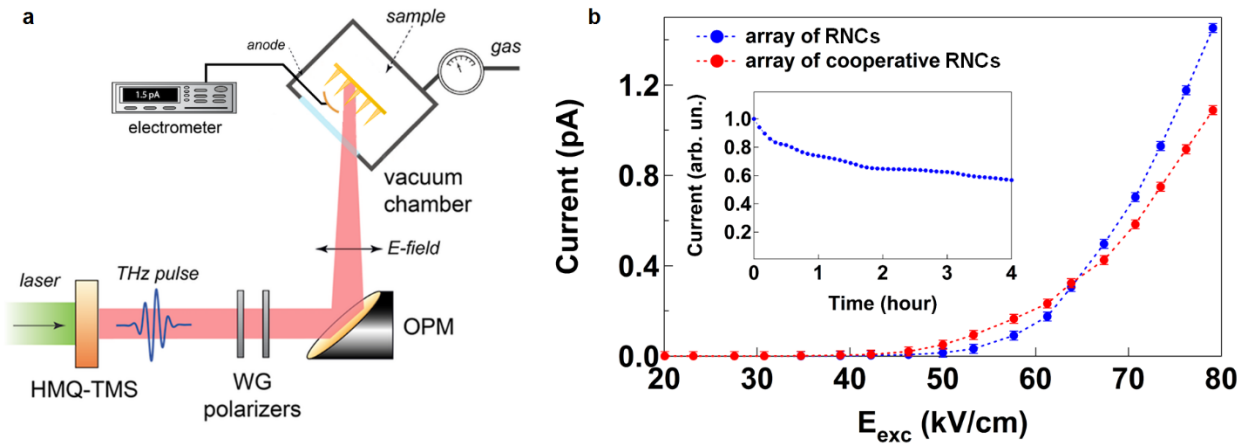


Figure 3.7 Photocurrent measurements

(a) Schematic of the experimental setup used to measure the photocurrent. (b) Current as a function of the incident THz peak electric field for the two RNC array samples. Inset: current trend for the array of RNCs under a 4-hour-long exposure to the highest THz field.

It is important to underline that the extracted electron bunches in our setup experience a considerable transversal spread, due to space charge effects, during the propagation from the photocathode to the anode. A simple numerical model has been developed to study the propagation of the extracted electrons between the RNC apex and the collecting copper foil, placed at $d = 1.5$ cm from the emitter (in order not to block the incoming THz radiation in our basic home-built setup). In this model, N_e electrons with kinetic energy ε , are randomly generated in an initial area of 150×150 nm 2 . The electron trajectories are evaluated numerically by solving the 3D equation of motion, taking into account the Coulomb interaction between all the electrons. It has been assumed that all electrons had an initial axial velocity corresponding to the estimated cut-off of the energy distributions for the

two RNC arrays (reported in Figure 3.13 in the next section) and no transverse velocity. To reduce the calculation time when the number of electrons is large, quasi-particles comprising N electrons, with mass $M_N = Nm_e$ and of charge, $Q_N = Nq_e$ have been used, where m_e and q_e are the mass and charge of a single electron, respectively. The results have been found to be similar to the case where all electrons are considered individually. In order to retrieve the number of extracted electrons, N_e for both the array of RNCs and the array of cooperative RNCs, we have integrated the emission current in time calculated by means of the FN equation (as the one reported in Figure 3.12 in the next section), obtaining the number of extracted electrons per pulse in both cases. In particular, for the case of the array of RNCs, the estimated number of electrons ($N_e = 3.45 \times 10^4$) results very close to the measured one ($N_e = 3.75 \times 10^4$). For the case of the cooperative array, the number of extracted electron is estimated to be > 6 times higher ($N_e = 2.22 \times 10^5$).

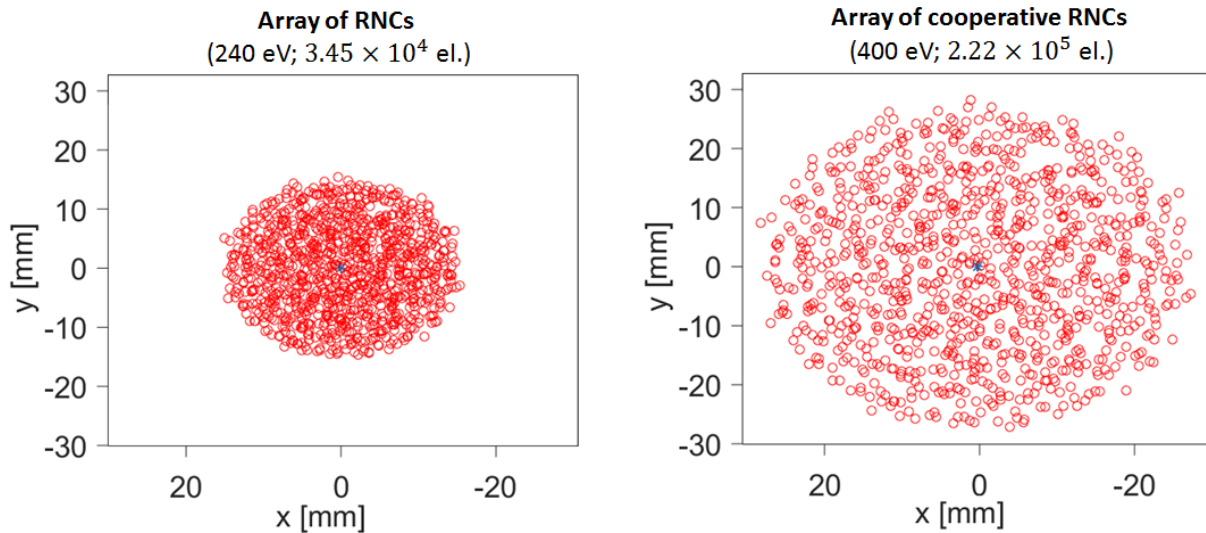


Figure 3.8 Numerical evaluation of the spatial spread of the electron bunch

Numerical evaluation of the spatial spread of the electron bunch after a propagation of 1.5 cm, considering a number of electrons per pulse for the two arrays estimated via the FN current and the electron kinetic cut-off energies calculated in the previous section. The central blue point in each figure represents the initial position of the electrons.

As it is possible to observe from Figure 3.9, the electron bunches emitted from the array of cooperative RNCs experience a considerable spatial spread (up to 5-6 cm in diameter) after a propagation of 1.5 cm, which is larger than the case of the array of RNCs (up to 3 cm in diameter), due to the higher number of extracted electrons. Thus, the geometrical constraints of this basic detection scheme hinder the complete collection of the total photoemitted current. This likely has affected the measurement of the cooperative RNC array even more severely than the one of the non-cooperative array, considering that the RNCs of the former sample are endowed with a larger β value and are then expected to deliver a higher number of electrons per THz pulse, resulting in a larger

spread of the emitted electrons, as estimated by our calculations. Furthermore, the two RNC arrays also have a different number of RNCs per unit area (~ 2 times smaller in the case of the cooperative RNC array), which clearly affects the overall measured current in the two cases. These facts prevent the use of such electrical characterization for a quantitative comparison between the arrays. Moreover, the photocurrent measured using this in-house developed setup has resulted to be too weak to return consistent datasets for the samples with a single nanostructure emitter.

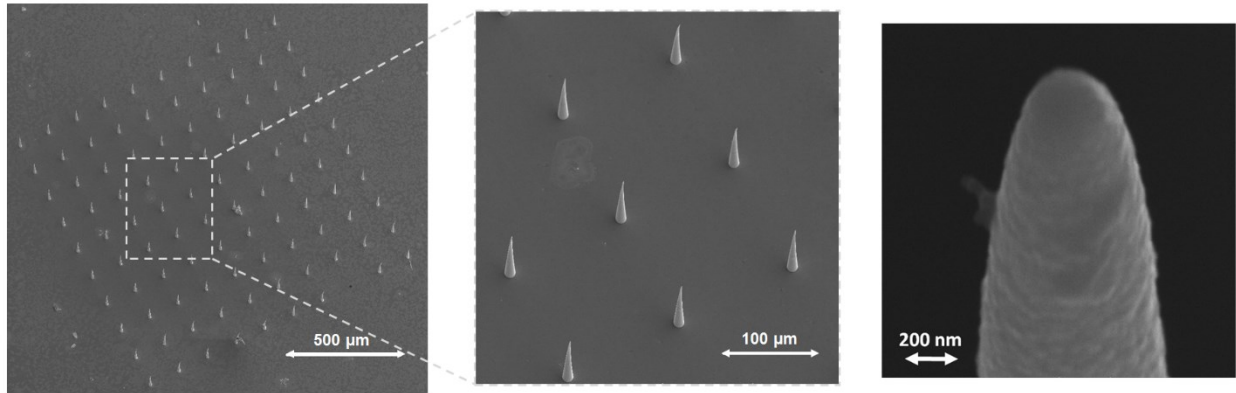


Figure 3.9 SEM images of the array of RNCs taken after the characterization experiments SEM images of the array of RNCs at the end of the set of measurements. The RNCs show a good structural stability even after an exposure of ~ 50 million THz pulses.

To test the robustness of our nanostructures as electron emitters, the emitted photocurrent from the array of RNCs has also been acquired for long exposure times and under the highest incident THz field provided by our source. As one can see in the inset of Figure 3.10, the gold RNCs are still functional after several hours of continuous THz illumination. The presence of a slow decay in time of the photocurrent (decrease of $\sim 40\%$ after 4 hours of exposure), besides a certain degree of degradation of the emitter surface, is also related to a residual charge accumulation on the anode that was observed in our in-house built setup. The structural stability of the RNCs has been further confirmed by an SEM inspection of the nanostructures after a prolonged THz exposure (about 50 million THz pulses). As seen in Figure 3.10, the RNC gold surface does not show signs of critical damage, especially in proximity of the RNC apex, which is typically the most sensitive area in these experiments (Li & Jones, 2016).

3.3 Electron energy distributions calculated via the two-step analytical model

The time-domain field enhancement value not only drives the tunneling process but also determines the subsequent electron acceleration and the resulting electron energy spectrum, an important parameter for the practical applications of the generated electron pulses. The overall process can be described via a two-step analytical model (see section 1.4.1 of the Introduction) that allows to retrieve the kinetic energy of the accelerated electrons, which considers: i) the electron extraction from the nanostructure through tunneling; ii) the subsequent electron acceleration by the THz electric field in proximity of the apex. Analytic forms for both the time-dependent tunneling current density, $j(t)$, and the enhanced THz field, $E(z, t)$, have been used to estimate the energy distributions of the photoemitted electrons for a 1-dimensional motion along the nanostructure principal axis, z.

The enhanced THz field at the nanostructure apex is given by the product between its spatial and time varying components, $E(z, t) = E_{\text{local}}(t) \times E(z)$, both retrieved from the numerical simulations. In particular, the spatial dependence of the THz electric field has been obtained by estimating the field decay as a function of the distance from the nanotip along the z-axis, as shown in Figure 3.11a. The spatial decay of the near-field can be then fitted with a double exponential function:

$$E(z) = y_0 + A_1 e^{-(z-z_0)/k_1} + A_2 e^{-(z-z_0)/k_2} \quad (3.5)$$

The fitting parameters for the case of the array of cooperative RNCs are reported in Figure 3.11a.

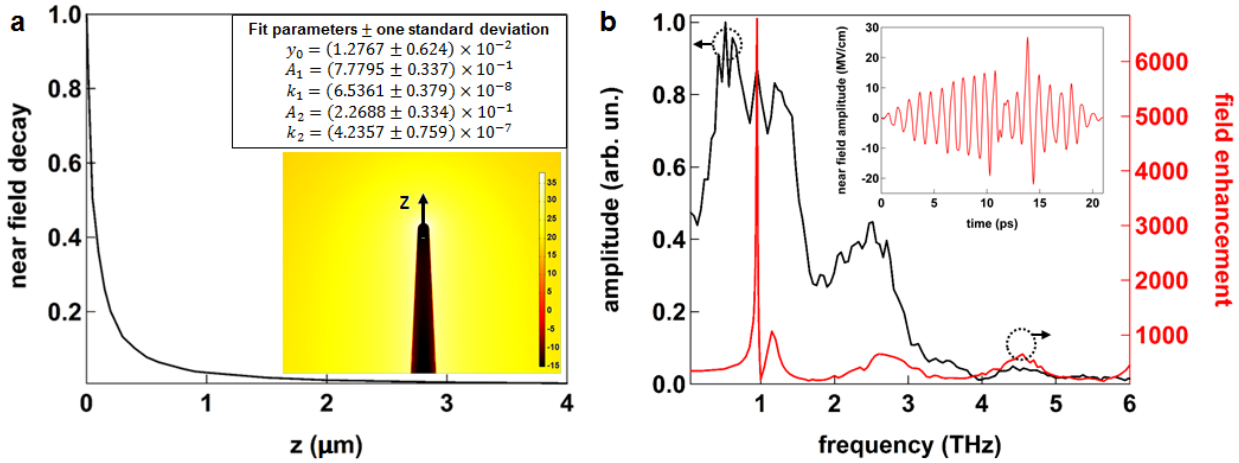


Figure 3.10 Spatial and temporal dependence of the THz near-field
(a) Spatial dependence of the enhanced THz near-field in proximity of the RNC apex, retrieved by the numerical simulations for the case of the array of cooperative RNCs. **(b)** Spectral overlap between the incident THz spectrum of the high-field THz source (Black) and the frequency field enhancement calculated at the RNC apex (Keathley et al.). The enhanced near-field in the time-domain for the case of the array of cooperative RNCs is shown in the inset.

At the same time, the time-domain dependence of the enhanced THz near-field can be estimated by considering the filtering effect of the narrow monopolar resonance of the RNCs in the frequency-domain on the impinging THz source spectrum (Figure 3.11b), which results in a multi-cycle THz waveform in the time-domain (inset in Figure 3.11b). The latter has been analytically interpolated by means of the following Fourier series:

$$E_{\text{local}}(t) = E_0 \sum_n [a_n \sin\left(\frac{\pi n t}{T}\right) + b_n \cos\left(\frac{\pi n t}{T}\right)] \quad (3.6)$$

Where E_0 is the peak amplitude of the THz near-field, a_n and b_n are the n^{th} Fourier coefficients of the expansion. Note that the time-domain field enhancement factor considered in the previous sections, β_{calc} , has been extracted from the ratio between the peak amplitude of the THz near-field (Equation (3.6)) and the peak amplitude of the incident THz field on the RNCs.

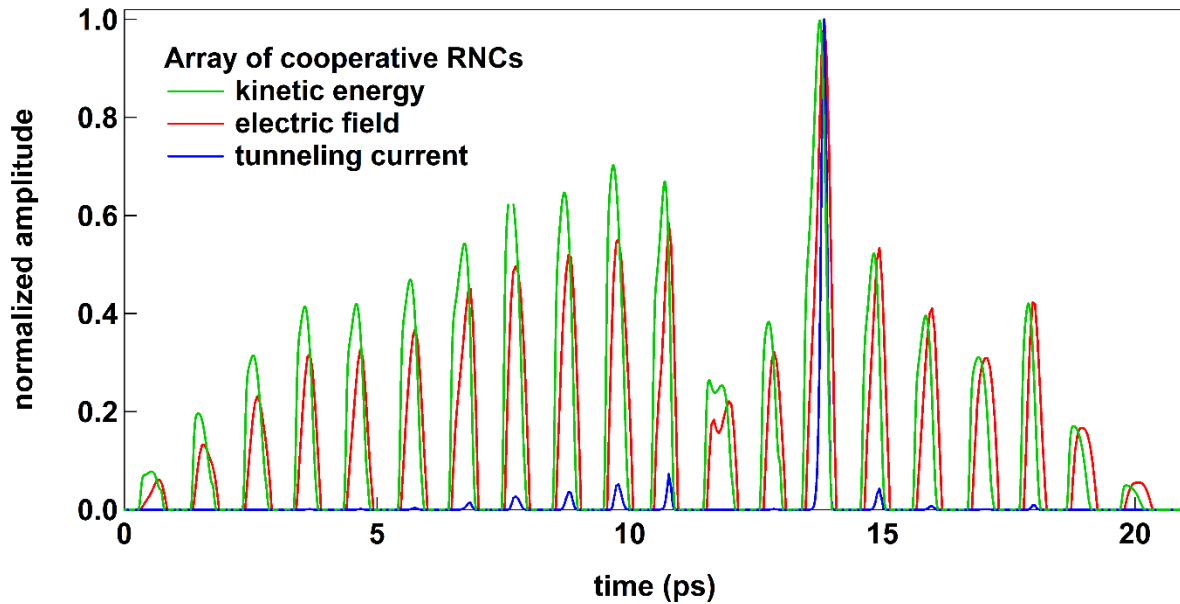


Figure 3.11 Time dependence of near field quantities

Time dependence of final kinetic energy (Hafez et al.), electron tunneling current density (blue) and THz electric field (Keathley et al.) for the case of the array of cooperative RNCs.

In order to simulate the acceleration of electrons emitted under the excitation of the THz pulse, we have solved the non-relativistic equation of motion for a free electron in an external electric field, by using a 4th order Runge-Kutta numerical method:

$$\begin{cases} m\ddot{z}(t) = -eE(z, t) \\ \dot{z}(t_0) = 0; z(t_0) = 0 \end{cases} \quad (3.7)$$

From the evaluated single-particle trajectory, we obtain the final kinetic energy (after the acceleration region, green curve in Figure 3.12) for a hypothetic electron extracted at the time t_B :

$$\varepsilon_K(t_B) = \frac{m[\dot{z}_B(t_\infty)]^2}{2} \quad (3.8)$$

In the quasi-static approximation, the time-dependent tunneling current density, at time t , is given by the FN theory:

$$J(t) = \Theta[E_0(t)] \frac{a|E_0(t)|^2}{\phi} \exp\left(\frac{-b\phi^{3/2}}{|E_{z=0}(t)|}\right) \quad (3.9)$$

where $\Theta[E_0(t)]$ is the Heaviside step function introduced to restrict electron emission to the polarity of the electric field for which the electric force drives the electron away from the metal surface. The retrieved final kinetic energy (Hafez et al.), tunneling current density (blue), and the driving THz electric field (Keathley et al.) for the case of the cooperative array of RNCs are reported in Figure 3.12. As one can see, the electron photoemission occurs predominantly in correspondence to the most intense half optical cycle of the THz near-field waveform, which gives rise to the emission of an electron bunch with a duration of a few-hundred fs.

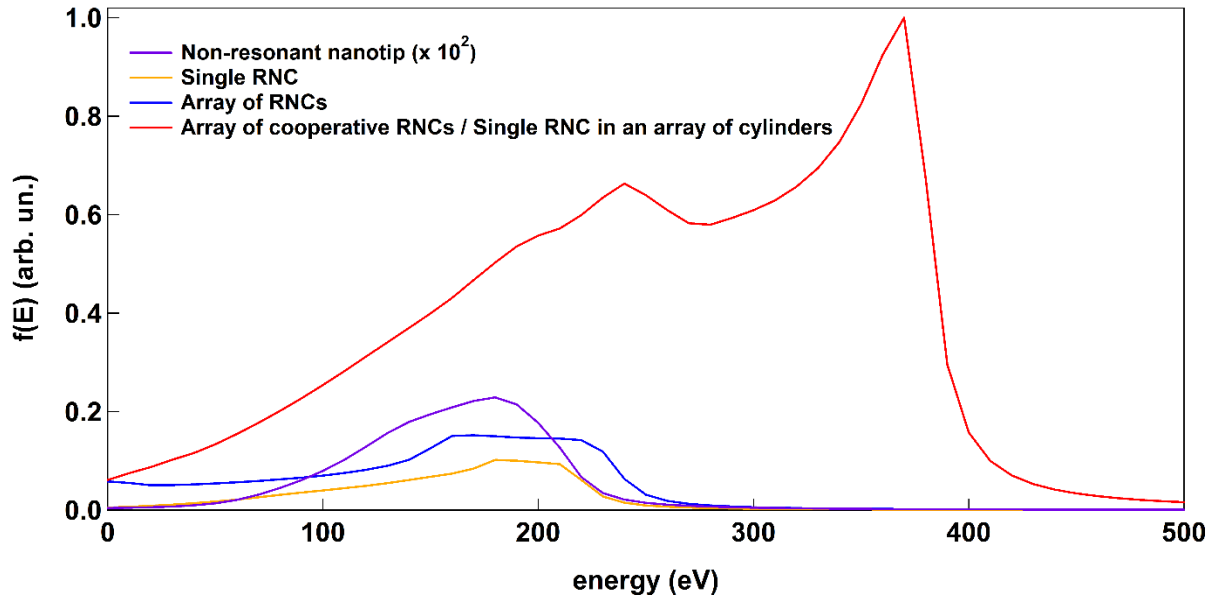


Figure 3.12 Energy distributions of the photoemitted electrons from the different nanostructures

Finally, the electron energy distributions $f(\varepsilon)$ has been obtained by weighting the final kinetic energies with the instantaneous tunneling probability, $P(t_B)$:

$$f(\varepsilon) \propto \int dt_B P(t_B) \frac{\Gamma/\pi}{[\varepsilon - \varepsilon_K(t_B)]^2 + \Gamma^2} \quad (3.10)$$

where $P(t_B) = \exp\left(\frac{-4\sqrt{2m}\phi^{3/2}}{3\hbar e|E_0(t)|}\right)$ and $\Gamma = 10$ eV is the energy resolution of the retrieved energy spectra. Figure 3.13 shows the energy distribution of the photoemitted electrons for the various samples tested in the conditions of our experiments. According to this model, the cooperative effect is predicted to result in an almost two-fold increase in the electron energy cut-off with respect to the case of a non-resonant tip, with significant energy values extending beyond 400 eV for just 80 kV/cm of effective incident electric field, E_{exc} .

4 CONCLUSIONS AND FUTURE PERSPECTIVES

Yb-lasers already represent the new frontier of ultrafast laser technology, but their exploitation for the efficient generation of intense THz pulses has not been fully explored yet, due to the fact that the most common, highly-nonlinear OR crystals do not offer a good phase-matching condition at 1030 nm. As a possible solution to this, in this thesis work two different strategies to generate high-field THz radiation by means of an amplified Yb-laser have been investigated.

First, it has been shown that the recently-synthesized organic crystal HMQ-TMS can be effectively employed for the simple, collinear generation of high-peak-electric-field THz pulses using a commercially-available amplified Yb laser as the optical pump. THz peak electric fields greater than 200 kV/cm have been obtained with a spectral emission extending beyond 3 THz, and a THz energy per pulse of 1.1 μ J, corresponding to a valuable energy conversion efficiency of 0.26%. The latter value is comparable to the efficiency obtained in a previous work, where intense THz pulses were generated by pumping LiNbO_3 with a Yb laser in a non-collinear scheme (Vicario et al., 2014). Moreover, this THz source has been employed in a proof-of-principle nonlinear Z-scan experiment, inducing a significant saturation of THz absorption in an n-doped InGaAs thin film, thus showing the potential of this novel source configuration for the exploration of THz nonlinear effects in condensed matter.

Furthermore, a Yb laser-based THz-TDS system providing an extremely broad bandwidth (up to 60 THz) with peak electric fields higher than 50 kV/cm has been introduced as a proof-of-principle, by employing an HCF pulse-compression stage and a two-color plasma generation scheme. Ultra-broadband generation has been achieved thanks to the HCF-based pulse compression, which has allowed us to convert 170-fs-long pulses emitted by our Yb laser amplifier into 18-fs-long pulses (10-fold compression). This method opens the route to the exploitation of the many advantages of Yb laser technology (including the availability of very high average powers / high repetition rates) for ultra-broadband THz generation. Regarding this, for the adoption of high-repetition-rate (MHz) Yb systems as pumping stations, high-frequency switching voltages at the kV-level would be required to perform the necessary ABCD detection, which is extremely challenging to implement. A promising alternative that can be explored in future works is represented by a recently developed THz detection technique, named solid-state-biased coherent detection (SSBCD) (Tomasino et al., 2017). Indeed, SSBCD can be biased with only 10 V and can thus easily operate at MHz switching frequencies, showing a great potential to be combined with the generation method proposed in this work for the development of the next-generation of ultra-broadband, high-field, high-repetition-rate THz TDS

systems. The developed ultrabroadband THz source can also be utilized for the exploration of nonlinear effects in our phonon strong coupling system. Indeed, the phonon resonance hybridization described in section 1.3.3 takes place at around 8 THz, so that the developed source can be used to intensely pump the system, entering the nonlinear strong coupling regime (Bishop et al., 2008) where the phonon resonance hybridization would be modified according to the pump intensity, an uncharted territory for the phonon response modification in nanosystems.

Finally, the intense THz pulses generated by the HMQ-TMS source have been used to explore a strong-field phenomenon at THz frequencies, in combination with the local field enhancement provided by THz resonant nanostructures. In particular, a novel photocathode design strategy for ultrafast THz-field-driven photoemission has been proposed, exploiting the advantages of high-resolution 3D printing. This approach allows achieving out-of-plane electron emission and acceleration employing broadband table-top THz sources with peak electric fields at the 100 kV/cm level. Using numerical modeling, THz far-field characterization, and the analysis of electron-induced argon gas fluorescence, we have shown the advantage offered by RNCs featuring a monopolar resonance at THz frequencies with respect to traditional non-resonant tips. Moreover, we have introduced a further degree of optimization, by tailoring the collective response of the RNCs when arranged in an array geometry. A significant boost of the nano-localized THz peak electric field of a factor of 2.5 when compared to the standard non-resonant case has been demonstrated for the cooperative nanostructures. This means that the peak electric field of the THz driver can be equivalently reduced by the same factor to obtain the same electron extraction/acceleration. Remarkably, such boost can also be obtained for electron emission from an individual nanostructure, as we have shown for the case of an RNC in an array of resonant cylinders. We also built a custom setup to perform proof-of-principle photocurrent measurements that corroborated the fluorescence intensity characterization, confirming the field-driven nature of the electron emission. A maximum current of 1.5 pA was recorded, corresponding to 3.75×10^4 electrons per THz pulse, showing that the developed photocathodes can deliver high brightness electron bunches of interest for, e.g., time-resolved electron diffraction experiments. The fabricated nanostructures exhibited a good structural resistance after several hours of exposure to intense THz fields. While our strategy was demonstrated for the case of broadband THz sources, the use of a narrowband source would allow the full exploitation of the sharp RNC resonance. Narrowband THz sources at the kV/cm peak electric field level can be built with femtosecond lasers of a few μJ energy (Krause et al., 2011). Such configuration could enable a novel class of THz-driven ultrafast electron sources with unprecedentedly high repetition rates (MHz level). We thus envision that the combination of THz source technology advances with rationally-designed 3D-printed

resonant nanostructures may find applications in the development of next-generation nano-localized and coherent ultrafast electron sources.

5 BIBLIOGRAPHY

- Abb, M., Wang, Y., Papasimakis, N., Groot, C. H., & Muskens, O. L. (2013). Surface-enhanced infrared spectroscopy using metal oxide plasmonic antenna arrays. *Nano Lett.*, *14*, 346-352.
- Agio, M., & Alù, A. (2013). *Optical antennas*. Cambridge University Press.
- Aglieri, V., Jin, X., Rovere, A., Piccoli, R., Caraffini, D., Tuccio, S., De Angelis, F., Morandotti, R., Macaluso, R., Toma, A., & Razzari, L. (2020). Improving nanoscale terahertz field localization by means of sharply tapered resonant nanoantennas. *Nanophotonics*, *9*, 683-690.
- Aspnes, D. E., & Studna, A. A. (1983). Dielectric functions and optical parameters of Si, Ge, GaP, GaAs, GaSb, InP, InAs, and InSb from 1.5 to 6.0 eV. *Phys. Rev. B*, *27*, 985-1009.
- Bazylewski, P., Ezugwu, S., & Fanchini, G. (2017). A review of three-dimensional scanning near-field optical microscopy (3D-SNOM) and its applications in nanoscale light management. *Appl. Sci.*, *7*, 973.
- Benicewicz, P. K., Roberts, J. P., & Taylor, A. J. (1994). Scaling of terahertz radiation from large-aperture biased photoconductors. *J. Opt. Soc. Am. B*, *11*, 2533-2546.
- Biagioni, P., Huang, J. S., & Hecht, B. (2012). Nanoantennas for visible and infrared radiataion. *Rep. Prog. Phys.*, *75*, 024402.
- Bishop, L. S., Chow, J. M., Koch, J., Houck, A. A., Devoret, M. H., Thuneberg, E., Girvin, S. M., & Schoelkopf, R. J. (2008). Nonlinear response of the vacuum Rabi resonance. *nature Phys.*, *5*, 105-109.
- Black, J. R. (1969). Electromigration - a brief survey and some recent results. *IEEE Transactions on Electron Devices*, *16*, 338-347.
- Blanchard, F., Razzari, L., Bandulet, H. C., Sharma, G., Morandotti, R., Kieffer, J. C., Ozaki, T., Reid, M., Tiedje, H. F., Haugen, H. K., & Hegmann, F. A. (2007). Generation of $1.5 \mu\text{J}$ single-cycle terahertz pulses by optical rectification from a large aperture ZnTe crystal. *Opt. Express*, *15*, 13212.
- Blanchard, F., Sharma, G., Razzari, L., Ropagnol, X., Bandulet, H.-C., Vidal, F., Morandotti, R., Kieffer, j. C., Ozaki, T., Tiedje, H., Haugen, H., Reid, M., & Hegmann, F. A. (2011). Generation of intense terahertz radiation via optical methods. *IEEE Journal of Selected Topics in Quantum Electronics*, *17*, 5-16.

- Blanchard, F., Sharma, G., Ropagnol, X., Razzari, L., Morandotti, R., & Ozaki, T. (2009). Improved terahertz two-color plasma sources pumped by high intensity laser beam. *Opt. Express*, 17, 6044-6052.
- Bormann, R., Gulde, M., Weismann, A., Yalunin, S. V., & Ropers, C. (2010). Tip-enhanced strong-field photoemission. *Phys. Rev. Lett.*, 105, 147601.
- Boyd, R. (2008). *Nonlinear Optics (3rd ed.)*. San Diego, USA: Elsevier Service.
- Brunner, F. D., Lee, S.-H., Kwon, O.-P., & Feurer, T. (2014). THz generation by optical rectification of near-infrared laser pulses in the organic nonlinear optical crystal HMQ-TMS. *Opt. Mater. Express*, 4, 1586– 1592.
- Carbone, F., Kwon, O.-H., & Zewail, A. H. (2009). Dynamics of chemical bonding mapped by energy-resolved 4D electron microscopy. *Science*, 325, 181.
- Cardin, V., Thiré, N., Beaulieu, S., Wanie, V., Légaré, F., & Schmidt, B. E. (2015). 0.42 TW 2-cycle pulses at 1.8 μm via hollow-core fiber compression. *Appl. Phys. Lett.*, 107, 181101.
- Caverley, A. (1959). Heating by electron bombardment. *Nature*, 184, 690-693.
- Chai, X., Ropagnol, X., Raeis-Zadeh, S. M., Reid, M., Safavi-Naeini, S., & Ozaki, T. (2018). Subcycle terahertz nonlinear optics. *Phys. Rev. Lett.*, 121, 143901.
- Clerici, M., Peccianti, M., Schmidt, B. E., Caspani, L., Shalaby, M., Giguère, M., Lotti, A., Couairon, A., Légaré, F., Ozaki, T., Faccio, D., & Morandotti, R. (2013). Wavelength scaling of terahertz generation by gas ionization. *Phys. Rev. Lett.*, 110, 253901.
- Cook, D. J., & Hochstrasser, R. M. (2000). Intense terahertz pulses by four-wave rectification in air. *Opt. Letters*, 25, 1210-1212.
- Corkum, P. (1993). Plasma perspective on strong field multiphoton ionization. *Phys. Rev. Lett.*, 71, 1994-1997.
- Cubukcu, E., Yu, N., Smythe, E. J., Diehl, L., Crozier, K. B., & Capasso, F. (2008). Plasmonic laser antennas and related devices. *IEEE J. Sel. Top. Quant.*, 14, 1448-1461.
- Deinzer, G., & Strauch, D. (2004). Two-phonon infrared absorption spectra of germanium and silicon calculated from first principles. *Phys. Rev. B*, 69, 045205.
- Dexheimer, S. L. (2007). *Terahertz spectroscopy: principles and applications*. CRC Press.

- Dombi, P., Hörl, A., Rácz, P., Márton, I., Trügler, A., Krenn, J. R., & Hohenester, U. (2013). Ultrafast strong-field photoemission from plasmonic nanoparticles. *Nano Lett.*, *13*, 674-678.
- Dressel, M., & Gruner, G. (2003). *Electrodynamics of solids*. (C. U. Press, Ed.)
- Duke, C. B., & Alferieff, M. E. (1967). Field emission through atoms adsorbed on a metal surface. *J. Chem. Phys.*, *46*, 923.
- Echternkamp, K. E., Herink, G., Yalunin, S. V., Rademann, K., Schäfer, S., & Ropers, C. (2016). Strong-field photoemission in nanotip near-fields: from quiver to sub-cycle electron dynamics. *Appl. Phys B*, *122*, 80.
- Einstein, A. (1905). Über einen die Erzeugung und Verwandlung des Lichtes betreffenden heuristischen Gesichtspunkt. *Annalen der physik*, *322*, 132-148.
- Ermushev, A. V., Mchedlishvili, B. V., Olešnikov, V. A., & Petukhov, A. V. (1993). Surface enhancement of local optical fields and the lightning-rod effect. *Quantum Electron.*, *23*, 435–440.
- Fan, K., Hwang, H. Y., Liu, M., Strikwerda, A. C., Sternbach, A., Zhang, J., Zhao, X., Zhang, X., Nelson, K. A., & Averitt, R. D. (2013). Nonlinear terahertz metamaterials via field-enhanced carrier dynamics in GaAs. *Phys. Rev. Lett.*, *110*, 217404-217405.
- Fleisher, S., Zhou, Y., Field, R. W., & Nelson, K. A. (2011). Molecular orientation and alignment by intense single-cycle THz pulses. *Phys. Rev. Lett.*, *107*, 163603.
- Fletcher, J. R. (2002). Distortion and uncertainty in chirped pulse THz spectrometers. *Opt. Express*, *10*, 1425-1430.
- Fowler, R. H., & Nordheim, L. (1929). Electron Emission in Intense Electric Fields. *P. Roy. Soc. A.*, *119*, 173-181.
- Franken, P., Hill, A. E., Peters, C., & Weinreich, G. (1961). Generation of optical harmonics. *Phys. Rev. Lett.*, *7*, 118, 119.
- Fukunaga, K., & Picollo, M. (2010). Terahertz spectroscopy applied to the analysis of artists' materials. *Applied Physics A*, *100*, 591-597.
- Giorgianni, F., Chiadroni, E., Rovere, A., Cestelli-Guidi, M., Perucchi, A., Bellaveglia, M., Castellano, M., Di Giovenale, D., Di Pirro, G., Ferrario, M., Pompili, R., Vaccarezza, C., Villa, F., Cianchi, A., Mostacci, A., Petrarca, M., Brahlek, M., Koirala, N., Oh, S., & Lupi, S. (2016). Strong nonlinear terahertz response induced by Dirac surface states in Bi₂Se₃ topological insulator. *Nature Commun.*, *7*, 11421.

- Grischkowsky, D. R., Keiding, S., Exter, M., & Fattinger, C. (1990). Far-infrared time-domain spectroscopy with terahertz beams of dielectrics and semiconductors. *J. Opt. Soc. Am. B*, *7*, 2006-2015.
- Hädrich, S., Klenke, A., Hoffmann, A., Eidam, T., Gottschall, T., Rothhardt, J., Limpert, J., & Tünnermann, A. (2013). Nonlinear compression to sub-30-fs, 0.5 mJ pulses at 135 W of average power. *Opt. Lett.*, *38*, 3866-3869.
- Hafez, H. A., Chai, X., Ibrahim, A., Mondal, S., Féralchou, D., Ropagnol, X., & Ozaki, T. (2016). Intense terahertz radiation and their applications. *J. Opt.*, *18*, 093004.
- Hafez, H. A., Kovalev, S., Deinert, J.-C., Mics, Z., Green, B., Awari, N., Chen, M., Germanskiy, S., Lehnert, U., Teichert, J., Wang, Z., Tielrooij, K. J., Liu, Z., Chen, Z., Narita, A., Müllen, K., Bonn, M., Gensch, M., & Turchinovich, D. (2018). Extremely efficient terahertz high harmonic generation in graphene by hot Dirac fermions. *Nature*, *561*, 507-511.
- Hamster, H., Sullivan, A., Gordon, S., White, W., & Falcone, R. W. (1993). Subpicosecond, electromagnetic pulses from intense laser-plasma interaction. *Phys. Rev. Lett.*, *71*, 2725-2728.
- Hauri, C. P., Ruchert, C., Vicario, C., & Ardana, F. (2011). Strong-field single-cycle THz pulses generated in an Organic Crystal. *Appl. Phys. Lett.*, *99*, 161116.
- Hebling, J., Almási, G., Kozma, I. Z., & Kuhl, J. (2002). Velocity matching by pulse front tilting for large-area THz-pulse generation. *Opt. Express*, *10*, 1161-1166.
- Hecht, E. (2014). *Optics*. Berlin: de Gruyter.
- Herink, G., Solli, D. R., Gulde, M., & Ropers, C. (2012). Field-driven photoemission from nanostructures quenches the quiver motion. *Nature*, *483*, 190-193.
- Herink, G., Wimmer, L., & Ropers, C. (2014). Field emission at terahertz frequencies AC-tunneling and ultrafast carrier dynamics. *New Journal of Physics*, *16*, 123005.
- Hirori, H., Doi, A., Blanchard, F., & Tanaka, K. (2011). Single-cycle terahertz pulses with amplitudes exceeding 1 MV/cm generated by optical rectification in LiNbO₃. *Appl. Phys. Lett.*, *98*, 091106.
- Hoener, B. S., Kirchner, S. R., Heiderscheit, T. S., Collins, S. S., Chang, W.-S., Link, S., & Landes, C. F. (2018). Plasmonic sensing and control of single-nanoparticle electrochemistry. *Chem.*, *4*, 1560-1585.
- Hoffmann, M. C., H. J., Hwang, H. Y., Yeh, K. L., & Nelson, K. A. (2009). Impact ionization in InSb probed by terahertz pump-terahertz probe spectroscopy. *Phys. Rev. B*, *79*, 161201.

- Hommelhoff, P., Sortais, Y., Aghajani-Talesh, A., & Kasevich, M. A. (2006). Field emission tip as a nanometer source of free electron femtosecond pulses. *Phys. Rev. Lett.*, *96*, 077401.
- Hwang, H. Y., Brandt, N. C., Farhat, H., Hsu, A. L., Kong, J., & Nelson, K. A. (2013). Nonlinear THz conductivity dynamics in P-type CVD-grown graphene. *J. Phys. Chem. B*, *117*, 15819–15824.
- Ismail, N., Kores, C. C., Geskus, D., & Pollnau, M. (2016). Fabry-Pérot resonator: spectral line shapes, generic and related airy distributions, linewidths, finesse, and performance at low or frequency dependent reflectivity. *Opt. Express*, *16*, 16366.
- Irmer, G., Monecke, J., & Verma, P. (2004). Encyclopedia of nanoscience and nanotechnology (Vol. 4). California: American Scientific Publisher.
- Iwaszczuk, K., Zalkovskij, M., Strikwerda, A. C., & Jepsen, P. U. (2014). Nitrogen plasma formation through terahertz-induced ultrafast electron field emission. *Optica*, *2*, 116-123.
- Jeong, J.-H., Kang, B.-J., Kim, J.-S., Jazbinsek, M., Lee, S.-H., Lee, S.-C., Baek, I. H., Yun, H., Kim, J., Lee, Y. S., Lee, J. H., Kim, J. H., Rotermund, F., & Kwon, O.-P. (2013). High-power broadband organic THz generator. *Sci. Rep.*, *3*, 3200.
- Jeong, Y.-G., Paul, M. J., Kim, S.-H., Yee, K.-J., Kim, D.-S., & Lee, Y.-S. (2013). Large enhancement of nonlinear terahertz absorption in intrinsic GaAs by plasmonic nanoantennas. *Appl. Phys. Lett.*, *103*, 171109.
- Jeong, Y.-G., Piccoli, R., Ferachou, D., Cardin, V., Chini, M., Hädrich, S., Limpert, J., Morandotti, R., Légaré, F., Schmidt, B. E., & Razzari, L. (2018). Direct compression of 170-fs 50-cycle pulses down to 1.5 cycles with 70% transmission. *Sci. Rep.*, *8*, 11794.
- Jin, X., Cerea, A., Messina, G. C., Rovere, A., Piccoli, R., Donato, F. D., Palazon, F., Perucchi, A., Di Pietro, P., Morandotti, R., Lupi, S., De Angelis, F., Prato, M., Toma, A., & Razzari, L. (2018). Reshaping the phonon energy landscape of nanocrystals inside a terahertz plasmonic nanocavity. *Nat. Commun.*, *9*, 763.
- John, F. F., Schuklin, B., Huang, F., Gary, D., Barat, R., Oliveira, F., & Zimdars, D. (2005). THz imaging and sensing for security applications - explosives, weapons and drugs. *Semicond. Sci. Tech.*, *20*, S266.
- Kampfrath, T., Tanaka, K., & Nelson, K. A. (2013). Resonant and nonresonant control over matter and light by intense terahertz transients. *Nat. Photon.*, *7*, 680-690.

- Kang, J. H., Kim, D. S., & Park, Q.-H. (2009). Local capacitor model for plasmonic electric field enhancement. *Phys. Rev. Lett.*, *102*, 093906.
- Karpowicz, N., Dai, J., Lu, X., Chen, Y., Yamaguchi, M., Zhao, H., & Zhang, X.-C. (2008). Coherent heterodyne time-domain spectrometry covering the entire "terahertz gap". *Appl. Phys. Lett.*, *92*, 011131.
- Kauranen, M., & Zayats, A. V. (2012). Nonlinear plasmonics. *Nat. Photon.*, *6*, 737-748.
- Keathley, P. D., Putnam, W. P., Vasireddy, P., Hobbs, R. G., Yang, Y., Berggren, K. K., & Kärtner, F. X. (2019). Vanishing carrier-envelope-phase-sensitive response in optical-field photoemission from plasmonic nanoantennas. *Nature Phys.*, *15*, 1128-1133.
- Keldysh, L. V. (1965). Ionization in the field of a strong electromagnetic wave. *Sov. Phys. JETP*, *20*, 1307-1314.
- Kim, K. Y., Glownia, J. H., Taylor, A. J., & Rodriguez, G. (2007). Terahertz emission from ultrafast ionizing air in symmetry-broken laser fields. *Opt. Express*, *15*, 4577-4584.
- Koechner, W. (2006). *Solid-State Laser Engineering*. Springer.
- Koenderink, A. F. (2010). On the use of Purcell factors for plasmon antenna. *Opt. Lett.*, *35*, 4208.
- Krause, J., Wagner, M., Winnerl, S., Helm, M., & Stehr, D. (2011). Tunable narrowband THz pulse generation in scalable large area photoconductive antennas. *Opt. Express*, *19*, 19114-19121.
- Kravets, V. G., Kabashin, A. V., Barnes, W. L., & Grigorenko, A. N. (2018). Plasmonic surface lattice resonances: a review of properties and applications. *Chem. Rev.*, *118*, 5912-5951.
- Kusa, F., Echternkamp, K. E., Herink, G., Ropers, C., & Ashihara, S. (2015). Optical field emission from resonant gold nanorods driven by femtosecond mid-infrared pulses. *AIP Adv.*, *5*, 077138.
- Kwon, O. P., Kwon, S.-J., Jazbinsek, M., Brunner, F. D., Seo, J.-I., Hunziker, C., Schneider, A., Yun, H., Lee, Y. S., & Günter, P. (2008). Organic phenolic configurationally locked polyene single crystals for electro-optic and terahertz wave applications. *Adv. Funct. Mat.*, *18*, 3242-3250.
- Lange, C., Maag, T., Hohenleutner, M., Baierl, S., Schubert, O., Edwards, E., Bougeard, D., Woltersdorf, G., Huber, R. (2014). Extremely nonperturbative nonlinearities in GaAs driven by atomically strong terahertz field in golden metamaterials. *Phys. Rev. Lett.*, *113*, 227401.
- Law, S., Yu, L., Rosenberg, A., & Wasserman, D. (2013). All-semiconductor plasmonic nanoantennas for infrared sensing. *Nano Lett.*, *13*, 4569-4574.

- Leitenstorfer, A., Hunsche, S., Shah, J., & Nuss, M. C. (1999). Detectors and sources for ultrabroadband electro-optic sampling: experiment and theory. *Appl. Phys. Lett.*, *74*, 1516.
- Li, S., & Jones, R. R. (2016). High-energy electron emission from metallic nano-tips driven by intense single-cycle terahertz pulses. *Nat. Commun.*, *7*, 13405.
- Lide, D. R. (2008). *CRC handbook of chemistry and physics*. London, UK: CRC Press.
- Lu, J., Hwang, H. Y., Li, X., Lee, S.-H., Kwon, O.-P., & Nelson, K. A. (2015). Tunable multi-cycle THz generation in organic crystal HMQ-TMS. *Opt. Express*, *23*, 22723-22729.
- Maier, S. A. (2007). *Plasmonics: fundamentals and applications*. Berlin, NY: Springer US.
- Maiman, T. H. (1960). Stimulated optical radiation in ruby. *Nature*, *187*, 493–494.
- Malerba, M., Alabastri, A., Miele, E., Zilio, P., Patrini, M., Bajoni, D., Messina, G. C., Dipalo, M., Toma, A., Proietti Zaccaria, R., & Angelis, F. D. (2015). 3D vertical nanostructures for enhanced infrared plasmonics. *Sci. Rep.*, *5*, 16436.
- Matsubara, E., Nagai, M., & Ashida, M. (2012). Ultrabroadband coherent electric field from far infrared to 200 THz using air plasma induced by 10 fs pulses. *Appl. Phys. Lett.*, *101*, 011105.
- Maxwell, J. C. (1865). A dynamical theory of the electromagnetic field. *Philos. Trans. Royal Soc.*, *155*, 459–512.
- Mittleman, D. M. (2017). Perspective: Terahertz science and technology. *J. Appl. Phys.*, *122*, 230901.
- Naftaly, M., & Dudley, R. (2009). Methodologies for determining the dynamic ranges and signal-to-noise ratios of terahertz time-domain spectrometers. *Opt. Lett.*, *34*, 1213–1215.
- Nahata, A., & Heinz, T. F. (1998). Detection of freely propagating terahertz radiation by use of optical second-harmonic generation. *Opt. Lett.*, *23*, 67-69.
- Neubrech, F., Huck, C., Weber, K., Pucci, A., & Giessen, H. (2017). Surface-enhanced infrared spectroscopy using resonant nanoantennas. *Chem. Rev.*, *117*, 5110-5145.
- Nisoli, M., Silvestri, S. D., & Svelto, O. (1996). Generation of high energy 10 fs pulses by a new pulse compression technique. *Appl. Phys. Lett.*, *68*, 2793.
- Novotny, L. (2007). Effective wavelength scaling for optical antennas. *Phys. Rev. Lett.*, *98*, 266802.
- Oh, T. I., You, Y. S., Jhajj, N., Rosenthal, E. W., Milchberg, H. M., & Kim, K. Y. (2013). Intense terahertz generation in two-color laser filamentation: energy scaling with terawatt laser systems. *New J. Phys.*, *15*, 075002.

- Park, H. S., Baskin, J. S., Barwick, B., Kwon, O.-H., & Zewail, A. H. (2009). 4D ultrafast electron microscopy: Imaging of atomic motions, acoustic resonances, and moiré fringe dynamics. *Ultramicroscopy*, 110, 7-19.
- Piccoli, R., Rovere, A., Jeong, Y.-G., Jia, Y., Zanotto, L., Légaré, F., Schmidt, B. E., Morandotti, R., & Razzari, L. (2019). Extremely broadband terahertz generation via pulse compression of an Ytterbium laser amplifier. *Opt. Express*, 27, 32659-32665.
- Pilot, R., Signorini, R., Durante, C., Orian, L., Bhamidipati, M., & Fabris, L. (2019). A review on surface-enhanced Raman scattering. *Biosensors*, 9, 57.
- Podenok, S., Sveningsson, M., Hansen, K., & Campbell, E. E. (2006). Electric field enhancement factors around a metallic, end-capped cylinder. *Nano*, 1, 87-93.
- Rayleigh, L. (1907). On the dynamical theory of gratings. *Proc. R. Soc. Lond. A.*, 79, 399-416.
- Razzari, L., Su, F. H., Sharma, G., Blanchard, F., Ayesheshim, A., Bandulet, H.-C., Morandotti, R., Kieffer, J. C., Ozaki, T., Reid, M., & Hegmann, F. A. (2009). Nonlinear ultrafast modulation of the optical absorption of intense few-cycle terahertz pulses in n-doped semiconductors. *Phys. Rev. B*, 79, 193204.
- Razzari, L., Toma, A., Clerici, M., Shalaby, M., Das, G., Liberale, C., Chirumamilla, M., Proietti Zaccaria, R., De Angelis, F., Peccianti, M., Morandotti, R., & Di Fabrizio, E. (2013). Terahertz dipole nanoantenna arrays: resonance characteristics. *Plasmonics*, 8, 133-138.
- Rovere, A., Jeong, Y.-G., Piccoli, R., Lee, S.-H., Lee, S.-C., Kwon, O.-P., Jazbinsek, M., Morandotti, R., & Razzari, L. (2018). Generation of high-field terahertz pulses in an HMQ-TMS organic crystal pumped by an ytterbium laser at 1030 nm. *Opt. Express*, 26, 2509-2516.
- Rovere, A., Piccoli, R., Bertoncini, A., Jeong, Y. G., Payeur, S., Vidal, F., Lee, S. H., Seok, J. H., Kwon, O. P., Morandotti, R., Liberale, C., & Razzari, L. (2020). 3D-Printed Photocathodes for Resonant, Terahertz-Field-Driven Ultrafast Electron Emission. *ArXiv*: 2010.12098.
- Rutz, F., Koch, M., Khare, S., Moneke, M., Richter, H., & Ewert, U. (2006). Terahertz quality control of polymeric products. *Int. J. Infrared Milli. Waves*, 27, 547–556.
- Saloman, E. B. (2010). Energy levels and observed spectral lines of ionized argon, Ar II through Ar XVIII. *J. Phys. Chem. Ref. Data*, 39, 033101.

- Schneider, A., Neis, M., Stillhart, M., Ruiz, B., Khan, R. U., & Günter, P. (2006). Generation of terahertz pulses through optical rectification in organic DAST crystals: theory and experiment. *J. Opt. Soc. Am. B*, 23, 1822-1835.
- Shelton, D. (2014). Optical properties of metallic films. In *Metallic Films for Electronic, Optical and Magnetic Applications* (pp. 547-589). Woodhead Publishing Limited.
- Sutherland, R. L. (2003). *Handbook of Nonlinear Optics*. CRC Press.
- Taminiau, T. H., Moerland, R. J., Segerink, F. B., Kuipers, L., & Hulst, N. F. (2007). $\lambda/4$ resonance of an optical monopole antenna probed by single molecule fluorescence. *Nano Lett.*, 7, 28-33.
- Tarekegne, A. T., Hirori, H., Tanaka, K., Iwaszczuk, K., & Jepsen, P. U. (2017). Impact ionization dynamics in silicon by MV/cm THz fields. *New J. Phys.*, 19, 123018.
- Tarekegne, T., K. Iwaszczuk, M. Z., Strikwerda, A. C., & Jepsen, P. U. (2015). Impact ionization in high resistivity silicon induced by an intense terahertz field enhanced by an antenna array. *New J. Phys.*, 17, 043002.
- Toma, A., Tuccio, S., Prato, M., Donato, F. D., Perucchi, A., Pietro, P. D., Marras, S., Liberale, C., Proietti Zaccaria, R., De Angelis, F., Manna, L., Lupi, S., Di Fabrizio, E., & Razzari, L. (2014). Squeezing terahertz light into nanovolumes: nanoantenna enhanced terahertz spectroscopy (NETS) of semiconductor quantum dots. *Nano lett.*, 15, 386-391.
- Tomasino, A., Mazhorova, A., Clerici, M., Peccianti, M., Ho, S.-P., Jestin, Y., Pasquazi, A., Markov, A., Jin, X., Piccoli, R., Delprat, S., Chaker, M., Busacca, A., Ali, J., Razzari, L., & Morandotti, R. (2017). Solid-state-biased coherent detection of ultra-broadband terahertz pulses. *Optica*, 4, 1358-1362.
- Tomasino, A., Parisi, A., Stivala, S., Livreri, P., Cino, A. C., Busacca, A. C., Peccianti, M., & Morandotti, R. (2013). Wideband THz time-domain spectroscopy based on optical rectification and electro-optic sampling. *Sci. Rep.*, 3, 3116.
- Tomasino, A., Piccoli, R., Jestin, Y., Delprat, S., Chaker, M., Peccianti, M., Delprat, S., Chaker, M., Peccianti, M., Clerici, M., Busacca, A., Razzari, L., & Morandotti, R. (2018). Invited Article: Ultra-broadband terahertz coherent detection via a silicon nitride-based deep sub-wavelength metallic slit. *APL Photonics*, 3, 110805.

- Tuccio, S., Razzari, L., Alabastri, A., Toma, A., Liberale, C., De Angelis, F., Candeloro, P., Das, G., Giugni, A., Di Fabrizio, E., & Proietti Zaccaria, R. (2014). Direct determination of the resonance properties of metallic conical nanoantennas. *Opt. Letters*, 39, 571-573.
- Vicario, C., Monoszlai, B., Jazbinsek, M., Lee, S. -H., Kwon, O.-P., & Hauri, C. P. (2015). Intense, carrier frequency and bandwidth tunable quasi single-cycle pulses from an organic emitter covering the terahertz frequency gap. *Sci. Rep.*, 5, 14394.
- Vicario, C., Monoszlai, B., Lombosi, Cs., Mareczko, A., Courjaud, A., Fülöp, J. A., & Hauri C. P. (2014). High energy Yb:CaF₂ femtosecond laser for efficient terahertz generation in lithium niobate. Proc. SPIE 8964, Nonlinear Frequency Generation and Conversion: Materials, Devices, and Applications XIII, 896410.
- Walther, M., Cooke, D. G., Sherstan, C., Hajar, M., Freeman, M. R., & Hegmann, F. A. (2007). Terahertz conductivity of thin gold films at the metal-insulator percolation transition. *Phys. Rev. B*, 76, 125408.
- Wellershoff, S. S., Hohlfeld, J., Gündde, J., & Matthias, E. (1999). The role of electronphonon coupling in femtosecond laser damage of metals. *Appl. Phys. A-Mater.*, 69, S99.
- Woerner, M., Kuehn, W., Bowlan, P., Reimann, K., & Elsaesser, T. (2013). Ultrafast two-dimensional terahertz spectroscopy of elementary excitations in solids. *New J. Phys.*, 15, 025039.
- Xie, X., Dai, J., & Zhang, X.-C. (2006). Coherent control of THz wave generation in ambient air. *Phys. Rev. Lett.*, 96, 075005.
- Yariv, A. (1997). *Optical electronics in modern communications* (5th edition ed.). New York: Oxford Univ. Press.
- Yoshie, T., Scherer, A., Hendrickson, J., Khitrova, G., Gibbs, H. M., Rupper, G., Ell, C., Shchekin, O. B., & Deppe, D. G. (2004). Vacuum Rabi splitting with a single quantum dot in a photonic crystal nanocavity. *Nature*, 432, 200–203.
- Yoshioka, K., Katayama, I., Minami, Y., Kitajima, M., Yoshida, S., Shigekawa, H., & Takeda, J. (2013). Real-space coherent manipulation of electrons in a single tunnel junction by single-cycle terahertz electric fields. *Nat. Photon.*, 10, 762-765.
- Yu, C., Fan, S., Sun, Y., & Pickwell-Macpherson, E. (2012). The potential of terahertz imaging for cancer diagnosis: a review of investigations to date. *Quant Imaging Med Surg.*, 2, 33–45.

- Yurtsever, A., Veen, R. M., & Zewail, A. H. (2012). Subparticle ultrafast spectrum imaging in 4D electron microscopy. *Science*, 335, 59.
- Zalkovskij, M., Bisgaard, C. Z., Novitsky, A., R, Malureanu, Savastru, D., Popescu, A., Jepsen, P. H., & Lavrinenko, A. V. (2012). Ultrabroadband terahertz spectroscopy of chalcogenide glasses. *Appl. Phys. Lett.*, 100, 031901.
- Zewail, A. H. (2010). Four-dimensional electron microscopy. *Science*, 328, 187–193.
- Zhang, H., Virally, S., Bao, Q., Ping, L. K., S, & Massar. (2012). Z-scan measurement of the nonlinear refractive index of graphene. *Opt. Lett.*, 37, 1856–1858.
- Zhang, J., Fan, X. Z., Wang, X., Zhang, G.-F., Geng, K., Zhang, X., & Averitt, R. D. (2015). Terahertz radiation-induced sub-cycle field electron emission across a split-gap dipole antenna. *Appl. Phys. Lett.*, 107, 231101.
- Zuloaga, J., & Nordlander, P. (2011). On the energy shift between near-field and far-field peak intensities in localized plasmon systems. *Nano Lett.*, 11, 1280-1283.

6 APPENDIX I

6.1 Theoretical modeling to retrieve the THz pulse spectrum generated via optical rectification in HMQ-TMS

The model developed by our collaborator (Mojca Jazbinsek) at the Zurich University of Applied Sciences (ZHAW) (Vicario et al., 2015), takes into account velocity matching among the optical and THz waves, linear absorption in the optical and THz range, thickness of the generation crystal, and pump pulse duration. In a non-depleted pump approximation and neglecting cascaded nonlinear effects, the electric-field amplitude E_{THz} of the generated THz wave in a nonlinear optical crystal of length L , which is a function of the pump laser wavelength λ_p and the generated THz frequency, ν , is given by:

$$|E_{\text{THz}}(\nu, \lambda_p)| = \left| \frac{2\pi\nu\mu_0\chi^{(2)}(\nu, \lambda_p)I(\lambda_p)}{n(\lambda_p)\left(\frac{c(\alpha_{\text{THz}}(\nu)/2 + \alpha(\lambda_p))}{2\pi\nu} + i(n_{\text{THz}}(\nu) + n(\lambda_p))\right)} \right| L_{\text{gen}}(\nu, \lambda_p, L) \quad (6.1)$$

where c is the speed of light in vacuum, μ_0 the vacuum permeability, and $I(\lambda_p)$ the Fourier transformed intensity of the pump pulse. In this calculation we take $\chi^{(2)}(\nu, \lambda_p) = 1$ and just evaluate the relative field strengths as a function of λ_p and ν . We also consider the linear optical parameters of the material: $n(\lambda_p)$ and $\alpha(\lambda_p)$ are the refractive index and absorption coefficient at the pump optical wavelength λ_p , respectively, while $n_{\text{THz}}(\nu)$ and $\alpha_{\text{THz}}(\nu)$ are the refractive index and absorption coefficient at the generated THz frequency ν . The important dependence on the crystal length L and the velocity-matching conditions is described by the effective generation length

$$L_{\text{gen}}(\nu, \lambda_p, L) = \sqrt{\frac{\exp(-\alpha_{\text{THz}}L) + \exp(-2\alpha L) - 2\exp(-(\alpha_{\text{THz}}/2 + \alpha)L)\cos(\pi L/L_C(\nu, \lambda_p))}{(\alpha_{\text{THz}}/2 - \alpha)^2 + (\pi/L_C(\nu, \lambda_p))^2}} \quad (6.2)$$

where the coherence length L_C for optical rectification is given by

$$L_C(\nu, \lambda_p) = \frac{c}{2\nu|n_{\text{THz}}(\nu) - n_g(\lambda_p)|} \quad (6.3)$$

with n_g , the group index at the pump optical wavelength.

7 APPENDIX II

7.1 Self phase modulation

An intense optical pulse propagating in a nonlinear medium can drive the instantaneous variation of refractive index of the medium through the optical Kerr effect, leading to a phase delay of the pulse itself. In this way, an initial unchirped optical pulse gains a so-called chirp, i.e., a temporally varying instantaneous frequency.

For instance, let us consider a high-intensity unchirped Gaussian pulse propagating in a nonlinear medium, $I(t) = I_0 \exp\left(-\frac{t^2}{\tau^2}\right)$, where I_0 is the peak intensity and τ is the temporal width of the pulse.

The induced Kerr effect results in a change of the refractive index of the medium:

$$n(t) = n + \Delta n = n + n_2 I(t) \quad (7.1)$$

where n_2 is the second order nonlinear refractive index. This variation in refractive index turns in a shift of the instantaneous phase of the pulse:

$$\phi(t) = \omega_0 t - kz = \omega_0 t - \frac{2\pi}{\lambda_0} n(I)L \quad (7.2)$$

where ω_0 and λ_0 are the carrier frequency and (vacuum) wavelength of the pulse, respectively, and L is the propagation distance. This phase shift leads to the change of the carrier frequency. The instantaneous frequency $\omega(t)$ is indeed given by:

$$\omega(t) = \frac{d\phi(t)}{dt} = \omega_0 - \frac{2\pi}{\lambda_0} L \frac{dn(I)}{dt} = \omega_0 - \frac{4\pi L n_2 I_0}{\lambda_0 \tau^2} \cdot t \cdot \exp\left(-\frac{t^2}{\tau^2}\right) \quad (7.3)$$

Thus, the time-dependent phase-shift given by SPM is associated with the broadening of the frequency spectrum of the optical pulse. The plot of $\omega(t)$ shows the frequency shift of each part of the pulse: the leading edge shifts to lower frequencies ("redder" wavelengths), the trailing edge to higher frequencies ("bluer"), while the very peak of the pulse is not shifted.

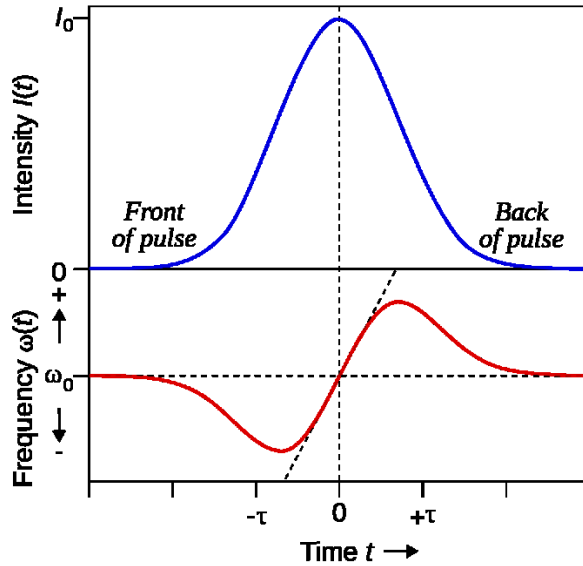


Figure 7.1 Self-phase modulation of a Gaussian optical pulse

A Gaussian pulse (blue curve) propagating through a nonlinear medium undergoes a self-frequency shift (bottom curve) due to SPM. The front of the pulse is shifted to lower frequencies, the back to higher frequencies. At the center of the pulse the frequency shift is approximately linear.

For the central portion of the pulse (between $t = \pm\tau/2$), there is an approximately linear frequency shift (chirp) given by:

$$\omega(t) = \omega_0 - \alpha \cdot t \quad (7.4)$$

where α is:

$$\alpha = \frac{d\omega}{dt} \Big|_0 = \frac{4\pi L n_2 I_0}{\lambda_0 \tau^2} \quad (7.5)$$

Typically, for not-chirped pulses, the SPM-induced-broadening of the optical spectrum is symmetric with respect to the central frequency of the optical pulse and can exhibit strong oscillations. The oscillatory behaviour is essentially due to the strong excursions of the instantaneous frequency, so that in general there are different contributions to the Fourier integral for a given frequency component. Depending on the exact frequency, these contributions may constructively add up or cancel each other.

SOMMAIRE RÉCAPITULATIF

Développement de Sources Térahertz Intenses au Moyen d'un Laser à Ytterbium et une Application dans la Photoémission d'Électrons Pilotée par le Champ à Partir de Nanostructures Résonantes Hors du Plan

Motivations de la thèse

Au cours des dernières décennies, le nombre de recherches et d'applications impliquant des fréquences térahertz (THz, $1 \text{ THz} = 10^{12} \text{ Hz} = 4.1 \text{ meV} = 33.3 \text{ cm}^{-1}$, 1 THz correspond à une longueur d'onde de 300 μm) a connu une augmentation impressionnante, notamment grâce à la disponibilité croissante de lasers à femtoseconde amplifiés. En effet, ces sources optiques ont ouvert la voie au développement de nouvelles techniques basées sur l'optique non linéaire pour la génération et la détection d'impulsions THz, telles que la *rectification optique* (RO) et la *détection électro-optique* (DEO) (Dexheimer, 2007). En particulier, les impulsions THz à champ élevé sont d'un grand intérêt pour étudier la réponse non linéaire des systèmes de la matière à ces fréquences, ce qui permet également des études cohérentes dans le domaine temporel (Hafez et al., 2016). Ces dernières années, on a constaté que la technologie laser à base d'Yb offrait une stabilité thermique et une puissance de sortie moyenne plus élevées que les systèmes laser Ti:Saphir utilisés traditionnellement, ce qui peut permettre d'améliorer encore le développement des sources THz de table. Toutefois, certains problèmes subsistent en ce qui concerne la mise en œuvre de sources THz intenses pompées à 1030 nm (c'est-à-dire la longueur d'onde d'émission des lasers Yb). Par exemple, les cristaux de LiNbO₃ présentent un coefficient non linéaire élevé, ce qui assure une génération de THz à haut rendement par le biais de la RO. Cependant, un schéma de pompage complexe et non colinéaire est nécessaire pour obtenir la condition d'adaptation de phase nécessaire à 1030 nm, ce qui nécessite un alignement non trivial (Hebling et al., 2002). D'autre part, les cristaux organiques non linéaires (par exemple DAST, OH1) offrent une alternative prometteuse pour la génération efficace d'impulsions THz intenses, car ils présentent une réponse non linéaire élevée et peuvent être pompés dans un schéma colinéaire (Hauri et al., 2011; Kwon et al., 2008). Par contre, la longueur d'onde optimale pour remplir la condition d'adaptation de phase dans ces cristaux se situe généralement dans la plage de 1.3 à 1.5 μm, ce qui nécessite un autre amplificateur paramétrique optique à coupler au système laser femtoseconde.

Dans la première partie de mon projet de thèse, j'ai caractérisé les impulsions THz à champ élevé émises par un cristal organique de 2-(4-hydroxy-3-méthoxystyryl)-1-méthylquinolinium 2,4,6-triméthylbenzènesulfonate (HMQ-TMS) pompé colinéairement par un système laser Yb amplifié. J'ai notamment utilisé un laser au tungstate de potassium et de gadolinium dopé à l'Yb (Yb:KGW, Pharos PH1-SP-1mJ, *Light Conversion*), qui émet des impulsions de 170 fs de long centrées à 1030 nm avec une énergie d'impulsion maximale de 1 mJ et une fréquence de répétition accordable jusqu'à 1 MHz (6 W de puissance moyenne: 1 mJ @ 6 kHz). De plus, j'ai utilisé ces impulsions THz intenses dans une expérience de preuve de principe non linéaire (saturation de l'absorption dans une couche mince semi-conductrice dopée), montrant ainsi le potentiel de cette nouvelle configuration pour l'exploration des effets non linéaires THz (Rovere et al., 2018). En même temps, la largeur de bande de gain des lasers Yb limite la durée d'impulsion dans la plage 250 fs - 130 fs. Afin de résoudre ce problème, on peut utiliser des techniques de compression d'impulsion non linéaire, assurant la réduction de la durée d'impulsion à quelques dizaines de femtosecondes (Jeong et al., 2018). Ainsi, dans un projet de collaboration, j'ai exploité ces impulsions comprimées pour générer des impulsions THz à très large bande (jusqu'à 60 THz) et à haut champ THz via une source de plasma bicolore (Piccoli et al., 2019). Cette source peut étendre les recherches non linéaires à des fréquences THz qui sont particulièrement pertinentes pour la dynamique des phonons optiques dans les systèmes de matière condensée. Les deux sources de THz seront décrites en suivant, en présentant la caractérisation complète des impulsions THz générées.

L'utilisation d'impulsions THz intenses est également très intéressante pour l'extraction et l'accélération de faisceaux d'électrons par photoémission sur le terrain à partir de nanostructures métalliques. En fait, le rayonnement THz assure un processus d'émission purement piloté par le champ. De plus, les électrons sont extraits et accélérés en un demi-cycle optique, ce qui permet une émission d'électrons en phase avec l'impulsion électromagnétique. La stabilité de phase intrinsèque de l'enveloppe porteuse des impulsions THz générées par RO peut ainsi fournir un contrôle cohérent précis des groupes d'électrons extraits (Yoshioka et al., 2013). Traditionnellement, les nanopuces métalliques non résonantes ont été étudiées pour la photoémission par THz (Herink et al., 2014; Li & Jones, 2016). Dans des études plus récentes, l'amélioration du champ supérieur accordée par les antennes planaires résonantes a été exploitée, permettant la photoémission d'électrons à des amplitudes de champ incident plus faibles (Iwasczuk et al., 2014; Zhang et al., 2015). Cependant, la proximité du substrat sous les antennes planaires entrave l'utilisation pratique des faisceaux d'électrons émis pour leurs possibles applications. Dans la deuxième partie de ce projet de doctorat, j'ai donc utilisé les impulsions THz à champ élevé générées par la source de cristaux organiques pour

étudier la photoémission d'électrons à champ THz à partir de photocathodes résonantes de conception rationnelle (Rovere et al., 2020). En particulier, j'ai étudié l'utilisation de *nanocones résonnantes* (resonant nanocones, RNCs) verticaux à THz pour la photoémission d'électrons hors plan commandée par le champ. Tout d'abord, j'ai optimisé leur conception par des simulations numériques afin d'accorder leur résonance au pic de fréquence de la source. En outre, j'ai étudié la disposition des RNCs sous forme de réseau, ce qui a permis de constater que cela permet d'augmenter encore le champ électrique local par une réponse collective en THz. Nous avons prouvé qu'un tel comportement collectif peut également être utilisé pour augmenter le champ local de THz sur un nanoémetteur individuel, en concevant un réseau de nanocylindres résonants avec une seule RNC au milieu. Les échantillons ont été fabriqués par nos collaborateurs de KAUST en utilisant une méthode de nanolithographie d'impression 3D. Nos caractérisations optiques et électriques des dispositifs fabriqués ont confirmé les avantages des conceptions proposées pour l'extraction des électrons par THz, qui ont également été corroborés par une modélisation numérique et analytique plus poussée du processus de photoémission.

Impulsions intenses de THz provenant d'un cristal organique HMQ-TMS pompé à 1030 nm

Pour les travaux présentés dans cette section, j'ai conçu et mis en place le système THz, effectué la caractérisation expérimentale de la source et dirigé l'analyse des données. J'ai également effectué le test de preuve de principe non linéaire.

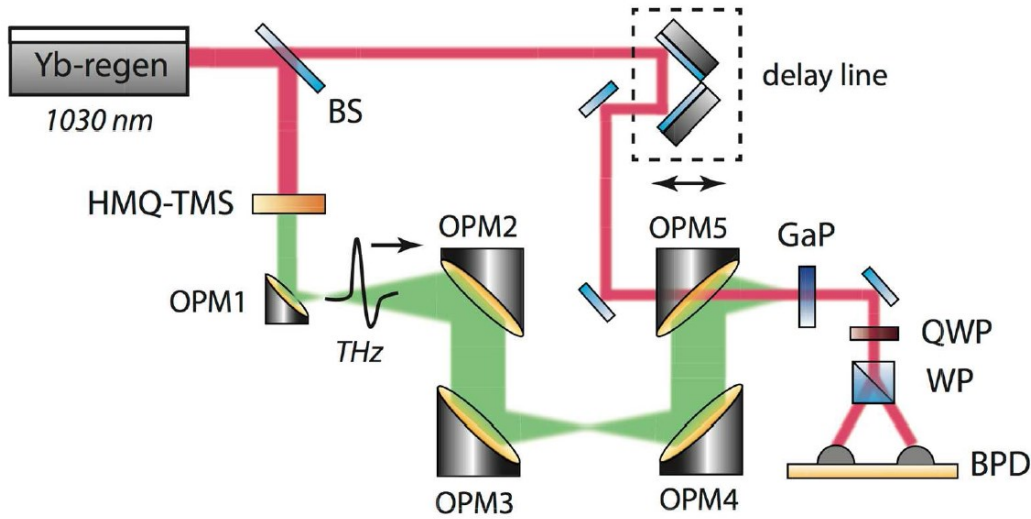


Figure 8.1 Setup SDT utilisée pour la caractérisation de la source THz HMQ-TMS

BS - séparateur de faisceau 80:20, OPM - miroirs paraboliques à 90 degrés hors axe (longueur focale de OPM1: 0,5", OPM2: 6", OPM3 et OPM4: 3", OPM5: 2"), QWP - plaque quart d'onde, WP - prisme de Wollaston, BPD - photodiodes équilibrées. La détection est effectuée par DEO dans un cristal GaP orienté <110> de 300- μ m-épaisseur. Reproduit avec la permission de (Rovere et al.) © 2018 The Optical Society.

Dans cette mesure, un cristal HMQ-TMS d'une épaisseur de 630 μm a été utilisé pour la génération d'impulsions THz. Pour la caractérisation du champ électrique THz, nous avons exploité un setup de *spectroscopie THz dans le domaine temporel* (THz-SDT) standard dans un environnement purgé à l'azote, comme celle illustrée dans la Figure 8.1. Le rayonnement résiduel de la pompe après le cristal HMQ-TMS a été bloqué au moyen d'une feuille de polyéthylène noir de 100- μm d'épaisseur. Le rayonnement THz généré a été collecté et finalement focalisé sur un cristal orienté <110> de phosphure de gallium (GaP) de 300 μm d'épaisseur au moyen d'un ensemble de miroirs paraboliques en hors axe (off-axis parabolic mirror, OPM). Nous avons acquis la trace temporelle du champ électrique THz par la technique standard DEO, en utilisant le cristal GaP comme détecteur, avec un pas de retard de 15 fs. Comme la taille du faisceau de sortie du laser (4,5 mm de diamètre à $1/e^2$ de l'intensité) est plus grande que l'ouverture nette du cristal HMQ-TMS (diamètre de 3 mm), un trou d'épingle a été utilisé pour limiter la taille du faisceau de pompage à l'ouverture du cristal.

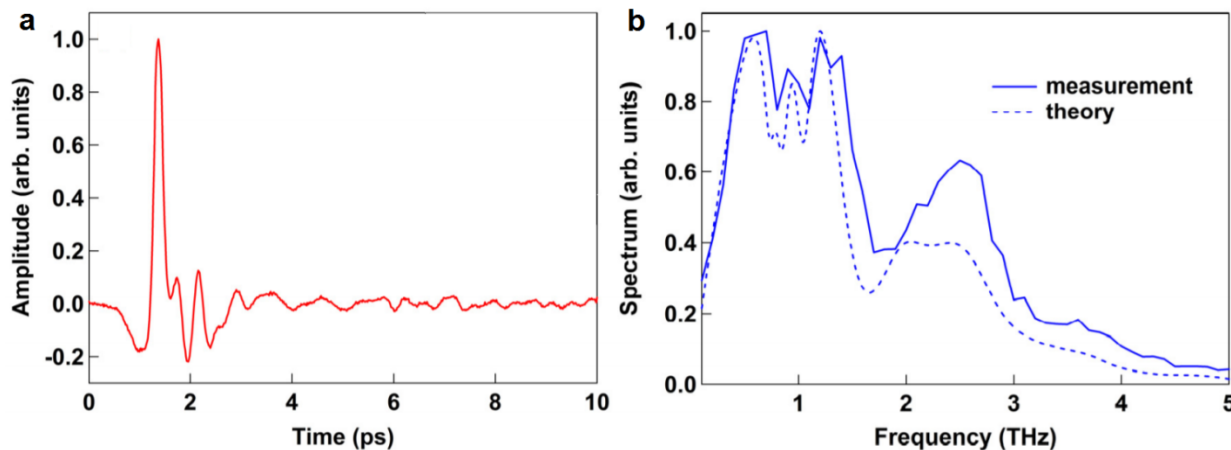


Figure 8.2 Forme d'onde en THz et spectre générée par RO dans le cristal HMQ-TMS

(a) Forme d'onde du champ électrique de THz émise par le cristal HMQ-TMS de 630- μm d'épaisseur et récupérée par DEO à l'aide d'un cristal de détection GaP. (b) Spectres d'émission mesurés (solide) et calculés (pointillés) en THz. Reproduit avec la permission de (Rovere et al.) © 2018 The Optical Society.

Cette source fournit des impulsions THz (Figure 8.2a) avec un spectre d'émission s'étendant au-delà de 3 THz (Figure 8.2b). L'absorption située à 1.7 THz est associé à un mode phonon du cristal HMQ-TMS (Vicario et al., 2015). Il a également été possible de simuler numériquement le spectre de sortie détecté de la source THz, sous l'approximation de la pompe non appauvrie en ondes planes et sans tenir compte des effets non linéaires en cascade. Plus précisément, dans les calculs effectués par notre collaborateur de l'Université des sciences appliquées de Zurich (ZHAW), le spectre de puissance de sortie de notre système laser Yb, l'indice de réfraction et le coefficient d'absorption du cristal organique aux fréquences optiques et THz (Brunner et al., 2014) ont été pris en compte, ainsi que la fonction de réponse du détecteur GaP, en tenant compte de sa THz (Leitenstorfer et al., 1999).

et des caractéristiques optiques (Aspnes & Studna, 1983). Comme il est possible de l'observer dans la Figure 8.2b, il y a un très bon accord entre les résultats expérimentaux et numériques, notamment en ce qui concerne la bande d'émission globale et la position de l'absorption du phonon.

Nous avons ensuite estimé l'intensité du champ électrique de crête de THz récupéré par la DEO. Pour les petites modulations, l'intensité différentielle mesurée par les photodiodes équilibrées (voir Figure 8.1) est directement proportionnelle à l'intensité du champ de THz, comme le montre la relation suivante:

$$\frac{\Delta I}{I} = \frac{2\pi d n_0^3 r_{41} t E_{\text{THz}}}{\lambda_0} \quad (8.1)$$

où $\Delta I/I$ est la modulation d'intensité normalisée, E_{THz} est le champ électrique de crête à THz, λ_0 est la longueur d'onde centrale de la pompe, tandis que $n_0 = 3.11$, $t = 0.46$, $d = 300 \mu\text{m}$, et $r_{41} = 0.97$ pm/V sont respectivement l'indice de réfraction à λ_0 , le coefficient de transmission à THz, l'épaisseur et le coefficient électro-optique du cristal GaP. Afin d'éviter une sur-rotation du cristal GaP (Fletcher, 2002), ainsi que des effets non linéaires supplémentaires, le signal THz incident a été atténué en plaçant 2 tranches de silicium à haute résistivité (HR Si > 5000 $\Omega \text{ cm}$) dans le trajet du faisceau (chacune d'entre elles fournissant environ 70% de la transmission du champ électrique).

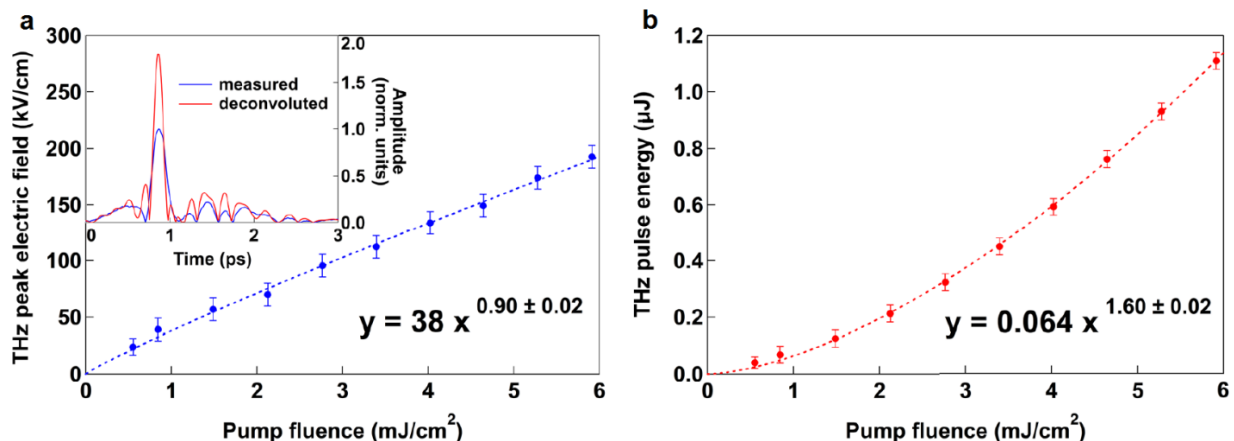


Figure 8.3 Crête du champ électrique THz et énergie des impulsions THz par rapport à la fluence de pompe

(a) Champ électrique de crête et (b) énergie des impulsions THz générées par le cristal HMQ-TMS de 630- μm -épaisseur en fonction de la fluence de la pompe incidente. L'encadré montre les valeurs absolues normalisées du champ THz mesuré (bleu) et d'une forme d'onde obtenue par déconvolution de la trace mesurée avec une sonde optique gaussienne de 170 fs - FWHM (rouge). Les formules indiquées dans les deux Figures représentent le meilleur ajustement des données expérimentales (lignes pointillées). Reproduit avec la permission de (Rovere et al.) © 2018 The Optical Society.

Le champ électrique de crête THz mesuré en fonction de la fluence de la pompe (qui est estimée comme le rapport entre l'énergie de pompe incidente sur le cristal et la surface du trou d'épinglé) est indiqué sur la Figure 8.3a, montrant une tendance quasi-linéaire avec un champ électrique de crête

THz maximum d'environ 200 kV/cm. Cependant, il faut noter que l'impulsion de la sonde optique étant relativement longue (FWHM de 170 fs), elle ne permet pas de résoudre complètement l'amplitude des oscillations du champ électrique de THz généré. Pour illustrer ceci, dans l'encadré de la Figure 8.3a, nous montrons la valeur absolue de la trace du champ électrique mesuré E_{mes} (bleu) comparée à celle d'une forme d'onde THz E_{dec} (rouge) obtenue en déconvolvant la trace mesurée avec une sonde optique gaussienne G de 170 fs, selon la formule : $E_{\text{mes}} = E_{\text{dec}} * G$. Comme il ressort de cette évaluation, la valeur de crête effective du champ THz peut être jusqu'à 1,8 fois plus élevée que celle extraite de notre mesure DEO, ce qui correspond à un champ électrique de crête d'environ 350 kV/cm à la position du cristal de détection. Nous avons également mesuré l'énergie des impulsions THz au moyen d'un détecteur pyroélectrique (THZ-I-BNC de Gentec-EO). L'énergie THz générée est présentée sur la Figure 8.3b, montrant une dépendance super-linéaire de la fluence de l'impulsion de pompe. À la fluence de pompage incidente maximale d'environ 5.9 mJ/cm² (bien en dessous du seuil de dommage précédemment signalé pour le cristal HMQ-TMS, c'est-à-dire > 20 mJ/cm² (Vicario et al., 2015), les impulsions THz générées atteignent une valeur d'environ 1.1 μJ par impulsion, ce qui correspond à un rendement de conversion significatif de 0.26 %. Il est remarquable que le processus de génération THz étudié puisse être mis à l'échelle, en termes d'énergie de THz et de champ électrique de pointe, en utilisant des cristaux à plus grande ouverture et des énergies de pompage plus élevées.

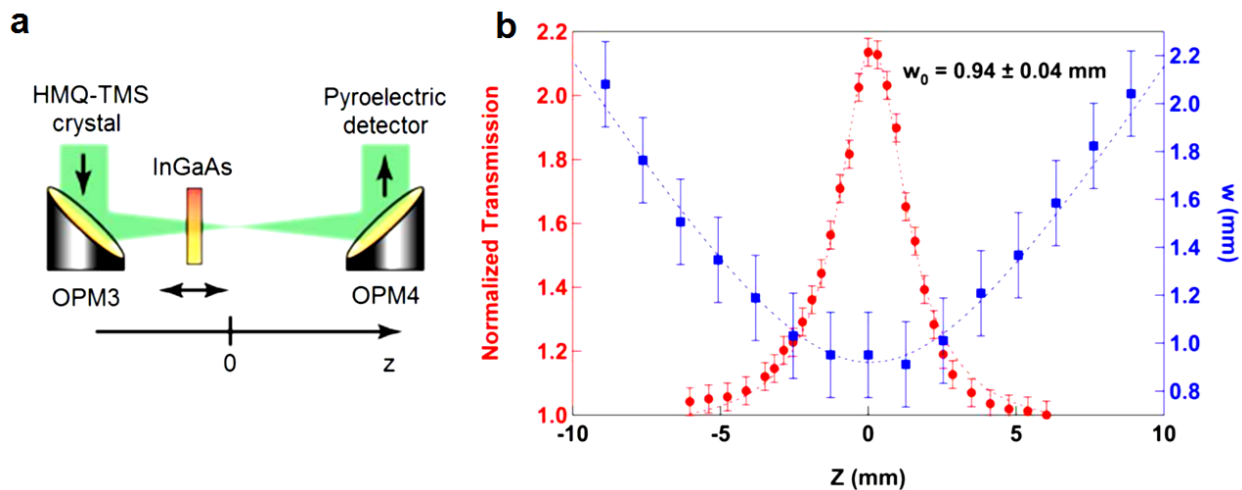


Figure 8.4 Mesure du Z-scan

(a) Schéma de la configuration pour la mesure du Z-scan. (b) Transmission normalisée du film InGaAs (points rouges) et des valeurs de taille du faisceau THz (points bleus) mesurées en fonction de la position z ($z = 0$ correspond à la position focale THz). Reproduit avec la permission de (Rovere et al.) © 2018 The Optical Society.

Afin de démontrer le potentiel de cette source pour les investigations non linéaires en THz, nous avons réalisé une expérience de preuve de principe (Z-scan) sur un film mince d'InGaAs dopé à n

d'une épaisseur de 500 nm (densité de porteurs de $\sim 2 \times 10^{18} \text{ cm}^{-3}$), déposé sur un substrat d'InP d'indice de réfraction n. En effet, le Z-scan est une technique de caractérisation non linéaire très courante qui permet, par exemple, de déterminer la non-linéarité de Kerr ainsi que les coefficients d'absorption non linéaires d'un matériau à partir de changements de transmission dépendant de l'intensité (Zhang et al., 2012). Dans cette mesure, nous avons enregistré l'énergie THz transmise à travers l'échantillon pendant qu'il était balayé le long de la direction de propagation z à travers le faisceau THz focalisé (voir Figure 8.4a). En particulier, le fort champ THz transmis peut induire une transition intermittente (de la vallée Γ à la vallée L) des porteuses dans la bande de conduction InGaAs. Comme la mobilité des porteuses dans la vallée L du satellite est plus faible, la conductivité du film est par conséquent réduite (et donc le courant entraîné), ce qui entraîne une transmission THz plus élevée. Pour chaque point du Z-scan, nous avons extrait la transmission normalisée comme étant l'énergie transmise détectée divisée par celle mesurée à faible intensité THz. Les résultats de cette mesure sont présentés sur la Figure 8.4b (cercles rouges). Nous avons observé une saturation significative de l'absorption du THz, avec une augmentation maximale de la transmission d'environ 2.2 fois au foyer. Ce changement de transmission est lié à la modification de la taille du faisceau THz (et donc à la modification de son intensité) le long de la direction z entre OPM3 et OPM4, qui ont été retrouvés par des mesures au couteau sur le faisceau THz. Les résultats de cette caractérisation sont également présentés sur la Figure 8.4b (carrés bleus). De cette façon, nous avons estimé une taille de faisceau THz de 940 μm à la position focale de l'OPM3. Cette caractérisation confirme en outre l'intensité significative du champ électrique des impulsions THz générées en utilisant la configuration proposée. Comme nous le verrons en suivant, cette source a également été utilisée pour commander l'émission d'électrons à partir de nanostructures verticales résonantes à THz.

Génération de plasma bicolore d'impulsions THz à haut champ et à ultra large bande

Pour les travaux présentés dans cette section, j'étais responsable de la partie expérimentale concernant la génération et la détection des impulsions THz à large bande, tandis que R. Piccoli s'est occupé de l'étape de compression des impulsions du laser Yb et a dirigé l'analyse des données.

Les sources de plasma bicolore sont avantageuses par rapport à la RO pour la génération d'impulsions THz à large bande. En fait, contrairement aux cristaux non linéaires en vrac, les gaz sont continuellement renouvelables et ne sont donc pas limités par les problèmes de dommages, ils peuvent donc être pompés à des intensités extrêmement élevées, étant capables de fournir des champs électriques de pointe supérieurs à des MV/cm (Oh et al., 2013). De plus, la largeur de bande THz générée n'est pratiquement limitée que par la durée d'impulsion de la pompe laser, grâce à la

très faible dispersion des gaz (Karpowicz et al., 2008). Dans cette section, nous rapportons la génération d'impulsions THz à très large bande via une source de plasma bicolore, utilisant des impulsions de laser Yb comprimées dans le temps au moyen d'une technique non linéaire exploitant une fibre creuse remplie de gaz (hollow-core fiber, HCF). Les HCF sont connues pour résister à des puissances moyennes supérieures à 100 W (Hädrich et al., 2013) et à des énergies d'impulsion élevées (Cardin et al., 2015). La combinaison des lasers Yb et des HCF constitue donc un outil unique pour la génération de rayonnements THz de puissance moyenne élevée, à champ élevé et à très large bande, par l'intermédiaire d'un plasma d'air excité en deux couleurs.

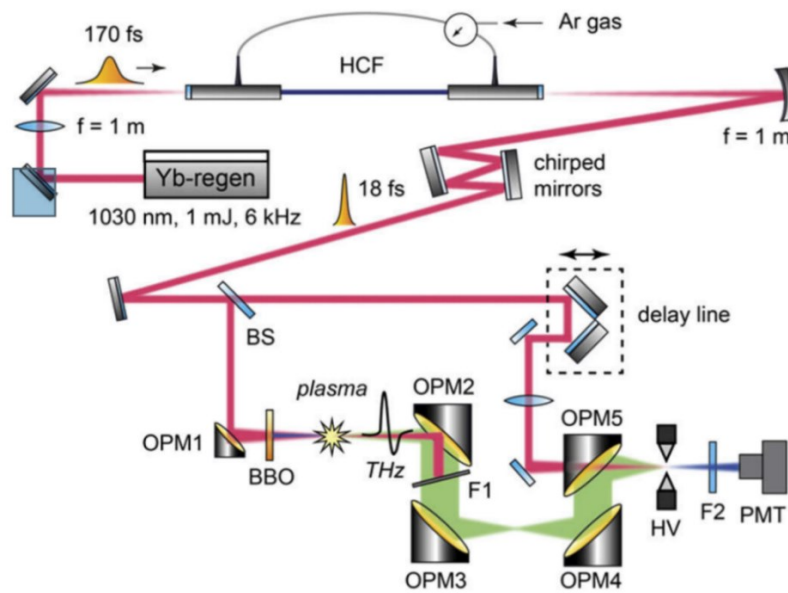


Figure 8.5 Setup pour la génération et la caractérisation des impulsions THz à large bande

HCF - fibre creuse ; BS - séparateur de faisceau 90:10; OPM1 - miroir parabolique hors axe $f = 4"$; OPM2, OPM3, et OPM4 $f = 3"$; OPM5 $f = 2"$; F1 - filtre passe-haut; HV - électrodes haute tension; F2 - filtre passe-bas pour 515 nm; PMT - tube photomultiplicateur. Reproduit avec la permission de (Piccoli et al.) © 2019 The Optical Society.

Les impulsions laser de 170 fs de long (énergie par impulsion de 0.94 mJ, fréquence de répétition de 6 kHz) émises par l'amplificateur régénératif Yb:KGW ont été focalisées dans un HCF de 1.6 m de long (500 μm de diamètre intérieur - *few-cycle Inc.*) rempli de gaz Ar à la pression statique de 2.8 bars, pour fournir la non-linéarité du troisième ordre requise et élargir le spectre des impulsions via le SPM. Le spectre est élargi le long de la propagation dans le HCF par des SPM entre environ 900 nm et 1100 nm, avec une efficacité de transmission globale supérieure à 70%. Après la fibre, le faisceau de sortie a été collimaté avec un miroir revêtu d'Al ($f = 1 \text{ m}$) et comprimé par quatre rebonds sur des miroirs à large bande (PC1611, *UltraFast Innovations*). Après les miroirs chirpés, les impulsions de pompage sont comprimées à $\sim 18 \text{ fs FWHM}$ (facteur de compression d'environ 9). Les impulsions comprimées ont ensuite été utilisées dans une configuration THz-SDT, comme le montre la Figure

8.5. Le faisceau d'entrée (taille de 2.4 mm à $1/e^2$ de l'intensité) a été séparé par un diviseur de faisceau 90:10 vers les trajets de la pompe et de la sonde. Le faisceau de pompe, qui représentait environ 471 μJ d'énergie ($\approx 26 \text{ GW}$ de puissance de crête), a été focalisé en un cristal BaB₂O₄ (BBO) de 100- μm d'épaisseur au moyen d'un miroir parabolique hors axe (OPM1) d'une longueur focale de 4 pouces.

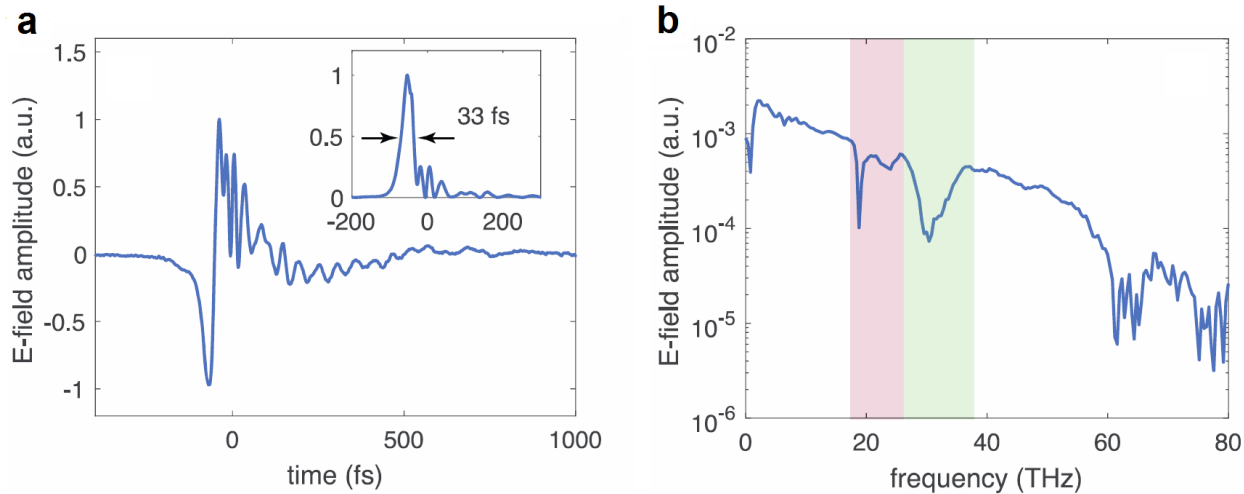


Figure 8.6 Forme d'onde du champ électrique et spectre de la source ultra-large bande THz

(a) Forme d'onde du champ électrique des impulsions de THz récupérées par la méthode DCBA. L'encadré montre l'enveloppe d'intensité comportant un pic principal d'une durée de 33 fs FWHM. **(b)** Spectre de champ électrique correspondant calculé par FFT. Reproduit avec la permission de (Piccoli et al.) © 2019 The Optical Society.

Les ondes fondamentales et de seconde harmonique ont été mélangées à la position focale afin de générer un filament de plasma bicolore dans l'air (longueur d'environ 3 mm). Un second miroir hors axe OPM2, d'une longueur focale et d'un diamètre de 2 pouces, a été utilisé pour collimater le rayonnement THz ultra-large bande émis, tandis qu'un filtre de 1 mm d'épaisseur (*Edmund* long-pass 1.65 μm , un film diélectrique multicouche sur un substrat de silicium) a été utilisé pour réfléchir la pompe résiduelle et la lumière de seconde harmonique. Une sélection appropriée de ce filtre pour les systèmes à base d'Yb devient particulièrement critique car les plaques de silicium, généralement utilisées dans les installations THz utilisant des lasers Ti:Saphir, ne sont pas adaptées pour bloquer correctement la lumière à des longueurs d'onde supérieures à 1000 nm (bande interdite du silicium à 1.14 eV ≈ 1087 nm). En outre, il est important de noter que les revêtements hautement réfléchissants sont une exigence stricte pour le fonctionnement à puissance moyenne élevée envisagé de ce type de sources THz à base d'Yb, en raison du fait que, dans ce cas, même une petite fraction de l'absorption optique endommagerait thermiquement le filtre. Un ensemble d'OPM de longueurs focales égales à 3, 3 et 2 pouces, respectivement, a été utilisé pour diriger le rayonnement vers l'étage de détection (voir Figure 8.5). Les impulsions THz à ultra large bande ont été détectées de manière

cohérente par la technique de *détection cohérente biaisée par l'air* (DCBA) (Karpowicz et al., 2008). À cette fin, les impulsions THz et les impulsions de la sonde ont été focalisées ensemble dans un espace de 1 mm de large entre deux électrodes, auxquelles une tension bipolaire carrée (jusqu'à 1.7 kV crête à crête, synchronisée à la moitié de la fréquence de répétition du laser) a été appliquée. La forme d'onde THz a été acquise dans un environnement purgé à l'azote, en enregistrant la lumière de seconde harmonique induite par le champ THz dans l'air avec un tube photomultiplicateur (PMM01, Thorlabs) en fonction du retard relatif entre les impulsions THz et les impulsions de la sonde (avec un pas de 5 fs). Comme l'illustre la Figure 8.6a, la forme d'onde THz présente une oscillation importante, presque à cycle unique, avec des caractéristiques temporelles inférieures à 50 fs. Une gamme dynamique maximale, définie comme le rapport entre l'amplitude maximale du signal et l'écart-type du niveau de bruit (Naftaly & Dudley, 2009), de 200 a été mesurée à la tension de polarisation maximale de 1.7 kV, ce qui suggère que cette configuration THz est suffisamment bonne pour être utilisée dans les mesures de spectroscopie THz-SDT. Le spectre correspondant, calculé numériquement par FFT, s'étend jusqu'à 60 THz (au plancher de bruit en échelle logarithmique) (Figure 8.6b), exploitant ainsi efficacement le contenu en fréquence des impulsions de pompe comprimées ($1/18 \text{ fs} = 55.6 \text{ THz}$). L'oscillation dans le temps sur le front arrière de l'impulsion THz, et les creux d'absorption correspondants dans le spectre, proviennent des propriétés spectrales du filtre passe-haut utilisé pour bloquer la lumière résiduelle de la pompe/seconde harmonique dans notre installation.

Cette source à large bande THz peut être utilisée à l'avenir pour des expériences non linéaires à des fréquences THz. Par exemple, une expérience possible concerne l'utilisation de cette source pour l'étude non linéaire du système fortement couplé composé de cavités plasmoniques et de nanocristaux CdS (Jin et al., 2018), en exploitant le fait que la source développée peut fournir des impulsions intenses avec un contenu en fréquence couvrant la région de résonance hybride, qui est d'environ 8 THz.

Nanocones résonants THz imprimés en 3D pour la photoémission ultra-rapide hors du plan

Dans mon travail de thèse, je présente une conception innovante de photocathode pour la photoémission hors plan pilotée par le champ THz, rendue possible par la grande reproductibilité et le contrôle précis offerts par la nanolithographie d'impression 3D. En particulier, des RNCs hors plan ont été étudiés, présentant une résonance monopolaire centrée à 1 THz, en raison de la présence d'une surface conductrice en or au bas des RNCs qui agit comme un plan d'image miroir (croquis de la Figure 8.7a). En outre, la réponse collective d'un réseau de RNCs peut être réglée avec précision

pour obtenir un champ local de THz encore plus élevé aux sommets des RNCs, qui peut être exploité pour obtenir une augmentation significative de l'émission d'électrons par champ par rapport aux nanoparticules non résonantes standard. Enfin, en tirant parti de la liberté géométrique accordée par la fabrication de l'impression 3D, nous démontrons que cet "*effet de coopération*" peut également être conçu pour confiner la photoémission commandée par le champ à un émetteur RNC individuel. Cette émission isolée est obtenue en positionnant un unique émetteur RNC dans un ensemble de cylindres d'or résonants.

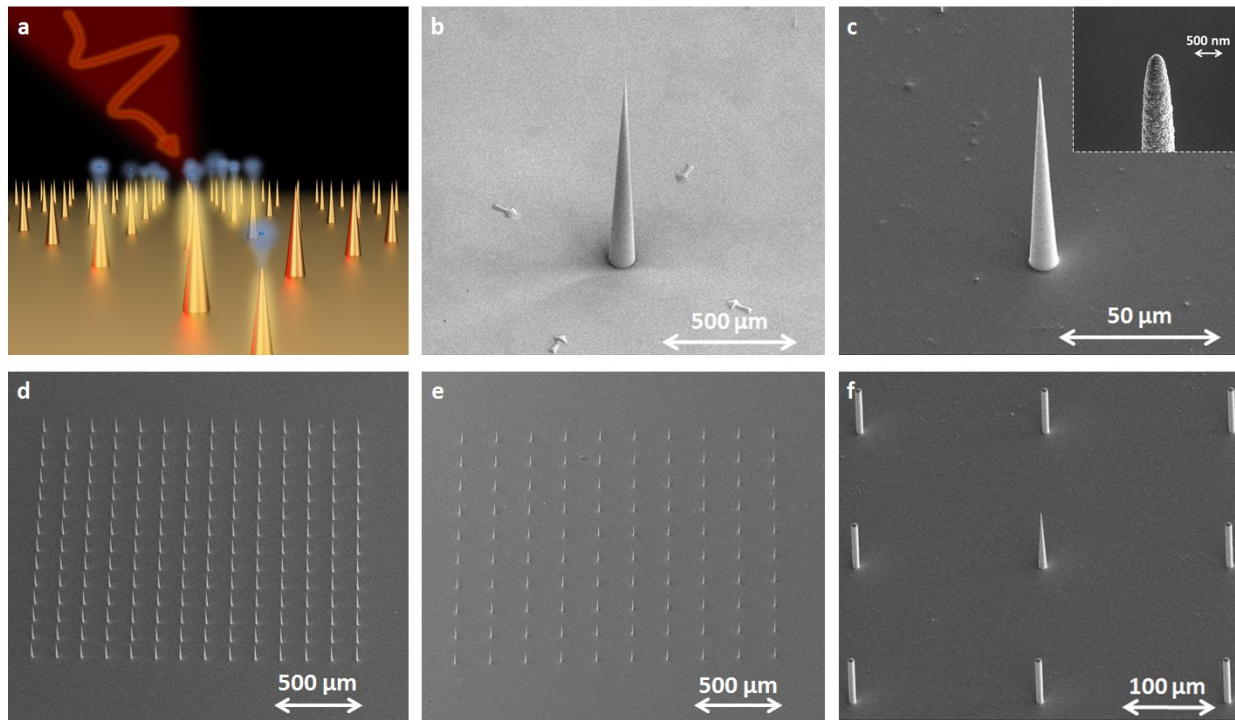


Figure 8.7 Émission d'électrons par champ de THz à partir de RNCs à résonance verticale

(a) Illustration de la photoémission d'électrons à champ de THz à partir d'un réseau de RNCs d'or à résonance monopolaire. Images MEB des échantillons fabriqués: (b) la nanopuce non résonante de 1 mm de hauteur, (c) le RNC unique, (d) le réseau de RNCs, (e) le réseau de RNCs coopératifs, et (f) le RNC unique dans un réseau de cylindres. Le détail du sommet d'un RNC fabriqué est indiqué dans l'encadré de la Figure 8.7c.

Dans cette étude, nous avons étudié différents types de nanostructures et d'arrangements : i) une *nanopuce non résonante* (Figure 8.7b), ii) une *RNC unique* (Figure 8.7c), iii) un *réseau de RNCs* (Figure 8.7d), iv) un *réseau de RNCs coopératives* (Figure 8.7e), et v) une *RNC unique dans un réseau de cylindres* (Figure 8.7f). Dans le cas des structures résonantes, nous avons adapté leur réponse en THz au moyen de simulations numériques (*COMSOL Multiphysics Software*) en centrant la résonance monopolaire autour de 1 THz. Le modèle consiste en différentes configurations de RNCs d'or THz sur une surface métallique, en utilisant les paramètres Drude pour la permittivité de l'or dérivés par (Walther et al., 2007), tandis qu'un domaine aérien avec $\epsilon_{air} = 1$ a été envisagé en plus de ce

système. Le champ lumineux est envoyé depuis le haut du modèle sous la forme d'une onde monochromatique plane à polarisation p arrivant à un angle d'incidence de $\theta = 30^\circ$ par rapport à l'axe principal du RNC (défini comme l'axe z, Figure 8.8a) avec des fréquences comprises entre 0.1 et 10 THz. Notez que seule la composante z du champ électrique de THz ($E_z = E_0 \sin\theta$) contribue à exciter la résonance monopolaire du RNC. Au-dessus et sur les côtés latéraux du modèle géométrique global, des couches dites "parfaitement adaptées" ont été introduites pour éviter les artefacts de réflexion. Pour simuler un réseau infini, des conditions aux limites périodiques ont été appliquées aux côtés latéraux du modèle. La réflectance des RNCs a été récupérée à l'aide de la formule suivante $R = 1 - (P_{\text{abs}} + P_{\text{sca}})/P_0$, où P_0 est la puissance incidente, tandis que $P_{\text{abs}} = \int Q_h dV$ et $P_{\text{sca}} = \int W dS$ sont les puissances absorbées et diffusées calculées des RNCs, respectivement, Q_h l'énergie dissipée dans le volume du RNC et W le flux de Poynting vers l'extérieur du RNC.

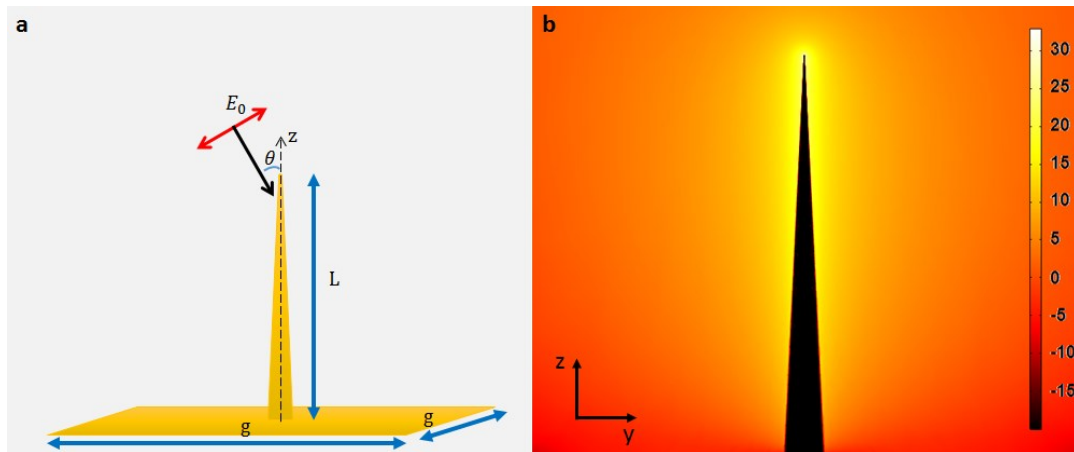


Figure 8.8 Modèle d'un RNC à THz

(a) Schéma du modèle de simulation où l'onde plane frappe le RNC d'or avec un angle $\theta = 30^\circ$. (b) distribution du champ proche (en dB) en correspondance de la fréquence de résonance monopolaire du RNC.

La Figure 8.8b montre la distribution en champ proche en correspondance de la fréquence de résonance monopolaire du RNC. En outre, il est possible de récupérer l'amélioration du champ sous la forme $F = E_{\text{loc}}/E_0$, où E_{loc} est le champ électrique local calculé à 1 nm au-dessus du sommet du RNC et E_0 est le champ électrique incident. Dans le cas d'une nanopuce métallique non résonante, l'augmentation du champ peut être évaluée de manière analytique en considérant une tige cylindrique de rayon R coiffée d'un hémisphère (Podenok et al., 2006). Dans ce cas, l'amélioration du champ est donnée par $F = \alpha(\lambda / R)$, avec $\alpha = 0.06$ (Li & Jones, 2016) (Figure 8.9a). Après la fabrication des échantillons conçus numériquement (réalisée par nos collaborateurs), la caractérisation spectrale THz des réseaux a été effectuée dans une géométrie de réflexion en utilisant une configuration THz-SDT. En particulier, le rayonnement THz a été généré par RO dans un cristal

GaP de 500 μm d'épaisseur, pompé par notre laser Yb amplifié, et détecté par DEO dans un second cristal GaP de 3 mm d'épaisseur. Les mesures ont été effectuées dans une atmosphère purifiée à l'azote et les spectres de réflectance correspondants ont été extraits en prenant comme référence la réponse d'une surface d'or.

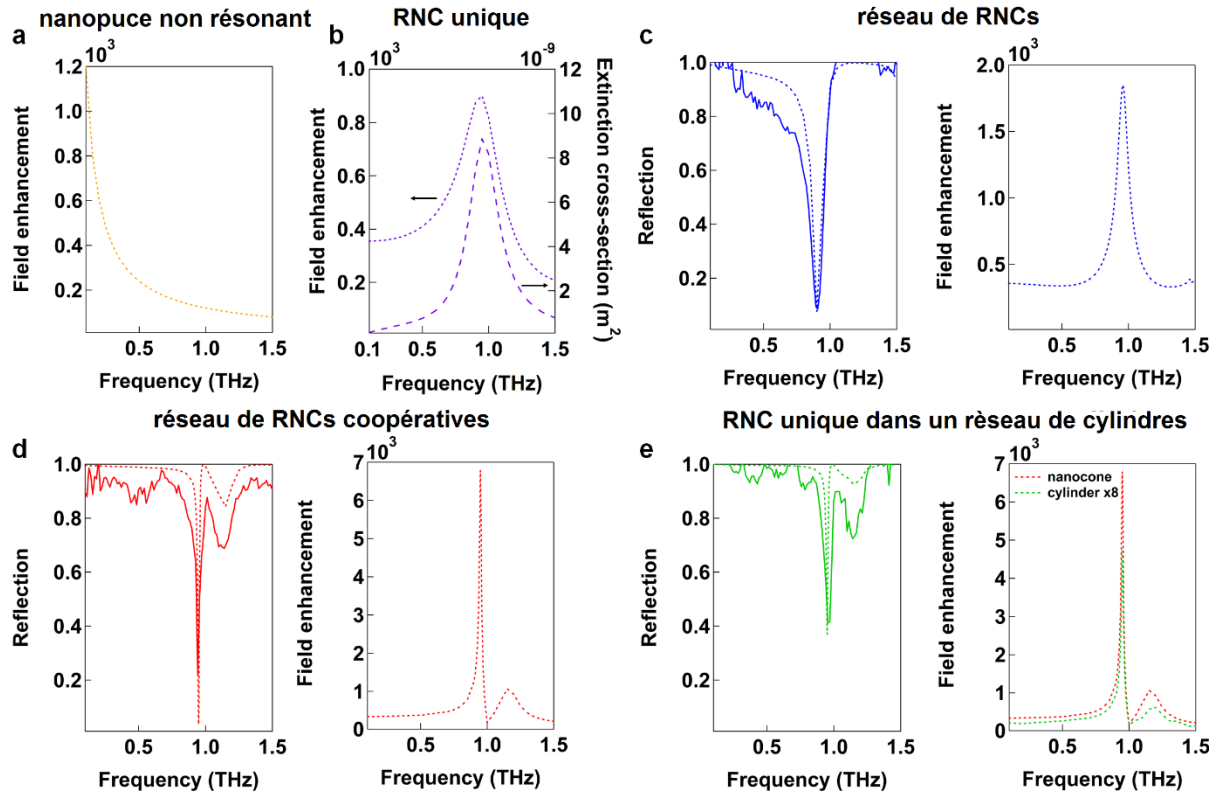


Figure 8.9 Les réponses en fréquence THz des RNCs étudiés

Propriétés des échantillons en champ proche et en champ lointain, calculées numériquement via COMSOL Multiphysics (ou extraites analytiquement dans le cas de l'amélioration du champ de la pointe non résonante) (lignes pointillées), ainsi que la réflectance mesurée des réseaux (lignes pleines). (a) Nanopuce non résonant, (b) RNC unique, (c) Réseau de RNCs, (d) Réseau de RNCs coopératifs et (e) RNC unique dans un réseau de cylindres. Dans ce dernier cas, nous avons simulé un réseau de cylindres dont le rayon de courbure des bords est équivalent à celui du sommet des RNCs. Comme on peut le voir, le renforcement du champ au sommet des cylindres est environ 10 fois inférieur à celui du RNC central (considéré comme équivalent à celui récupéré pour le réseau de RNCs coopératifs).

Tout d'abord, le cas d'un RNC résonant unique sur une surface d'or conductrice infinie a été pris en considération. La valeur maximale calculée de F est d'environ 900 en correspondance de la fréquence de résonance, lorsque la hauteur du RNC est fixée à $\lambda_{\text{res}}/4 \approx 80 \mu\text{m}$ (Figure 8.9b). La section d'extinction calculée numériquement du RNC unique présente également une résonance monopolaire centrée autour de 1 THz, avec une largeur de bande (pleine largeur à mi-hauteur - FWHM) de 250 GHz. Notez que la réponse THz de l'unique RNC n'a pas pu être mesurée directement par spectroscopie THz en champ lointain en raison de la très faible section d'extinction associée à une nanostructure individuelle. La réponse d'un réseau périodique de RNCs résonants à THz a alors

été étudiée. Cette conception permet une émission cohérente d'électrons provenant de plusieurs RNCs, renvoyant un motif d'électrons structuré dans l'espace qui conduit également à un courant global plus élevé par rapport à un émetteur unique. Les RNCs fabriquées, séparées de 140 µm, ont dans ce cas une hauteur de 120 µm, pour compenser le décalage de la position de résonance induit par le réseau, ce qui donne un facteur d'amélioration du champ d'environ 1850 à environ 1 THz. La réflectance du réseau en THz est indiquée sur la Figure 8.9c (ligne pleine) et montre un très bon accord avec les simulations numériques (ligne pointillée), tant en termes de fréquence centrale de résonance que de largeur de bande (environ 115 GHz FWHM dans le cas du réseau). La réponse électromagnétique collective d'un ensemble de nanostructures résonantes peut être optimisée davantage grâce à une récolte appropriée du rayonnement rediffusé par les différents éléments. C'est ce qui a été fait pour le réseau de RNCs coopératives. L'effet de coopération dans ce réseau se traduit par une augmentation significative de l'amélioration du champ local, avec une valeur de crête d'environ 6800 et une largeur de bande de résonance plus étroite (~60 GHz FWHM de la mesure de réflectance, voir Figure 8.9d) par rapport au réseau non coopératif de RNCs. Comme mentionné, l'avantage offert par cet effet de coopération peut également être maintenu dans le cas d'un RNC unique entouré de cylindres résonants. Dans cet échantillon, la hauteur du RNC central et la périodicité du réseau sont les mêmes que celles du réseau de RNCs coopératifs, tandis que la hauteur des cylindres est réduite à 66 µm, pour faire correspondre leur résonance monopolaire à celle du RNC. La Figure 8.9e montre que la mesure de la réflectance THz sur cet échantillon présente des caractéristiques similaires à celle du réseau de RNCs coopératifs. La valeur de l'amélioration du champ électrique à proximité du sommet du RNC est dans ce cas supposée être la même que celle extraite pour le cas du réseau de RNCs coopératifs, comme le suggèrent les simulations numériques réalisées sur un modèle simplifié d'un seul RNC entouré de 8 cylindres. Comme le montre la Figure 8.9e, le renforcement maximal du champ au sommet du RNC est 11 fois supérieur à celui atteint sur les cylindres. En conséquence, comme la photoémission par le champ est très non linéaire par rapport au champ électrique local de THz, cette géométrie hybride ne garantit un "point chaud" d'émission d'électrons individuels.

Pour avoir accès à une évaluation optique simple des caractéristiques d'émission d'électrons induite par le champ électromagnétique des échantillons fabriqués, nous avons caractérisé le signal de fluorescence émis par les atomes de gaz argon entourant les nanostructures métalliques sous une pression statique contrôlée, selon une procédure introduite pour la première fois par (Iwasczuk et al., 2014). En bref, les atomes de gaz sont excités par l'impact avec les électrons extraits, ce qui donne un signal de fluorescence qui peut être directement décrit par l'équation *Fowler-Nordheim* (FN),

renvoyant ainsi les caractéristiques clés de la photoémission. Un schéma du dispositif expérimental utilisé pour cette mesure est présenté à la Figure 8.10a.

Des impulsions THz à large bande (0.1 - 3,0 THz) avec un champ électrique de pointe maximum de 180 kV/cm ont été générées par RO dans le cristal organique non linéaire HMQ-TMS pompé par notre laser Yb amplifié (Rovere et al., 2018). L'échantillon étudié a été placé dans une chambre étanche remplie d'argon gazeux. En cette expérience, deux polariseurs à grille métallique ont été utilisés en série sur le trajet du faisceau pour faire varier l'amplitude du champ incident THz tout en maintenant une polarisation p à leur sortie. Le champ THz a été envoyé à travers une fenêtre de quartz sur l'échantillon avec un angle d'incidence de 30 degrés par rapport à l'axe principal des RNCs. Le champ électrique incident effectif sur l'échantillon E_{exc} peut donc être récupéré en considérant la transmission de la fenêtre de la chambre et la projection du champ électrique sur l'axe principal des RNCs (à noter que $\max_t(E_{\text{exc}}) = 80 \text{ kV/cm}$ pour le champ électrique de crête d'entrée maximum dans notre expérience).

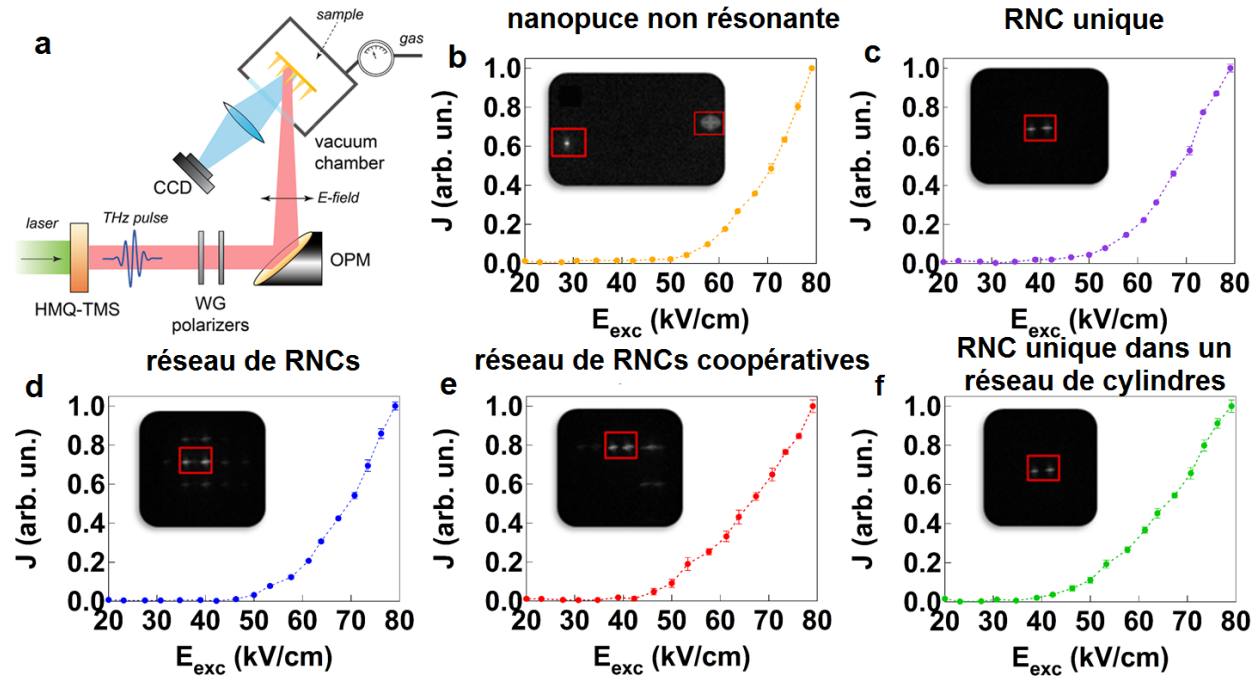


Figure 8.10 Mesures de fluorescence

(a) Schéma de l'installation utilisée pour les mesures de fluorescence. WG - polariseurs à grille métallique; OPM - miroir parabolique à 90 degrés hors axe. (b-f) Données expérimentales de la fluorescence de l'argon mesurée à partir des différentes nanostructures fabriquées en fonction de l' E_{exc} . Des exemples d'images de fluorescence acquises avec la caméra CCD sont présentés dans l'encadré correspondant. L'origine du double point observé pour toutes les structures est la réflexion de la fluorescence émise sur le plan du fond recouvert d'or.

L'intensité de la lumière de fluorescence a été recueillie par un télescope (avec un grossissement d'environ 2, permettant d'imager les apex des nanostructures) et acquise avec une caméra CCD,

permettant une évaluation relative de la fluorescence locale pour chaque nanostructure individuelle dans un échantillon (encadré de la figure 8.10b-f). Chaque image est normalisée par rapport au fond (c'est-à-dire une image prise sans fluorescence), puis l'intensité de la fluorescence est intégrée dans une zone sélectionnée pour l'émetteur considéré. Ainsi, les valeurs d'intensité intégrées ont été tracées en fonction du champ THz incident, obtenant les tendances rapportées dans la figure 8.10b-f, qui peuvent être bien décrites par l'équation FN (Fowler & Nordheim, 1929).

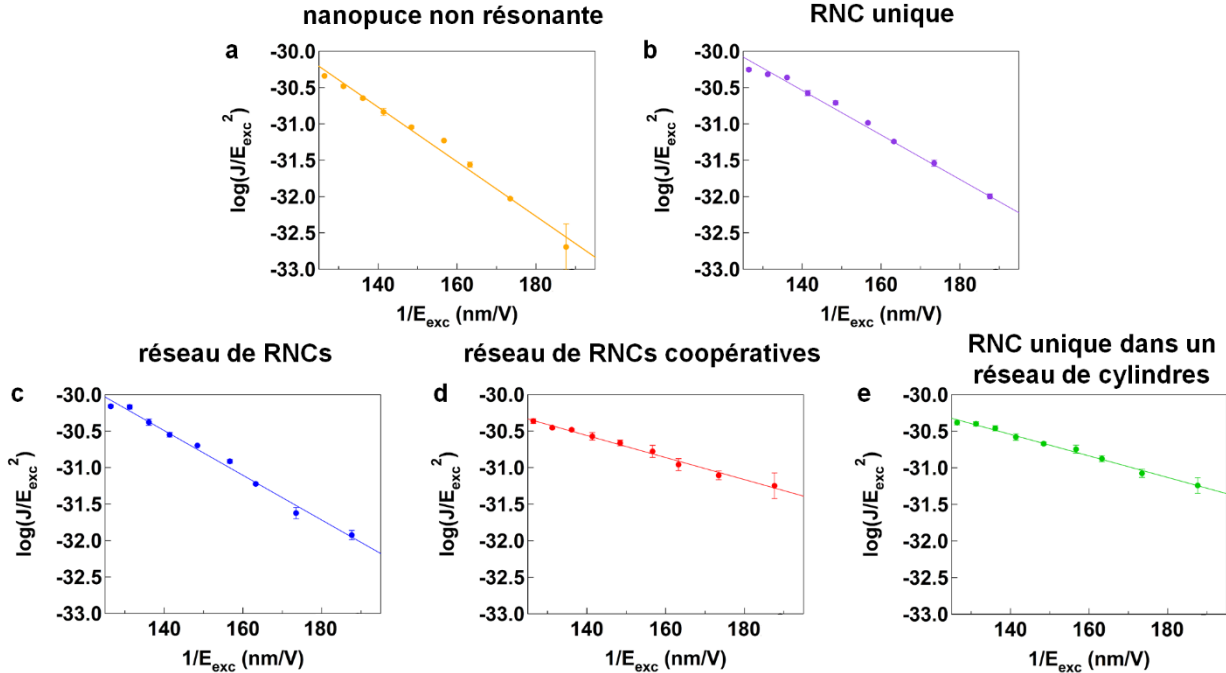


Figure 8.11 Graphiques FN des mesures de fluorescence

a-e) Données expérimentales (points) de la fluorescence de l'argon mesurée et ajustement linéaire à l'aide de l'équation 8.3 (lignes pleines) pour les différents échantillons. À partir de la pente de l'ajustement, il est possible de récupérer une estimation expérimentale de l'amélioration du champ dans le domaine temporel pour chaque échantillon.

Il est important de noter que la forte résonance des RNCs métalliques agit comme un filtre passe-bande de fréquence pour le rayonnement lumineux à large bande THz. Par conséquent, le processus de photoémission observé résulte d'un compromis entre la valeur de crête absolue de l'amélioration du champ à la fréquence de résonance et la partie du spectre d'excitation THz qui remplit effectivement la largeur de bande de résonance des RNCs. Un paramètre de référence peut être défini, c'est-à-dire le pic d'augmentation du champ électrique THz dans le domaine temporel:

$$\beta_{\text{calc}} = \max_t(E_{\text{local}}) / \max_t(E_{\text{exc}}) \quad (8.2)$$

où E_{local} est le champ électrique local dans le domaine temporel évalué à 1 nm au-dessus de l'apex de la nanostructure. Ainsi, β_{calc} prend implicitement en compte le chevauchement spectral entre les impulsions THz incidentes et la résonance des échantillons étudiés. Il convient de noter qu'il est possible de récupérer les valeurs expérimentales de cette amélioration du champ électrique de crête THz dans le domaine temporel pour nos échantillons à partir des mesures de fluorescence. L'équation FN peut être réécrite de façon pratique comme suit:

$$\log \left(J/E_{\text{exc}}^2 \right) = C_1 + C_2/E_{\text{exc}} \quad (8.3)$$

où $C_1 = \log \left(\frac{\phi}{a\beta^2} \right)$ et $C_2 = -\frac{b\phi^{3/2}}{\beta}$. De cette façon, il est possible de représenter les données expérimentales dans un tracé linéaire. Toutes nos mesures de fluorescence présentent un degré élevé de linéarité, comme le montre la Figure 8.11, ce qui confirme la nature du processus de photoémission, qui est déterminé par le champ THz. Grâce à cette représentation, nous pouvons extraire, au moyen d'un simple ajustement linéaire, le facteur de pente C_2 pour chaque échantillon, qui est directement lié au facteur d'amélioration du champ dans le domaine temporel, β_{exp} :

$$\beta_{\text{exp}} = -\frac{b\phi^{3/2}}{C_2} \quad (8.4)$$

Les valeurs de β_{exp} obtenues en ajustant les données des expériences de fluorescence à l'équation (8.4) représentent un moyen efficace de comparer les performances de photoémission des différentes nanostructures. Dans cette comparaison, nous avons considéré une fonction de travail efficace de $\phi = 0.78 \pm 0.03$ eV pour toutes les nanostructures d'or. Cette valeur a été obtenue en ajustant les données expérimentales pour la nanotechnologie non résonante tout en fixant $\beta = 128$ puisque, comme expliqué ci-dessus, il existe une formule analytique bien établie pour ce cas (Podenok et al., 2006). Comme déjà observé par (Iwaszczuk et al., 2014) pour les antennes en or évaporé, la valeur obtenue est inférieure à la fonction de travail généralement rapportée pour l'or en vrac (~ 5 eV) (Lide, 2008). Cette différence a été attribuée à i) des impuretés et des adsorbats de l'air déposés localement sur la zone de photoémission, qui peuvent abaisser ϕ d'un métal sous l'effet d'un effet tunnel des électrons (Duke & Alferieff, 1967); ii) la rugosité intrinsèque de la surface de l'or évaporé, avec des caractéristiques à l'échelle nanométrique au sommet, qui peut conduire à une augmentation du champ local. En effet, une sous-estimation de β entraînerait une diminution de la valeur récupérée pour ϕ , en raison de la dépendance du facteur de pente dans l'équation (8.4) à l'égard de ces deux paramètres. Le tableau 8.1 résume les valeurs d'amélioration du champ dans le

domaine temporel β_{exp} que nous avons obtenues à partir des expériences de luminescence. Elles sont en bon accord avec les facteurs de renforcement correspondants β_{calc} renvoyés par les simulations numériques (équation (8.2), également indiquée dans le tableau 8.1).

Table 8.1 Résultats de l'analyse de la mesure de la fluorescence

Paramètre	Nanopuce non-résonant	RNC unique	Réseau de RNCs	Réseau de RNCs coopératives	RNC dans le réseau de cylindres
$C_2 (\times 10^7)$	(-3.7 ± 0.2)	(-3.1 ± 0.1)	(-3.1 ± 0.1)	(-1.51 ± 0.06)	(-1.47 ± 0.05)
β_{exp}	128 (analytique)	153 ± 10	153 ± 10	314 ± 21	322 ± 21
β_{calc}	128 (analytique)	204	209	344	344

Facteurs de pente C_2 pour chaque échantillon, extraits de l'ajustement des expériences de fluorescence présentées à la Figure 8.11 à l'aide de l'équation 8.4. Les valeurs d'amélioration du champ correspondant sont extraites des mesures (β_{exp}) et des calculs (β_{calc}). Le cas de la pointe non résonante a été utilisé comme référence pour estimer la fonction de travail de l'or ($\phi = 0,78 \pm 0,03$ eV), en fixant β à la valeur extraite analytiquement.

Comme on peut le voir, les valeurs de β liées aux RNCs sont plus élevées que celle de la nanopuce non résonnant, ce qui indique une photoémission d'électrons plus efficace. En outre, l'effet de coopération dans une géométrie de réseau conduit à une augmentation finale d'environ 2.5 fois du facteur d'amélioration du champ dans le domaine temporel par rapport au cas non résonnant ($\beta_{\text{exp}} > 300$ pour le cas de coopération, ce qui signifie que le champ local au sommet du RNC atteint des valeurs supérieures à 24 MV/cm dans nos conditions expérimentales).

Enfin, une augmentation similaire de la photoémission est confirmée pour le cas du réseau de RNCs coopératifs et le RNC unique dans le réseau de cylindres coopératifs. Des mesures électriques de preuve de principe ont également été effectuées, afin de fournir une preuve directe de l'émission d'électrons. Pour cela, un électromètre à semi-conducteurs (Keithley 610C) a été utilisé. L'échantillon étudié a été placé dans une chambre sous ultravide ($\sim 10^{-6}$ mbar) et une feuille de cuivre (anode, de 2x2 cm²) reliée à l'électromètre a été utilisée pour collecter les électrons émis (voir le croquis de la Figure 8.12a). Les photocourants mesurés produits par le réseau de RNCs et le réseau de RNCs coopératives (Figure 8.12b) en fonction de E_{exc} montrent un comportement caractéristique de seuil similaire à celui observé dans les expériences de fluorescence, confirmant ainsi le processus piloté par le terrain. Le courant commence à être observable pour $E_{\text{exc}} \sim 50$ kV/cm et atteint un maximum à 80 kV/cm d'environ 1.5 pA pour le réseau de RNCs et 1.15 pA pour le réseau coopératif, ce qui

correspond à 6 fC et 4.6 fC par impulsion (3.75×10^4 and 2.87×10^4 électrons par impulsion), respectivement.

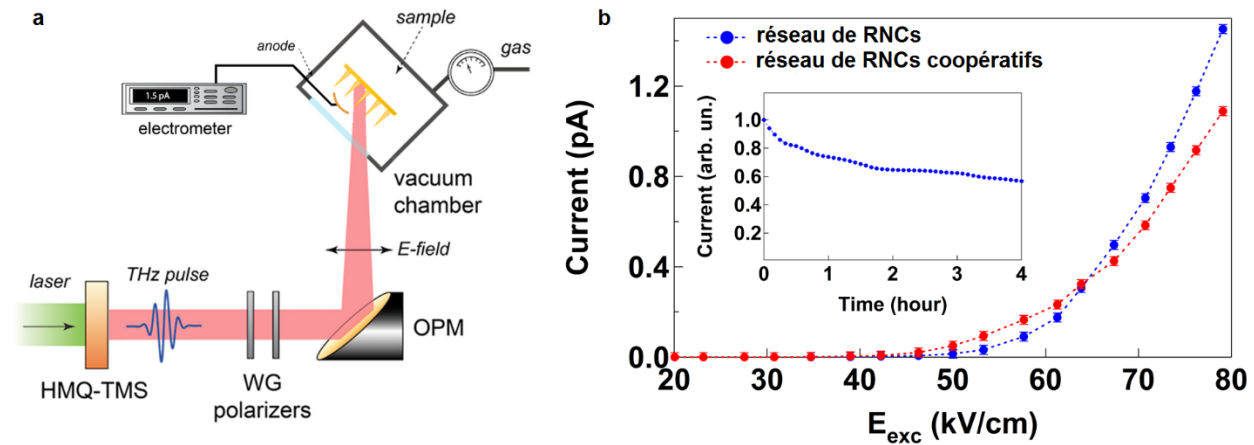


Figure 8.12 Mesures des photocourants

(a) Schéma du dispositif expérimental utilisé pour mesurer le photocourant. (b) Courant en fonction du champ électrique de crête incident de THz pour les deux échantillons du réseau RNCs. Encadré : tendance du courant pour le réseau de RNCs lors d'une exposition de 4 heures au champ de THz le plus élevé.

Il est important de souligner que les faisceaux d'électrons extraits dans notre installation connaissent une propagation transversale considérable, due aux effets de la charge spatiale, lors de la propagation de la photocathode à l'anode. Un modèle numérique simple a été développé pour étudier la propagation des électrons extraits entre l'apex du RNC et la feuille de cuivre collectrice, placée à $d = 1.5$ cm de l'émetteur (afin de ne pas bloquer le rayonnement THz). Dans ce modèle, les électrons N_e à énergie cinétique ϵ , sont générés de manière aléatoire dans une zone initiale de 150×150 nm², et les trajectoires des électrons sont évaluées numériquement en résolvant l'équation 3D du mouvement, en tenant compte de l'interaction de Coulomb entre tous les électrons. Afin de récupérer le nombre d'électrons extraits, N_e pour le réseau de RNCs et le réseau de RNCs coopératives, nous avons intégré le courant d'émission dans le temps calculé au moyen de l'équation FN, obtenant ainsi le nombre d'électrons extraits par impulsion dans les deux cas. En particulier, dans le cas du réseau de RNCs, le nombre d'électrons estimé ($N_e = 3.45 \times 10^4$) est très proche du nombre mesuré ($N_e = 3.75 \times 10^4$). Dans le cas du réseau coopératif, le nombre d'électrons extraits est estimé > 6 fois plus élevé ($N_e = 2.22 \times 10^5$). Comme le montre ce modèle, les faisceaux d'électrons émis par le réseau de RNCs coopératifs présentent un étalement spatial considérable (jusqu'à 5-6 cm de diamètre) après une propagation de 1.5 cm, ce qui est plus important que dans le cas du réseau de RNCs (jusqu'à 3 cm de diamètre), en raison du nombre plus élevé d'électrons extraits. Ainsi, les contraintes géométriques de ce schéma de détection de base entravent la collecte complète du courant photoélectrique total. Cela a probablement affecté la mesure du réseau de RNCs coopératif encore

plus sévèrement que celle du réseau non coopératif, étant donné que les RNCs du premier échantillon sont dotées d'une valeur β plus élevée et sont ensuite censées fournir un nombre plus élevé d'électrons par impulsion de THz, ce qui entraîne une plus grande dispersion des électrons émis, comme l'estiment nos calculs. En outre, les deux réseaux de RNCs ont également un nombre différent de RNCs par unité de surface (~ 2 fois plus petit dans le cas du réseau de RNCs coopératif), ce qui affecte clairement le courant global mesuré dans les deux cas. Ces faits empêchent l'utilisation d'une telle caractérisation électrique pour une comparaison quantitative entre les réseaux. De plus, le courant photoélectrique mesuré à l'aide de ce dispositif développé en interne s'est avéré trop faible pour renvoyer des ensembles de données cohérents pour les échantillons avec un seul émetteur.

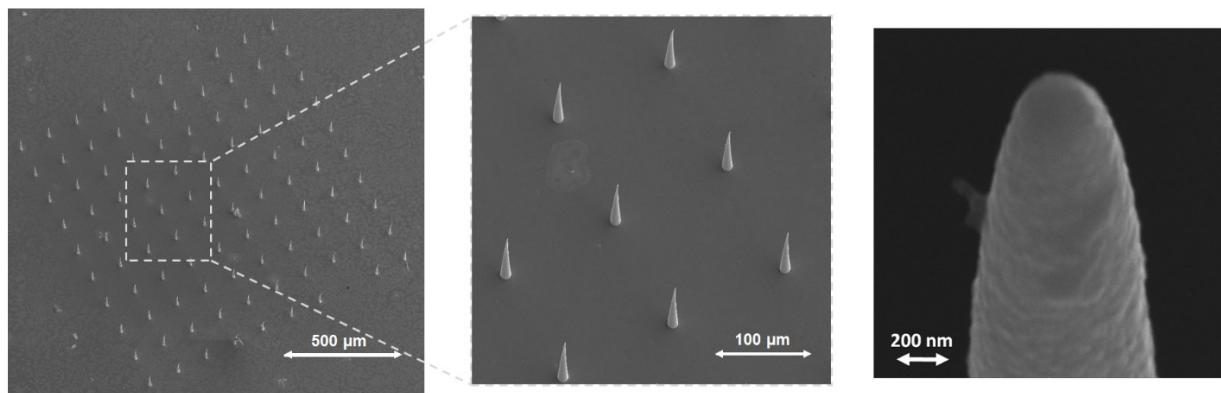


Figure 8.13 Images MEB du réseau de RNCs prises après les expériences de caractérisation

Les RNCs présentent une bonne stabilité structurelle même après une exposition à ~ 50 millions d'impulsions THz. Pour tester la robustesse de nos nanostructures en tant qu'émetteurs d'électrons, le photocourant émis par le réseau de RNCs a également été acquis pour de longues durées d'exposition et sous le champ THz incident le plus élevé fourni par notre source. Comme on peut le voir dans l'encadré de la Figure 8.12, les RNCs en or sont toujours fonctionnels après plusieurs heures d'illumination continue en THz. La présence d'une lente décroissance dans le temps du photocourant, outre un certain degré de dégradation de la surface de l'émetteur, est également liée à une accumulation de charge résiduelle sur l'anode qui a été observée dans notre setup. La stabilité structurelle des RNCs a été confirmée par une inspection au MEB des nanostructures après une exposition prolongée à la fréquence THz (environ 50 millions d'impulsions THz). Comme le montre la Figure 8.13, la surface en or des RNCs ne présente pas de signes de dommages critiques, en particulier à proximité de l'apex des RNCs, qui est généralement la zone la plus sollicitée dans ces expériences (Li & Jones, 2016).

Enfin, la distribution de l'énergie des électrons $f(\varepsilon)$ a été obtenue au moyen d'un modèle en deux étapes. La Figure 8.14 montre la répartition de l'énergie des électrons photoémis pour les différents échantillons testés dans les conditions de nos expériences. Selon ce modèle, l'effet de coopération

devrait entraîner une multiplication par deux de la coupure d'énergie des électrons par rapport au cas d'une pointe non résonnante, avec des valeurs énergétiques significatives dépassant 400 eV pour seulement 80 kV/cm de champ électrique incident effectif, E_{exc} .

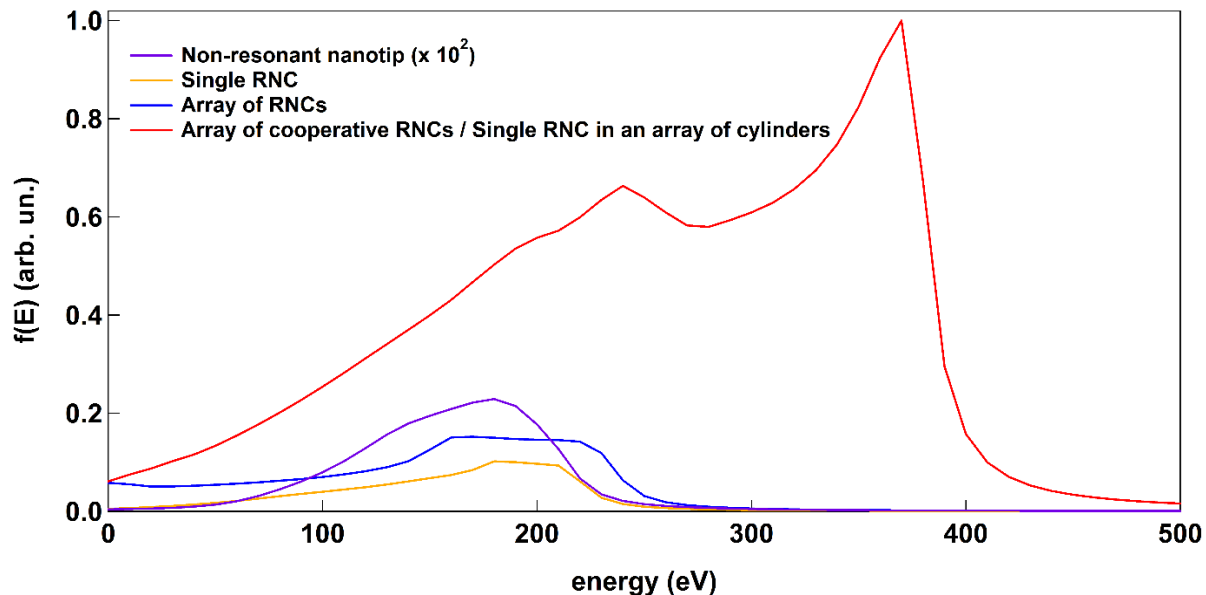


Figure 8.14 Répartition de l'énergie des électrons photoémis par les différentes nanostructures

Conclusions et perspectives d'avenir

Les lasers Yb représentent déjà la nouvelle frontière de la technologie laser ultrarapide, mais leur exploitation pour la génération efficace d'impulsions THz intenses n'a pas encore été pleinement explorée, en raison du fait que les plus communs cristaux hautement non linéaires pour RO n'offrent pas de bonnes conditions de concordance de phase à 1030 nm. Comme solution possible à ce problème, dans ce travail de thèse, deux stratégies différentes pour générer des radiations THz à haut champ au moyen d'un laser Yb amplifié ont été étudiées.

Premièrement, il a été démontré que le cristal organique récemment synthétisé HMQ-TMS peut être utilisé efficacement pour la génération simple et colinéaire d'impulsions THz de champ électrique de haute crête en utilisant un laser Yb amplifié disponible dans le commerce comme pompe optique. Des champs électriques de crête THz supérieurs à 200 kV/cm ont été obtenus avec une émission spectrale s'étendant au-delà de 3 THz, et une énergie THz par impulsion de 1.1 μ J, ce qui correspond à un rendement de conversion énergétique précieux de 0.26%. De plus, cette source de THz a été utilisée dans une expérience de démonstration de principe de Z-scan non linéaire, induisant une

saturation significative de l'absorption de THz dans une couche mince d'InGaAs dopé n, montrant ainsi le potentiel de cette nouvelle source pour l'exploration des effets non linéaires de THz dans la matière condensée.

En outre, un système THz-SDT basé sur un laser Yb offrant une bande passante extrêmement large (jusqu'à 60 THz) avec des champs électriques de pointe supérieurs à 50 kV/cm a été introduit comme preuve de principe, en utilisant un étage de compression d'impulsions HCF et un schéma de génération de plasma bicolore. La génération d'ultra large bande a été réalisée grâce à la compression d'impulsions basée sur le HCF, qui nous a permis de convertir des impulsions de 170 fs de long émises par notre amplificateur laser Yb en des impulsions de 18 fs de long. Cette méthode ouvre la voie à l'exploitation des nombreux avantages de la technologie laser Yb (notamment la disponibilité de très hautes puissances moyennes/taux de répétition élevés) pour la génération THz à très large bande. À cet égard, pour l'adoption de systèmes Yb à taux de répétition élevé (MHz) comme stations de pompage, des tensions de commutation haute fréquence au niveau kV seraient nécessaires pour effectuer la détection DCBA, ce qui est extrêmement difficile à mettre en œuvre. Une alternative prometteuse qui peut être explorée dans des travaux futurs est représentée par une technique de détection THz récemment développée, appelée *détection cohérente à l'état solide biaisé* (DCESB) (Tomasino et al., 2017). En effet, la DCESB peut être polarisée avec seulement 10 V et peut donc facilement fonctionner à des fréquences de commutation de MHz, ce qui montre un grand potentiel à être combiné avec la méthode de génération proposée dans ces travaux pour le développement de la prochaine génération de systèmes THz-SDT à ultra large bande, à haut champ et à haut débit de répétition THz. La source THz à ultra large bande développée peut également être utilisée pour l'exploration des effets non linéaires dans notre système de couplage fort de phonon. En effet, l'hybridation de résonance phononique étudié par (Jin et al., 2018) a lieu à environ 8 THz, de sorte que la source développée peut être utilisée pour pomper intensément le système, en entrant dans le régime de couplage non linéaire fort (Bishop et al., 2008) où l'hybridation de résonance phononique serait modifiée en fonction de l'intensité du pompage, un territoire inexploré pour la modification de la réponse phononique dans les nanosystèmes.

Enfin, les impulsions THz intenses générées par la source HMQ-TMS ont été utilisées pour explorer un phénomène de champ fort aux fréquences THz, en combinaison avec l'amélioration locale du champ fournie par les nanostructures résonantes THz. En particulier, une nouvelle stratégie de conception de photocathodes pour la photoémission ultra-rapide à champ THz a été proposée, exploitant les avantages de l'impression 3D à haute résolution. Cette approche permet d'obtenir une émission et une accélération d'électrons hors du plan en utilisant des sources THz de table à large

bande avec des champs électriques de pointe au niveau de 100 kV/cm. En utilisant la modélisation numérique, la caractérisation du champ lointain à THz et l'analyse de la fluorescence gazeuse de l'argon induite par les électrons, nous avons montré l'avantage offert par les RNCs présentant une résonance monopolaire à des fréquences de THz par rapport aux pointes non résonantes traditionnelles. En outre, nous avons introduit un degré d'optimisation supplémentaire en adaptant la réponse collective des RNCs lorsqu'elles sont disposées en réseau. Une augmentation significative du champ électrique de crête THz nano-localisé d'un facteur de 2.5 par rapport au cas non résonnant standard a été démontrée pour les nanostructures coopératives. Cela signifie que le champ électrique de crête THz peut être réduit de manière équivalente du même facteur pour obtenir la même extraction/accélération d'électrons. Fait remarquable, une telle accélération peut également être obtenue pour l'émission d'électrons d'une nanostructure individuelle, comme nous l'avons montré pour le cas d'une RNC dans un ensemble de cylindres résonnantes. Nous avons également mis au point une installation sur mesure pour effectuer des mesures de photocourant de démonstration de principe qui ont corroboré la caractérisation de l'intensité de la fluorescence, confirmant la nature de l'émission d'électrons en fonction du champ. Un courant maximum de 1.5 pA a été enregistré, correspondant à 3.75×10^4 électrons par impulsion THz, ce qui montre que les photocathodes mises au point peuvent fournir des grappes d'électrons de haute luminosité intéressantes pour, par exemple, des expériences de diffraction électronique à résolution temporelle. Les nanostructures fabriquées présentaient une bonne résistance structurelle après plusieurs heures d'exposition à des champs THz intenses. Si notre stratégie a été démontrée dans le cas des sources THz à large bande, l'utilisation d'une source à bande étroite permettrait d'exploiter pleinement la résonance RNC aiguë. En fait, les sources THz à bande étroite au niveau du champ électrique de crête de kV/cm peuvent être construites avec des lasers femtoseconde de quelques μJ d'énergie (Krause et al., 2011). Une telle configuration pourrait permettre de créer une nouvelle classe de sources d'électrons ultrarapides à THz avec des taux de répétition sans précédent (au niveau MHz). Nous envisageons donc que la combinaison des progrès de la technologie des sources THz avec des nanostructures résonantes imprimées en 3D de conception rationnelle puisse trouver des applications dans le développement de la prochaine génération de sources d'électrons ultrarapides nano-localisées et cohérentes.